Observation of Semileptonic Decays of Baryons Containing Bottom Quarks at the Fermilab Tevatron

Jeffrey Chun-Lee Tseng

A dissertation submitted to the Johns Hopkins University
in conformity with the requirements for
the degree of Doctor of Philosophy.

Baltimore, Maryland
1996

Abstract

The semileptonic decay of the Λ_b baryon is observed at CDF in $19.3 pb^{-1}$ of data from Run 1A through its decay $\Lambda_b \to \Lambda_c^+ e^- \overline{\nu}_e X$, by the identification of a high-energy electron and the full reconstruction of $\Lambda_c^+ \to pK^-\pi^+$ with the correct charge relationship and combined invariant mass. From 35.7 ± 9.4 signal events, the cross section times branching fraction is measured to be

$$\begin{aligned} &\sigma_b(p_T^b > 10.5 \text{ GeV}/c, |y| < 1)\times \\ &f(b \to \Lambda_b)\text{Br}(\Lambda_b \to \Lambda_c^+ e^- \overline{\nu}_e X)\text{Br}(\Lambda_c^+ \to pK^-\pi^+) \\ &= (2.8 \pm 0.72(stat) \pm 0.41(syst)^{+1.05}_{-0.86}(theory)) \text{ nb}. \end{aligned}$$

Using the previously measured CDF b quark cross section at 10.5 GeV/c, $1.99 \pm 0.30 \pm 0.41 \mu b$ and removing common systematic uncertainties,

$$\begin{aligned} &f(b \to \Lambda_b)\text{Br}(\Lambda_b \to \Lambda_c^+ e^- \overline{\nu}_e X)\text{Br}(\Lambda_c^+ \to pK^-\pi^+) \\ &= (13.9 \pm 3.6(stat) \pm 4.4(syst)^{+5.3}_{-4.3}(theory)) \times 10^{-4}. \end{aligned}$$

This is the first Λ_b semileptonic rate measurement at a hadron collider. This research was conducted under the guidance of Professor Bruce Barnett.

Acknowledgements

An African proverb states that it takes a whole village to raise a single child. That this proverb is true is evident in the both the child himself and in whatever research he may choose to pursue or dissertation he may choose to write. High on my list, of course, are my parents, Chingling and Feiying Tseng, and my brother, Dr. Daniel Tseng, whose support, guidance, and wisdom have certainly shaped my life in many positive ways.

The village which raised this dissertation must of course include the lively academic environments of the Johns Hopkins University and the Fermi National Accelerator Laboratory. My adviser, Professor Bruce Barnett, who turned my attention to bottom baryon physics in the first place, has overseen and supported my research and education, helping me through not a few difficult and vexing problems along the way. I have also received much help and support from the two Johns Hopkins research associates, Dr. John Skarha and Dr. Rick Snider. One notable feat of these "village elders," Dr. Skarha in particular, was to teach me how to give presentations. It was no mean accomplishment. I am also grateful to have worked with such colleagues as Steve Vejcik, Chris Boswell, Alan Spies, Doug Glenzinski, and Jeff Cammerata, my fellow Johns Hopkins graduate cohorts while at Fermilab. Among those of the Fermilab village, I must single out Dr. Ting Miao of Fermilab, whose work on the Λ_b lifetime, as well as his advice and encouragement, certainly pushed my research along; and Dr. Fritz DeJongh of Fermilab and Professor Paris Sphicas of the Massachusetts Institute of Technology, who helped guide this research to its conclusion.

The One who made all the above acknowledgements possible, of course, deserves

the highest thanks and, indeed, worship. Not only has He taught me about love, joy, justice, and mercy, as well as the good news of salvation through His Son Jesus Christ, but He also created a world which, after thousands of years of intentional human study, remains a fascinating and humbling mystery.

Contents

List of Tables

List of Figures

"For my thoughts are not your thoughts,
neither are your ways my ways,"
declares the LORD.
"As the heavens are higher than the earth,
so are my ways higher than your ways
and my thoughts than your thoughts."
(Isaiah 55:8-9)

Chapter 1

Overview

The last half century has seen an astonishing variety of phenomena described, classified, and incorporated into a single theoretical structure known as the "Standard Model." This theory of matter describes the behavior of elementary particles under the influence of electromagnetic, weak, and strong forces, and, by extension, the behavior of the forces themselves. We describe in this chapter this theory and how it is used in experimental particle physics measurements.

1.1 The Standard Model

The most obvious elementary particle in the Standard Model is the electron, pervasive in its chemical and electrical effects. The electron belongs to a family of spin-$\frac{1}{2}$ particles known as the "leptons" which are subject to electromagnetic and weak forces. There are six leptons whose properties are summarized in Table 1.1. [1] They are paired into three generations,

$$\begin{pmatrix} \nu_e \\ e \end{pmatrix}, \begin{pmatrix} \nu_\mu \\ \mu \end{pmatrix}, \begin{pmatrix} \nu_\tau \\ \tau \end{pmatrix},$$

lepton	charge	mass (MeV/c^2)
ν_e	0	< 0.0000051 (95% C.L.)
e	-1	0.511
ν_μ	0	< 0.27 (90% C.L.)
μ	-1	105.66
ν_τ	0	< 31 (95% C.L.)
τ	-1	1777.1

Table 1.1: Lepton properties.

which reflect the observed fact that lepton number is conserved within each generation, that is, the number of electrons and electron neutrinos is the same before and after a reaction. The same holds for μ's and ν_μ's, and τ's and ν_τ's.

The three-generation structure is mirrored in the other family of spin-$\frac{1}{2}$ particles known as the "quarks,"

$$\left(\begin{array}{c} u \\ d \end{array} \right), \left(\begin{array}{c} c \\ s \end{array} \right), \left(\begin{array}{c} t \\ b \end{array} \right),$$

whose properties are summarized in Table 1.2. Unlike the leptons, quarks are subject to the strong force as well as the electromagnetic and weak forces. This difference is important, since the properties of the strong force are such that the quarks are confined in bound states with other quarks—they are never observed in isolation. Like the leptons, only the first generation of particles in this family are familiar in the everyday world.

Unlike lepton family number, however, interactions do not conserve quark family number. This is due to the fact that the mass eigenstates are not the same as the weak eigenstates, resulting in a mixing of quark flavors. By convention, the

quark	charge	mass (MeV/c^2)	I_z	S	C	B	T
d	$-\frac{1}{3}$	5 to 15	$-\frac{1}{2}$	0	0	0	0
u	$+\frac{2}{3}$	2 to 8	$+\frac{1}{2}$	0	0	0	0
s	$-\frac{1}{3}$	100 to 300	0	-1	0	0	0
c	$+\frac{2}{3}$	1000 to 1600	0	0	+1	0	0
b	$-\frac{1}{3}$	4100 to 4500	0	0	0	-1	0
t	$+\frac{2}{3}$	175000 ± 13000	0	0	0	0	+1

Table 1.2: Quark properties. The masses of the u, d, and s quarks are "current-quark" estimates, while the c and b masses are from mesons. The top quark mass is from $\overline{t}t$ events at CDF.

lower quarks, d, s, and b, are taken to mix according to a matrix

$$\begin{pmatrix} d' \\ s' \\ b' \end{pmatrix} = \begin{pmatrix} V_{ud} & V_{us} & V_{ub} \\ V_{cd} & V_{cs} & V_{cb} \\ V_{td} & V_{ts} & V_{tb} \end{pmatrix} \begin{pmatrix} d \\ s \\ b \end{pmatrix}, \tag{1.1}$$

where the q' and q are the weak and mass eigenstates, respectively. This matrix is known as the Cabibbo-Kobayashi-Maskawa ("CKM") matrix, and is unitary if we assume that there are only three quark generations. Unitarity constrains the free parameters in the matrix to three real angles and one complex phase. Measuring these parameters is one of the most important goals of particle physics today: since they are not fixed within the Standard Model itself, they could reflect physics beyond it.

Quarks and leptons interact with one another through gauge bosons, so called because they arise from imposing "local gauge invariance," which means that the equations of motion must be same when the quantum fields are multiplied by a

unitary phase factor $U(x)$, a function of spacetime position. When $U(x) \in U(1)$, having the form $e^{i\alpha(x)}$, where $\alpha(x)$ is a scalar function, the gauge boson corresponds to the photon, which mediates the electromagnetic force. When $U(x) \in SU(2) \times U(1)$, the result is the unified electroweak force with its photon, $W^{\pm}$, and Z^0 gauge bosons. Another massive field, the Higgs boson, is postulated to break the symmetry of the theory and to thus explain the fact that the W and Z have large masses while the photon remains massless.

The description of the strong force, Quantum Chromodynamics (QCD), is also a gauge theory where $U(x) \in SU(3)$. In this theory, quarks have a "color" charge of red, green, or blue, and their interactions are mediated by eight gauge bosons called "gluons." The strong force binds quarks together. Its consequences will be discussed in the next section.

Gravity is also recognized as a fundamental force and is described by a gauge theory, but its relationship with the other three forces remains unclear and is not incorporated in the Standard Model. Since its coupling is so comparatively feeble—roughly 10^{-41} of that of the electromangetic interaction—we ignore it in the analysis of our experimental data.

1.2 Quarks and Hadrons

One of the most intriguing and challenging features of the strong force is that the gluon density between two quarks increases with distance, in stark contrast with the other forces, for which the mediating boson density tends to decrease with distance. The increasing gluon density results in "color confinement": bound states must always be colorless, and quarks in such a bound state sit in an essentially infinite potential well. Indeed, to pull two quarks apart is to increase the energy

force	gauge boson	mass (GeV/c^2)	source
electromagnetism	γ	0	charge
weak	$W^{\pm}$	80.22 ± 0.26	weak
	Z^0	91.187 ± 0.007	hypercharge
strong	g	0	color

Table 1.3: The Standard Model gauge bosons.

density to such an extent that two new quarks are created. Experiments therefore deal with these bound states, or "hadrons." Because of the three color charges, hadrons come in two varieties: mesons, which combine a quark and an antiquark, which has an anticolor charge; and baryons, which combine three quarks or three antiquarks, the three colors combining into a neutral, or "colorless," combination. The behavior of these hadrons must be derived from our quark-level understanding of matter. This derivation is no trivial matter. This section describes the production and decay of the Λ_b baryon in $\overline{p}p$ collisions in the context of the quark model.

1.2.1 Λ_b Production

Briefly, b and $\overline{b}$ quarks are produced in interactions between partons in the initial proton and antiproton, as shown in Figure 1.1, and are combined with other quarks to form hadrons. This latter process is called "fragmentation." The production and fragmentation processes are generally assumed to be independent and may be treated separately.

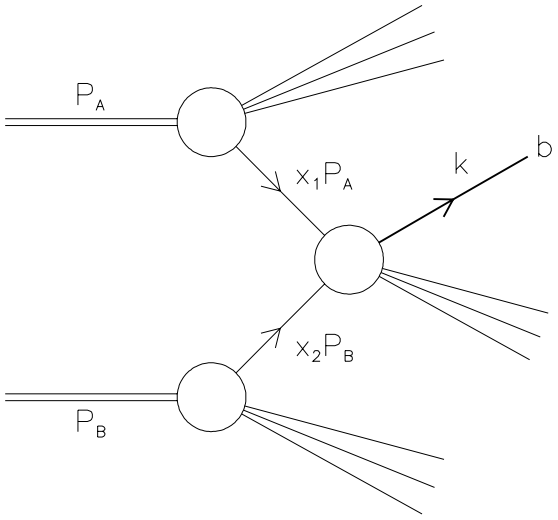

Figure 1.1: Schematic of the process $\overline{p}p \rightarrow bX$.

Since the partons in the proton and antiproton include not only the three valence quarks or antiquarks but also the sea of $\overline{q}q$ pairs and gluons, single b quark production proceeds by all the following processes:

$$\begin{aligned} q + \overline{q} &\rightarrow bX \\ g + q &\rightarrow bX \\ g + \overline{q} &\rightarrow bX \\ g + g &\rightarrow bX \end{aligned}$$

The inclusive single-quark cross section, σ_b, for these processes has been calculated using the lowest order graphs shown in Figure 1.2 as well as higher graphs to order α_s^3, taking advantage of the fact that α_s is small for processes characterized by large momentum transfers. The calculation leaves two free parameters: a renormalization mass scale, μ, which we take to be $\mu_0 = \sqrt{m_b^2 + p_T^2}$; and the b quark

mass, m_b, which we take to be 4.75 GeV/c^2. This m_b is not the same as that shown in Table 1.2, because this quantity depends upon the renormalization scheme. In practice, the p_T distribution of the b quark is not observed because of fragmentation. Moreover, in this analysis the hadron itself is only partially reconstructed. Therefore the cross section is quoted integrated above a certain p_T^{min}, below which the b events do not enter the analysis in appreciable quantities, and in a range of rapidity.

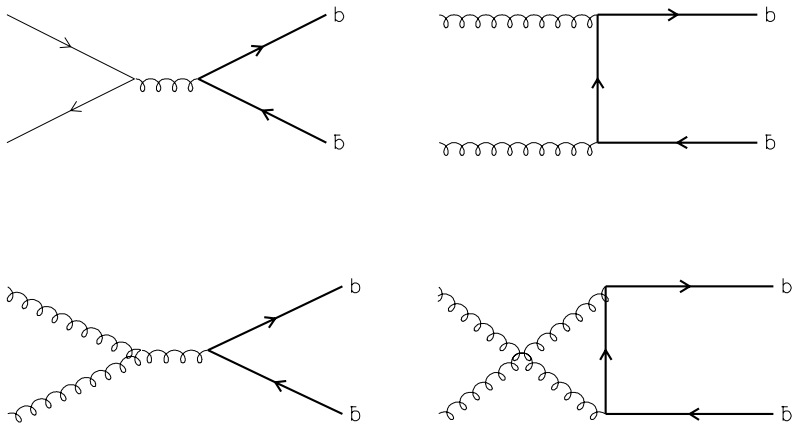

Figure 1.2: Lowest order graphs for the single b quark inclusive cross section calculation.

The cross section prediction also depends upon the proton structure functions which parameterize the composition of quarks and gluons that make up the proton. Several sets of structure functions have been calculated by A.D. Martin, W.J. Stirling, and R.G. Roberts, by analyzing a wide assortment of processes, including deep inelastic scattering as well as Drell-Yan and W production. [5] These structure

functions are often labeled "MRSD_0," with the "MRSD_-" functions as an upper limit.

Fragmentation is another process which is difficult to calculate using full QCD. Qualitatively, a leading quark stretches the gluon field generated by its color charge. The energy density increases as a result until it is large enough to create real quark-antiquark pairs. This process is shown schematically in Figure 1.3. Some of these quarks form color-neutral hadrons and disengage from the gluon field, while other quarks continue pulling on it until all the initial energy is expended. We assume for simplicity that at high enough p_T the fragmentation of the single leading quark is independent of its production.

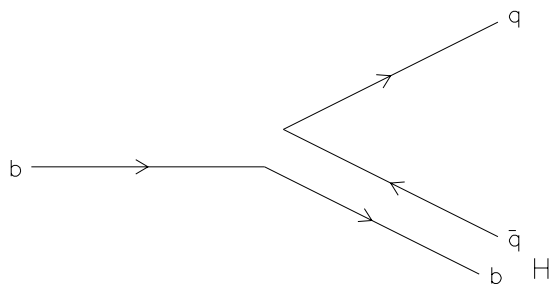

Figure 1.3: Schematic of the fragmentation process, where the b quark pulls a $\overline{q}q$ pair out of the color field, forming the hadron h with the $\overline{q}$.

Fragmentation is described in terms of functions $D_q^h(z)$, which are the probabilities of generating the hadron h in the fragmentation of the quark q with energy-momentum fraction z. A common definition of z is

$$z \equiv \frac{(E + p_{||})_h}{(E + p)_q} \tag{1.2}$$

where $p_{||}$ is the hadron momentum parallel to the initial quark direction. This definition has the advantage of being invariant with respect to boosts along the

quark direction. The relation

$$\sum_h \int_0^1 z D_q^h(z) dz = 1 \tag{1.3}$$

follows from momentum conservation.

Peterson *et al.* have taken advantage of the charm and bottom quarks' large masses to propose a simple parameterization of their fragmentation functions. [6] A fast-moving heavy quark does not lose much of its energy when it is paired with a newly created light quark. Quantum mechanical arguments show that the transition amplitude is inversely proportional to the energy transfer, ΔE,

$$A(Q \to H + q) \propto \Delta E^{-1}, \tag{1.4}$$

$$\Delta E = E_H + E_q - E_Q, \tag{1.5}$$

where E_H, E_q, and E_Q are the energies of the new hadron, the newly created quark, and the initial heavy quark, respectively. The energy transfer may be expanded as follows, with the approximation that the mass of the hadron is close to that of the heavy quark,

$$\Delta E = \sqrt{m_H^2 + z^2 p^2} + \sqrt{m_q^2 + (1-z)^2 p^2} + \sqrt{m_Q^2 + p^2} \tag{1.6}$$

$$\propto 1 - \frac{1}{z} - \frac{\epsilon_Q^h}{1-z} \tag{1.7}$$

where $\epsilon_Q^h = m_q^2/m_Q^2$, the ratio of effective masses of the quarks involved in the hadron, is an input parameter for the model and must be measured in data for individual hadron species. The fragmentation function may then be written

$$D_Q^h = \frac{N}{z[1 - z^{-1} - \epsilon_Q(1-z)^{-1}]^2}, \tag{1.8}$$

where N is the normalization constant, and an additional z^{-1} factor has been introduced for the longitudinal phase space. Measurements at e^+e^- experiments

give the following values: [7]

$$\epsilon_c = 0.06^{+0.02+0.02}_{-0.01-0.01} \tag{1.9}$$

$$\epsilon_b = 0.006^{+0.001+0.002}_{-0.001-0.002}. \tag{1.10}$$

As expected, the ratio of the two ϵ_Q's,

$$\frac{\epsilon_c}{\epsilon_b} = \frac{m_b^2}{m_c^2} = 10^{+4+5}_{-2-4}. \tag{1.11}$$

The above argument pertains most directly to meson production via fragmentation, whereas baryon production requires popping a diquark-antidiquark out of the gluon field. We assume for the present that the bottom quark is heavy enough that the effective mass of the diquark is similar to that of the antiquark in the meson case, and therefore that $\epsilon_b^{\Lambda_b}$ is close to the inclusive ϵ_b measured above.

1.2.2 Semileptonic Decay

The experimental study of the electroweak quark physics would ideally measure quantities related to the vertex illustrated in Figure 1.4, where two quarks of different flavors couple to a W boson. One measurable quantity of special interest is the CKM matrix element which determines the vertex coupling strength. In the case of a $b \to c$ transition, however, there is not enough mass to make a real W, and hence another vertex must terminate the W line, as shown in Figure 1.5. This vertex may couple the W to other quarks or to a lepton-antilepton pair. Taking the diagram to represent b decay, we have in Figure 1.5 diagrams for the transitions $b \to cq\overline{q}$ and $b \to c\ell\overline{\nu}_\ell$.

In addition, since the observed particles are actually hadrons, the quarks must be "dressed" with other quarks. As shown in Figure 1.6, if the second vertex couples the W to two other quarks, the decay proceeds via internal W emission,

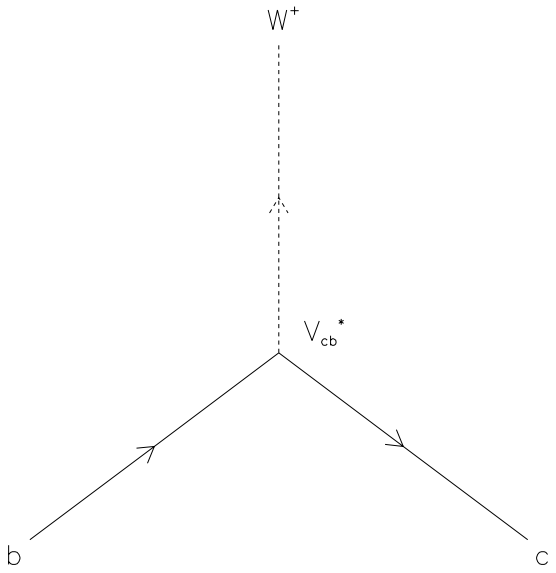

Figure 1.4: The bcW vertex.

Figure 1.5: b quark decay, to a three-quark final state (left), or semileptonic final state (right).

where the W decay quarks join with initial quarks, and external W emission, where the W decay quarks hadronize independently. These are only the simplest diagrams; Figure 1.7 shows graphs with additional gluon lines which must be included in any calculation of experimental observables. Such calculations rapidly become very complicated.

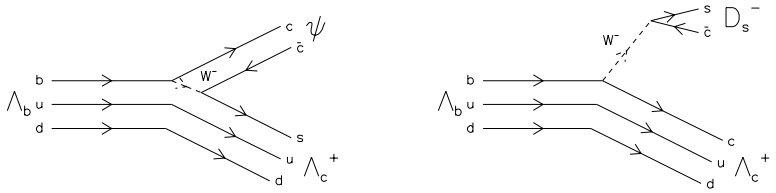

Figure 1.6: Lowest-order hadronic decays proceeding via internal (left) and external (right) W emission.

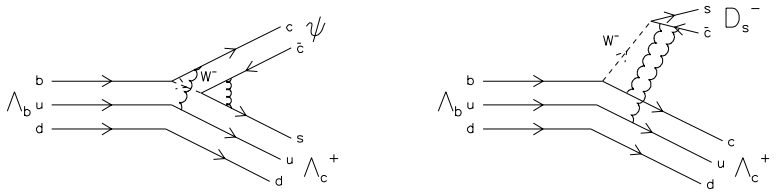

Figure 1.7: A sample of hadronic decay diagrams with additional gluon lines.

If, on the other hand, the virtual W decays to a lepton pair, for instance an electron and an electron antineutrino, as shown in Figure 1.8, the picture simplifies considerably, due to the leptons' insensitivity to the strong force. The gluon interactions are thereby reduced, and external W emission is the only option. Moreover,

electroweak lepton physics is well understood on the elementary particle level. For these reasons, semileptonic decays are important tools in understanding quark-level physics.

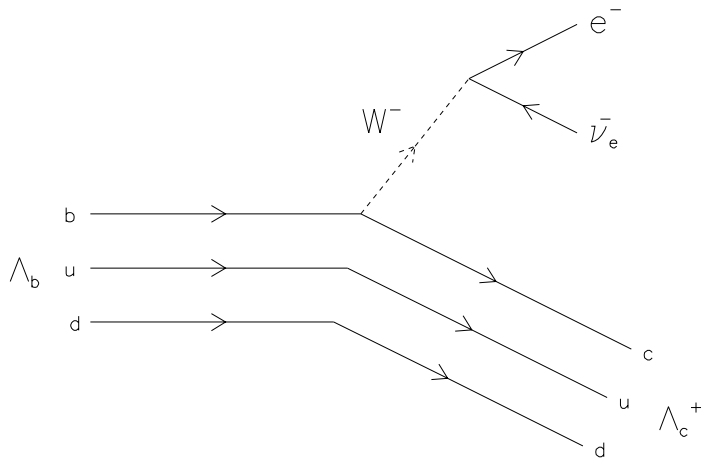

Figure 1.8: Semileptonic Λ_b decay.

Semileptonic decay offers an experimental advantage in that the daughter lepton—in this case, an electron—is readily identifiable. This fact is especially important at a hadron collider, where the b production cross section is much smaller than the $\overline{p}p$ interaction cross section. Since there are no high-energy electron production mechanisms from light-quark interactions, a sample of high-energy electrons is expected to be rich in heavy quark events, and of these events the sample will contain mostly b decays, because b quarks typically produce higher-energy electrons than charm.

An additional advantage accrues to the study of bottom physics due to the bottom quark's large mass. Again, the momentum of the heavy quark is not changed

significantly by the low-energy—here below the QCD scale, $\Lambda_{QCD} \sim 300$ MeV—interactions within the hadron, the result being that the bottom quark largely decouples from the light diquark. The heavy quark is essentially at rest in the hadron rest frame and acts as a static gluon source. Hadron properties then become independent of the heavy quark's mass and spin. Similar symmetries arise in atomic physics due to the large nuclear mass: different isotopes have the same chemistry, since the electron cloud sees only the charge of the nucleus, and the hyperfine energy splittings are very small because of the small couplings between the electron and nuclear spins. These observations for quarks in hadrons have recently been formalized into what is known as Heavy Quark Effective Theory. [8] Corrections to the above symmetries are on the order of Λ_{QCD}/m_Q.

The heavy quark mass limit has been mostly explored for mesons with one heavy quark, since mesons are the most frequent fragmentation products, and large samples have been already been collected by experimenters. Among bottom baryons, the Λ_b is expected to be the most frequently produced—as well as being a daughter particle in Σ_b decays—with its ud diquark. The diquark is also spin-0, so that the baryon spin reflects the bottom quark spin.

The top quark, at 176 GeV/c^2, is of course much more massive than the bottom quark. However, its production rate is too small with present technology to admit large-statistics studies. In any case, since the top quark decays primarily through a bottom quark and a real W, an understanding of bottom quark physics is essential to studying top. The bottom quark is the heaviest and most copiously produced quark for the study of quark-level dynamics.

Spectator Model

A calculation of production rate and branching fractions requires the simulation of the particle and its decay in a detector model. It is therefore dependent upon the model of the decay itself.

Given that the bottom quark is largely independent of its light partners, the simplest reasonable model for Λ_b decay consists of decaying the bottom quark independently of other processes, and hadronizing the final quarks. This is called the "spectator model," since the light quarks do not participate in the actual decay. Though there have been a number of recent theoretical advances in the understanding of exclusive decays, such spectator models, in particular ones which include QCD corrections such as ACCMM [10], remain a benchmark, and we use it to compare with more sophisticated models. ACCMM has been useful in fitting inclusive single lepton spectra, and describes the data well where the $b \to c$ transition is important.

Our interest in the spectator model is primarily as an input into the decay simulation. We use the ACCMM ansatz, that the momentum of the bottom quark in the hadron rest frame is distributed according a normal distribution,

$$\phi(p) = \frac{4}{\sqrt{\pi} p_F^3} e^{-p^2/p_F^2} \tag{1.12}$$

where p_F is the "Fermi momentum." A fit to inclusive lepton data at $\Upsilon(4S)$ yields $p_F \approx 230$ MeV/c. [11] The statement that the bottom quark in the Λ_b would be less relativistic than in mesons would imply that p_F for the Λ_b would be smaller. However, for the purposes of this analysis, we assume that it is the same.

Exclusive Model

Two factors lead to the expectation that the exclusive decay $\Lambda_b \to \Lambda_c^+ e^- \overline{\nu}_e$, with its charge conjugate, dominate the Λ_b semileptonic decays to Λ_c observed at CDF. First, the decays with additional hadrons reduce the energy available to the electron. Second, of the available three-body decays, $\Lambda_b \to \Sigma_c^+ e^- \overline{\nu}_e$ is suppressed by isospin symmetry, and $\Lambda_b \to \Lambda_c^{*+} e^- \overline{\nu}_e$ requires the change of the relative angular momentum of the two light quarks with respect to one another, while the gluon interaction necessary for such a change is exactly that suppressed in the heavy quark limit. It should be noted that in the Λ_b the bottom quark partner is a spin-0 ud system, whereas in the meson case the b is paired with a single spin-$\frac{1}{2}$ light quark. Adding the two spins gives mesons with both spins 0 and 1, while for baryons, the sum is only spin-$\frac{1}{2}$. Thus, when relating decay widths between baryons and mesons, a $\Lambda_b \to \Lambda_c$ transition corresponds to the sum of $B \to D$ and $B \to D^*$. The $B \to D^{**}$ transitions, which change the relative angular momentum between the heavy quark and its partner, corresponds to a $\Lambda_b \to \Lambda_c^*$ transition in the baryon case. The $B \to D^{**}$ transition makes up at most about 30% of the semileptonic decay width of the B meson, the rest being taken up by higher resonances and nonresonant decays.

To model $\Lambda_b \to \Lambda_c^+ e^- \overline{\nu}_e$, we have used decay distributions derived by R. Singleton. [12]. He begins by writing the decay rate

$$d\Gamma(M_s \to m_{s'} e \overline{\nu}) = \frac{1}{2N} |A(M_s \to m_{s'} e \overline{\nu})|^2 d\Pi \tag{1.13}$$

where the M_s and $m_{s'}$ are the Λ_b and Λ_c, respectively, with masses M and m and spin components s and s'. The phase space factor is the familiar Lorentz invariant

phase space factor,

$$d\Pi = (2\pi)^4 \delta^{(4)}(P - k - p - p') \prod_f \frac{d^3\vec{k}_f}{(2\pi)^3 2E_f} \tag{1.14}$$

where the 4-momenta of the Λ_b and Λ_c are P and k, and that of the e and $\overline{\nu}$ are p and p'. The product is over the three final state particles, $\vec{k}_f$ representing their three-momenta. The invariant amplitude is factored into leptonic and hadronic currents,

$$A(M_s \to m_{s'} e\overline{\nu}) = \frac{G_F}{\sqrt{2}} V_{bc} L^\mu H_\mu^{s's}, \tag{1.15}$$

where G_F is the weak coupling constant and V_{bc} is the CKM matrix element. The leptonic current has the well known form,

$$L^\mu = \overline{u}_e \gamma^\mu (1 - \gamma^5) v_\nu, \tag{1.16}$$

while the hadronic current is constructed from Lorentz-invariant form factors:

$$H^{(s's)\mu} = < k, s' | J^\mu(0) | P, s > \tag{1.17}$$

$$J^\mu = V^\mu - A^\mu \tag{1.18}$$

$$< k | V^\mu(0) | P > = \overline{u}_m [g\gamma^\mu + g_+(P+k)^\mu + g_-(P-k)^\mu] u_M \tag{1.19}$$

$$< k | A^\mu(0) | P > = \overline{u}_m [a\gamma^\mu\gamma^5 + a_+(P+k)^\mu\gamma^5 + a_-(P-k)^\mu\gamma^5] u_M \tag{1.20}$$

where the spin labels have been suppressed in the last two equations. The form factors g, $g_\pm$, a, and $a_\pm$ are functions of the scalar $q^2 = (P-k)^2$, which is the squared mass of the virtual W.

Using standard four-component Dirac spinors with normalization $\overline{u}u = 1$ and averaging over the initial and final spins, the differential decay distribution becomes

$$\frac{d\Gamma}{dy\, d\cos\theta} = \frac{G_F^2 |V_{bc}|^2 K M^2 y}{2(2\pi)^3} \left[\left(\frac{1 - \cos\theta}{2} \right)^2 |H_+|^2 + \right.$$

$$\left(\frac{1+\cos\theta}{2}\right)^2 |H_-|^2 + \sin^2\theta |H_0|^2\Bigg] \tag{1.21}$$

where $y = q^2/M^2$ and θ is the angle the electron makes with the W direction, boosted into the W rest frame. K is the Λ_c momentum in the Λ_b rest frame,

$$K \equiv \frac{M}{2}\left[(1-\frac{m^2}{M^2}-y)^2 - 4\frac{m^2}{M^2}y\right]^{1/2}. \tag{1.22}$$

The $H_{0,\pm}$ amplitudes are the result of projecting the currents along longitudinal and transverse W helicity basis vectors,

$$H_\pm \equiv \pm(aF_0 \mp gF_-) \tag{1.23}$$

$$H_0 \equiv \{[2a(N-\frac{1}{2}F_0) - 2ka_+F_-]^2 + (2kg_+F_0 + gF_+)^2\}^{1/2} \tag{1.24}$$

where k is the Λ_c momentum in the W rest frame,

$$k = \frac{K}{\sqrt{y}}, \tag{1.25}$$

and the F and N coefficients are

$$N \equiv \left[\frac{(E_m+m)(E_M+M)}{4Mm}\right]^{1/2} \tag{1.26}$$

$$F_\pm \equiv N\left[\frac{k}{E_m+m} \pm \frac{k}{E_M+M}\right] \tag{1.27}$$

$$F_0 \equiv N\left[1 - \frac{k^2}{(E_m+m)(E_M+M)}\right] \tag{1.28}$$

where the energies are calculated in the W rest frame,

$$E_M = \frac{M}{2\sqrt{y}}\left[1-\frac{m^2}{M^2}+y\right], \tag{1.29}$$

$$E_m = \frac{M}{2\sqrt{y}}\left[1-\frac{m^2}{M^2}-y\right]. \tag{1.30}$$

Meson form factors have been calculated by N. Isgur, *et al.*(ISGW) [13], using a nonrelativistic quark potential model. Bound state effects are modeled by the valence quarks moving in a Coulomb-like potential. Using a similar technique, D. Scora has calculated form factors for heavy quark baryon decay, including those for $\Lambda_b \to \Lambda_c^+ e^- \overline{\nu}_e$. [14] He begins with different form factor definitions,

$$< k, s' | V_\mu | P, s > = \overline{u} \left[F_1 \gamma_\mu + F_2 \frac{P_\mu}{M} + F_3 \frac{k_\mu}{m} \right] u \tag{1.31}$$

$$< k, s' | A_\mu | P, s > = \overline{u} \left[G_1 \gamma_\mu + G_2 \frac{P_\mu}{M} + G_3 \frac{k_\mu}{m} \right] \gamma_5 u \tag{1.32}$$

these form factors being connected with Singleton's by the formulas,

$$g = \sqrt{4Mm} F_1 \tag{1.33}$$

$$g_\pm = \sqrt{4Mm} \left(\frac{F_2}{2M} \pm \frac{F_3}{2m} \right) \tag{1.34}$$

$$a = \sqrt{4Mm} G_1 \tag{1.35}$$

$$a_\pm = \sqrt{4Mm} \left(\frac{G_2}{2M} \pm \frac{G_3}{2m} \right). \tag{1.36}$$

The Hamiltonian is

$$H = \sum_{i=1}^{3} \left(m_i + \frac{p_i^2}{2m_i} \right) + \sum_{i<j} \left(\frac{1}{2} b r_{ij} + c - \frac{2\alpha_s}{3 r_{ij}} \right), \tag{1.37}$$

with $\vec{r}_{ij} = \vec{r}_i - \vec{r}_j$. The model parameters are taken to be $\alpha_s = 0.5$, $b = 0.18$ GeV^2, and $c = -0.485$ GeV, and the constituent quark masses $m_u = m_d = 0.29$ GeV$/c^2$, $m_c = 1.78$ GeV$/c^2$, and $m_b = 5.08$ GeV$/c^2$. He calculates the wavefunction by varying the parameters of the lowest two-dimensional harmonic oscillator state function to obtain the ground state. The form factors all have the form, letting F stand for vector or axial factors,

$$F_i = \overline{F}_i I_H \tag{1.38}$$

where I_H is

$$I_H = \left(\frac{\alpha_\rho \alpha_{\rho'}}{\alpha^2_{\rho\rho'}}\right)^{3/2} \left(\frac{\alpha_\lambda \alpha_{\lambda'}}{\alpha^2_{\lambda\lambda'}}\right)^{3/2} \exp\left[-\frac{3}{2}\left(\frac{m_\sigma^2}{Mm}\right)\frac{q^2_{max}-q^2}{\alpha^2_{\lambda\lambda'}}\right]. \tag{1.39}$$

In this expression, m_σ is the constituent quark mass, which is simply $m_u = m_d$ in our case, and $q^2_{max} = (M-m)^2$. The α's are the variational parameters, with the additional definitions

$$\alpha^2_{\lambda\lambda'} = \frac{1}{2}(\alpha^2_\lambda + \alpha^2_{\lambda'}) \tag{1.40}$$

$$\alpha^2_{\rho\rho'} = \frac{1}{2}(\alpha^2_\rho + \alpha^2_{\rho'}). \tag{1.41}$$

The form factor coefficients are as follows:

$$\overline{F}_1 = 1 + \frac{m_\sigma}{m_c}(1-\Delta) + \frac{m_\sigma}{m_b}(1+\Delta) \tag{1.42}$$

$$\overline{F}_2 = -\frac{m_\sigma}{m_c}(1-\Delta) \tag{1.43}$$

$$\overline{F}_3 = -\frac{m_\sigma}{m_b}(1+\Delta) \tag{1.44}$$

$$\overline{G}_1 = C_{gA} \tag{1.45}$$

$$\overline{G}_2 = -\frac{m_\sigma}{m_c}(1-\Delta) - \frac{m_\sigma^2}{m_c m_b}(1+\Delta)(1-\Delta) \tag{1.46}$$

$$\overline{G}_3 = -\frac{m_\sigma}{m_b}(1+\Delta) - \frac{m_\sigma^2}{m_c m_b}(1+\Delta)(1-\Delta) \tag{1.47}$$

where $C_{gA} = 0.987$ is a relativistic correction to the axial form factors, and with the definition

$$\Delta = \frac{\alpha^2_\lambda - \alpha^2_{\lambda'}}{\alpha^2_\lambda + \alpha^2_{\lambda'}}, \tag{1.48}$$

which is a measure of the wavefunction mismatch between the parent and daughter baryons. The variational parameters are calculated to be $\alpha_\rho = 0.39$ GeV and $\alpha_\lambda = 0.53$ for the Λ_b, and $\alpha_{\rho'} = 0.39$ GeV and $\alpha_{\lambda'} = 0.50$ for the Λ_c. Inserting all these elements into Equation 1.21, we arrive at a decay distribution in terms of the

four-momentum transfer y and the electron angle θ. Figure 1.9 shows the shape of this distribution with arbitrary normalization. The assymetry in $\cos\theta$ reflects the $V-A$ structure of the quark-level decay. We use this distribution to simulate $\Lambda_b \to \Lambda_c^+ e^- \overline{\nu}_e$.

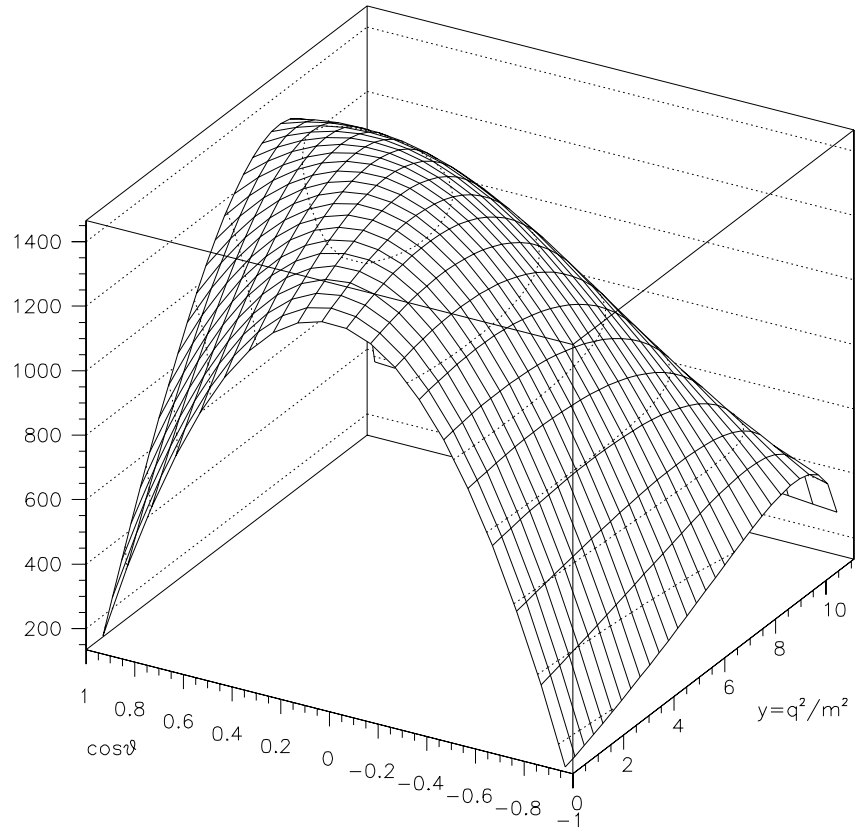

Figure 1.9: Singleton-Scora decay distribution for $\Lambda_b \to \Lambda_c^+ e^- \overline{\nu}_e$ as a function of y and $\cos\theta$.

Comparison to Data

ISGW is not a model with adjustable parameters to fit data, as is ACCMM. To compare ISGW with data requires the model calculation to be repeated for every contributing exclusive channel and summed, and every calculation results in a definite prediction. However, not all decay channels have yet been modeled, including those to baryons. CLEO has compared ACCMM and ISGW with the inclusive lepton energy spectrum at $\Upsilon(4S)$. [15] With two adjustable parameters, ACCMM fits the inclusive lepton spectrum well except for the high-energy tail, which is very sensitive to $b \to u$ transitions. ISGW, on the other hand, must be modified to admit a larger D^{**} contribution to the semileptonic width. This adjusted model is dubbed "ISGW**," and also fits the data well except for the high-energy tail. However, since both fit well the bulk of the spectrum, which is mostly dependent upon $b \to c$ transitions, we have some confidence that related calculations are appropriate to model Λ_b decay.

1.3 Rate Expectation

In this analysis, we identify electrons and fully reconstruct Λ_c's to obtain evidence for Λ_b production and semileptonic decay. The rate measurement will take the form of the product

$$f_{\Lambda_b}\mathrm{Br}(\Lambda_b \to \Lambda_c^+ e^- \overline{\nu}_e X)\mathrm{Br}(\Lambda_c^+ \to pK^-\pi^+) \tag{1.49}$$

which will be averaged over the decays listed and their charge conjugates. f_{Λ_b} is the probability of the fragmentation of the b quark resulting in a Λ_b, whether directly from hadronization or from the decay of more massive baryons such as Σ_b. It is generally assumed that 10% of the b quarks hadronize into baryons. If

we assume that all Σ_b's decay to Λ_b's, as all Σ_c's do to Λ_c's, and we neglect Ξ_b production, we can take this number as f_{Λ_b}.

The decoupling of the heavy quark with its partner light quarks implies that the semileptonic widths of all b hadrons are equal. Since the branching fractions are proportional to their total widths, which vary inversely with their lifetimes, we take

$$\mathrm{Br}(\Lambda_b \to \Lambda_c^+ e^- \overline{\nu}_e X) = \frac{\tau_{\Lambda_b}}{\tau_B} \mathrm{Br}(\overline{B} \to e^- X) \tag{1.50}$$

where we have neglected $b \to u$ transitions and other Λ_b semileptonic decays which do not produce Λ_c's. We can therefore take advantage of the inclusive measurement, [16]

$$\mathrm{Br}(\overline{B} \to e^- X) = (10.49 \pm 0.17 \pm 0.43)\%, \tag{1.51}$$

using dilepton events at $\Upsilon(4S)$. The lifetime ratio, τ_{Λ_b}/τ_B, is generally expected to be about 0.9, [17] but measurements have placed it lower. For our present estimate, we use the theoretical expectation. Combining all these numbers with the world average value for $\mathrm{Br}(\Lambda_c^+ \to pK^-\pi^+)$ of $(4.4 \pm 0.6)\%$ [1], we get

$$f_{\Lambda_b} \mathrm{Br}(\Lambda_b \to \Lambda_c^+ e^- \overline{\nu}_e X) \mathrm{Br}(\Lambda_c^+ \to pK^-\pi^+) = 4.6 \times 10^{-4}. \tag{1.52}$$

It should be noted that the Λ_c branching fraction is not well known. Most recent measurements, performed at e^+e^- machines at $\Upsilon(4S)$, neglect baryonic B decay modes besides those with the final state $\Lambda_c^+ \overline{N} X$. If such decay modes contribute significantly to B decay, $\mathrm{Br}(\Lambda_c^+ \to pK^-\pi^+)$ would increase. [18] CLEO [19] has performed another measurement, relating $\Lambda_c^+ \to pK^-\pi^+$ to $\Lambda_c^+ \to \Lambda \ell^+ \overline{\nu}_\ell$. Assuming that all c hadrons have the same semileptonic width, as we have assumed above for b hadrons, they calculate an upper limit on $\mathrm{Br}(\Lambda_c^+ \to pK^-\pi^+)$ to be $(6.67 \pm 0.35 \pm 1.35)\%$. A further assumption using the spectator model gives the

branching fraction

$$\mathrm{Br}(\Lambda_c^+ \to pK^-\pi^+) = (5.94 \pm 0.31 \pm 1.44)\%. \tag{1.53}$$

The world average quoted by the Particle Data Group simply averages these methods, but the nature of the measurements indicates that the branching fraction may indeed be higher, which would then increase the product of branching fractions we measure here.

Chapter 2

Experimental Apparatus

Experimental high-energy physics is, on the one hand, done very deliberately, marshalling sizable resources in order to build the equipment needed to concentrate large amounts of energy as well as extract precise measurements of small signals from complicated environments; and on the other hand, prone to reap additional and sometimes unexpected rewards. There is considerable interesting physics in that complicated environment. For this reason, each piece of equipment is actually a general-purpose device which can be used for many different analyses.

The process we are studying is as follows:

1. $\overline{p}p \rightarrow \overline{b}bX$ at $\sqrt{s} = 1.8$ TeV: a proton and an antiproton are accelerated to 900 GeV each and steered into a head-on collision, producing, among other things, a $\overline{b}b$ pair.

2. The b quark fragments into a Λ_b. For this analysis we take both charge-conjugate processes.

3. $\Lambda_b \rightarrow \Lambda_c^+ e^- \overline{\nu}_e X$: the Λ_b decays semileptonically to a Λ_c^+ and an electron.

4. $\Lambda_c^+ \rightarrow pK^-\pi^+$: the Λ_c^+ decays into three hadrons. This three-body decay includes decays via resonances such as K^{*0}, $\Lambda(1520)$, and Δ^{++}.

The first step is accomplished using the Fermilab Tevatron as a collider, which, as noted above, produces many different particles by many different processes. The following steps occur naturally on short time scales, and are not seen directly. Instead, they are inferred by the long-lived debris they produce. In this case, the debris consists of four particles, an electron, a proton, a kaon, and a pion, which must be sorted out from all the other activity in the event. We accomplish this with the Collider Detector at Fermilab (CDF). [20]

2.1 The Fermilab Tevatron

The process of achieving high-energy $\overline{p}p$ collisions is outlined in Figure 2.1, with the topology illustrated in Figure 2.2. It begins with electrical discharges in a hydrogen gas bottle, producing H^- ions. These are accelerated down a 150 m linear accelerator to an energy of 200 MeV. The two electrons are stripped off, and the protons are injected into the Booster ring, which is a circular accelerator with a circumference of 475 m. The Booster increases the energy to 8 GeV and then transfers the protons to the Main Ring, a larger circular accelerator, with a circumference of 6.3 km. The Main Ring again adds energy to the protons, this time increasing the energies to 150 GeV.

At this point, some protons are extracted from the Main Ring and smashed into a target. Among the collision products are antiprotons, which are guided into a storage ring for later use in $\overline{p}p$ collisions. When required, the antiprotons are reinjected into the Main Ring, and from there into the Tevatron.

The Tevatron is another circular accelerator built in the same tunnel as the

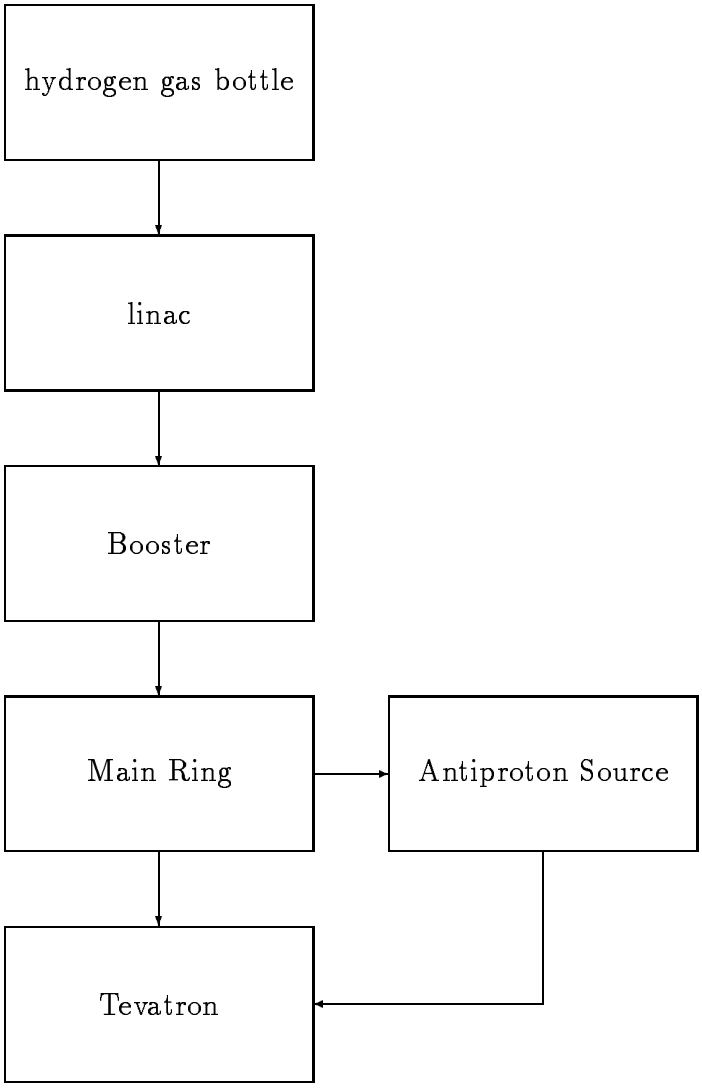

Figure 2.1: Elements in the generation and acceleration of protons and antiprotons at Fermilab.

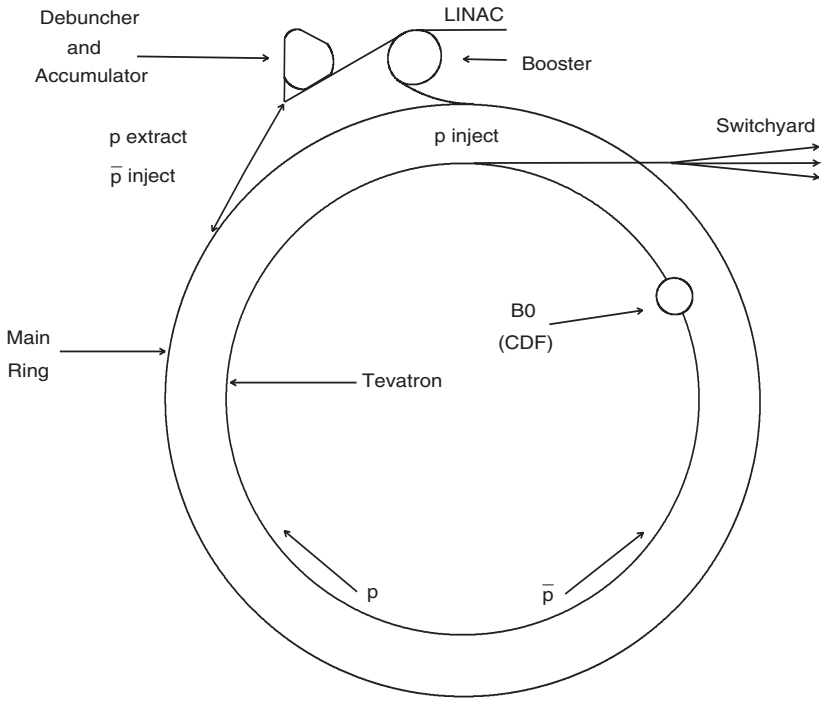

Figure 2.2: Schematic diagram of the Fermilab accelerators.

Main Ring. However, with the higher magnetic fields made possible with its superconducting magnets, the Tevatron increases the particle energies to 900 GeV. It is also, with the addition of electromagnetic separators, able to simultaneously accelerate counter-rotating proton and antiproton beams. Finally, the two beams are tightly focused to a radius of about 35 μm and guided to intersect at the B0 interaction region of the Tevatron. CDF is constructed around the nominal B0 interaction point. Along the beamline, the collisions occur within 30 cm of the nominal interaction point because of the length of the p and $\overline{p}$ bunches and the small intersection angle of the two beams. Furthermore, with the high beam intensities characteristic of the 1992-1993 data run, many beam crossings produced more than one collision.

2.2 The Collider Detector at Fermilab

CDF is a general purpose particle detector constructed and maintained by a multinational collaboration of high-energy physicists, with member institutions from the United States, Italy, Japan, Canada, and the Republic of China (Taiwan). As shown in Figure 2.3, it is nearly cylindrically symmetric with respect to the beamline, and forward-backward symmetric with respect to the nominal interaction point. It is equipped with high-resolution tracking chambers in a 1.4 T axial magnetic field provided by a superconducting solenoid, nearly 4π electromagnetic and hadron calorimeter coverage, and muon chambers. The quarter view schematic is shown in Figure 2.4. This analysis is limited to the central region, which roughly spans the pseudorapidity range $|\eta| < 0.8$ relative to the nominal interaction point,

where the pseudorapidity is defined to be

$$\eta \equiv -\ln \tan\left(\frac{\theta}{2}\right). \tag{2.1}$$

This region is where the tracking and calorimetry is best understood and most reliably calibrated. The following sections describe the parts of the detector used in this analysis.

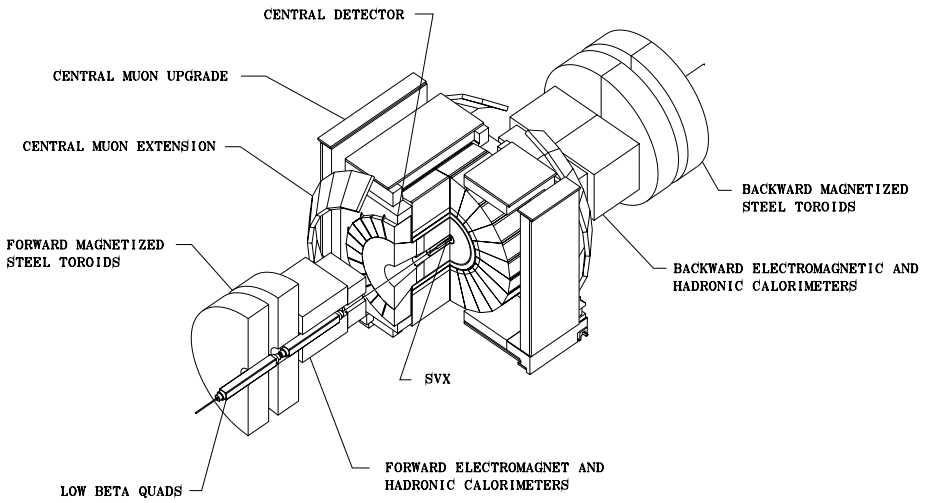

Figure 2.3: Isometric cut-away view of CDF, showing central, forward, and backward regions.

2.2.1 Beam-Beam Counters

Essential to any rate measurement is its normalization to some other, known rate. For CDF this normalization is provided by the beam-beam counters (BBC), which are scintillator paddles arranged around the beampipe in the forward and backward

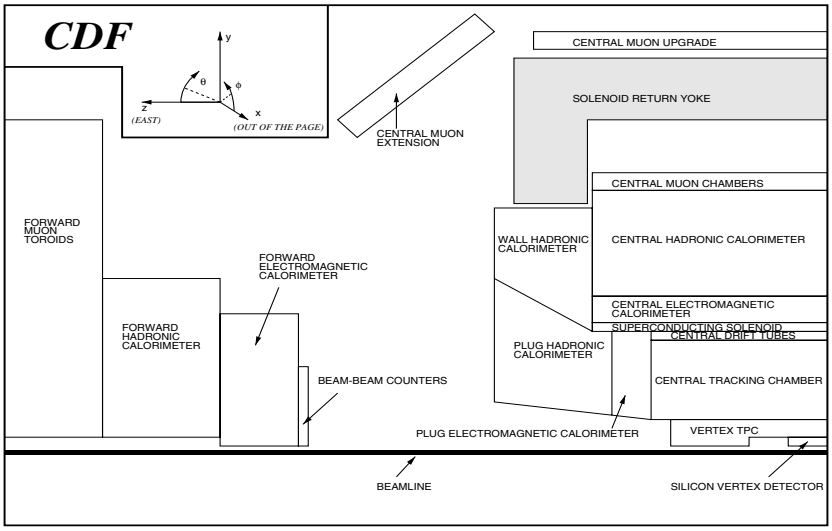

Figure 2.4: Quarter view of CDF, with global coordinate system. The central region used by this analysis includes the central tracking chambers and central calorimeters.

regions and covering a pseudorapidity range of roughly 3 to 6. The BBC provides a fast "minimum bias" trigger, and is a prerequisite for any other CDF trigger.

2.2.2 Tracking

Many bottom hadrons, including the Λ_b, are, by the standards of subatomic particles, long-lived—about 10^{-12} seconds, which is long enough for them to travel several hundred microns at their nearly light speed. Bottom events are therefore characterized by the existence of displaced vertices resulting from bottom decay. However, detectors cannot be placed within hundreds of microns from the interaction point because of the extreme radiation exposure; the tracks from these displaced vertices must be extrapolated from measurements made farther away. Successfully reconstructing bottom events requires precision tracking, which is an important feature of CDF.

In general, tracking a charged particle is accomplished by collecting the trail of ionization it leaves behind. The positions at which the charge is collected yields measurements along the particle's path, and these measurements are combined into a track. Because a "hit" is the result of ionization from a passing charged particle, neutral particles leave no tracks.

CDF tracking consists of three chambers. From the outermost to the innermost, they are the Central Tracking Chamber (CTC), the vertex time projection chamber (VTX), and the silicon vertex detector (SVX). The CTC is a open-cell gas-filled drift chamber: charged particles ionize gas molecules, and the resulting electrons and ions then drift along paths determined by the electric and magnetic fields and are picked up by wires strung along the chamber. The 84 radial wire layers are organized into five twelve-wire "axial" and four six-wire "stereo" superlayers. The axial layers are strung parallel to the beamline, giving $r\phi$ measurements along

the track, whereas the stereo layers are turned 3°. The two types of superlayers, used together, yield z information as well. The superlayers are further organized into cells which are rotated 45° relative to the radial direction to resolve left-right ambiguities when reconstructing tracks. The transverse position resolution of the CTC is 200 μm, and the longitudinal resolution about 1 mm. Inside the 1.4 T magnetic field, the CTC's momentum resolution is better than $\delta p_T/p_T^2 < 0.002(\mathrm{GeV}/c)^{-1}$. [20]

The VTX is another gas-filled drift chamber, except that the 24 wire layers are strung transverse to the beam, and provide rz position measurements. The VTX is primarily used to measure the z position of the $\overline{p}p$ collisions, and helps distinguish between tracks from different collisions in a single beam crossing.

The SVX, shown in Figure 2.5, consists of four layers of silicon microstrip detectors. The innermost layer is about 3 cm away from the beam, and the outermost 8 cm. On each detector face there are hundreds of metal strips, each separated by 55 or 60 μm. The bulk silicon is n-doped, but under each strip is a p-doped region, resulting in a high-density array of pn diodes. Passing charged particles excite electrons into conduction energy bands. The resulting charges and "holes" are swept out of the diode region by the electric fields and picked up by the metal strips. With its small radius and high strip density, the SVX is a high-resolution $r\phi$ tracker: its transverse impact parameter resolution is about 40 μm. This high resolution is necessary to identify non-primary decay vertices in an event.

The amount of ionization left by a charged particle is related to its energy loss. Since the energy loss is also related to the particle mass, given knowledge of the particle's momentum, measuring the amount of ionization is a handle on its identity. The CTC is instrumented to measure the ionization along the tracks. These measurements have been calibrated using electrons, since they are readily

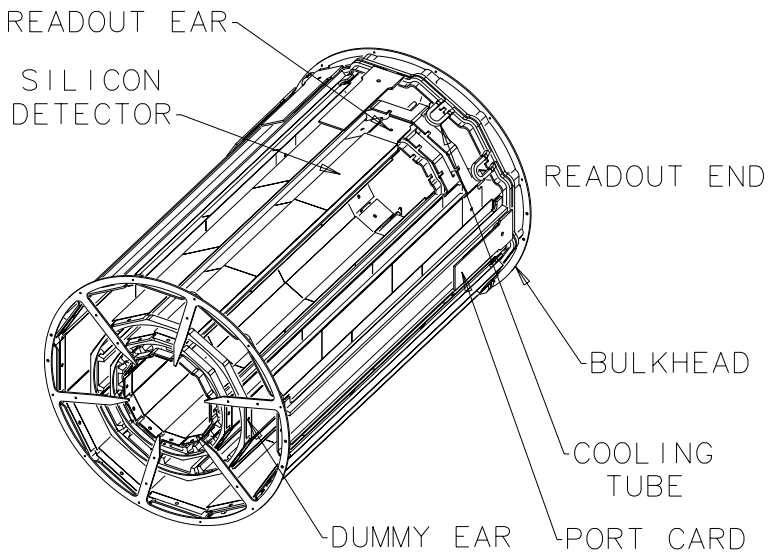

Figure 2.5: One SVX barrel, cut-away isometric view.

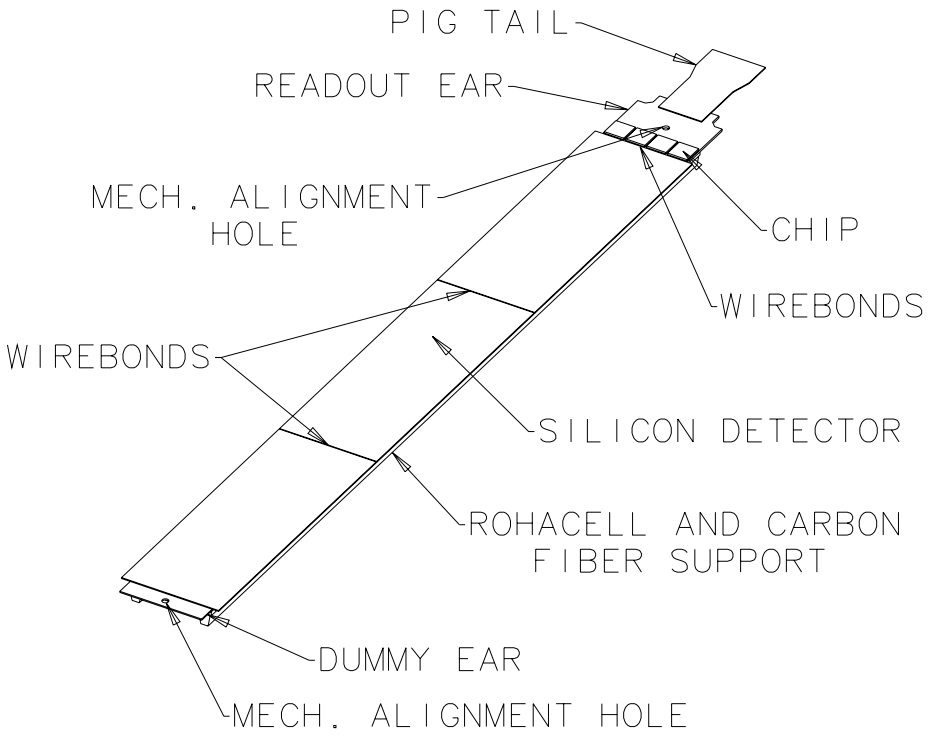

Figure 2.6: One SVX detector ladder, showing the three individual detector crystals, and readout chips.

identified and highly relativistic, due to their small mass. Because of this last characteristic, their dE/dx response is constant. After the corrections, the p/π separation in the relativistic rise region above about 1.7 GeV/c is roughly 1σ, and is used to distinguish proton candidates in this analysis.

2.2.3 Calorimetry

Outside the CDF tracking chambers lies the solenoid, and outside of that are the calorimeters, which absorb particles and provide measurements of the resulting energy deposition. The calorimeters also distinguish between different particle species by their energy loss characteristics. Most hadrons will lose their energy by nuclear interactions in the steel absorber of the hadron calorimeter. High-energy muons, on the other hand, tend to deposit little energy in absorbers and are instead detected outside the calorimeters. Photons tend to lose their energy quickly via pair production, and electrons via bremsstrahlung.

The characteristic length of electron energy loss due to electromagnetic interactions is roughly

$$X_0 = \frac{716.4 \text{ g cm}^{-2} A}{Z(Z+1)\ln(287/\sqrt{Z})}. \tag{2.2}$$

What is important is that the energy loss is larger per unit length for higher-Z absorbers, in contrast with the hadronic energy loss for which the characteristic length is very roughly

$$\lambda_I \approx 35 \text{ g cm}^{-2} A^{1/3} \tag{2.3}$$

due to nuclear interactions. In this case, energy loss is less for higher $A \propto Z$. This difference makes it advantageous to construct two kinds of calorimeter, an inner one made of high-Z absorber to detect electrons and photons, and a larger, outer one made of relatively inexpensive absorber to detect other particles. The CDF

inner calorimeter, the Central Electromagnetic Calorimeter (CEM), is constructed of lead absorber plates interspersed with plastic scintillator, while the outer one, the Central Hadron Calorimeter (CHA), is constructed of steel absorber and plastic scintillator. The plastic scintillator planes collect light from the showering particles and guide it to phototubes which convert the energy into electrical signals. The calorimeters are constructed in $\Delta\phi = 15^\circ$ wedges and arranged around the tracking chambers. One wedge is illustrated in Figure 2.7.

As a result of this construction, electrons and photons deposit most of their energy in the CEM, while hadrons do so in the CHA. The construction therefore provides a very quick signature for a high-energy electron or photon in an event, since it relies only on individual phototube measurements and requires only pedestal subtraction and threshold comparison. Electrons and photons are further distinguished by looking for a track pointing to the deposited energy. This distinction requires online track reconstruction with specialized trigger electronics described in Section 2.2.5.

The ratio of hadronic to electromagnetic energy deposition in the two calorimeters is used to distinguish between electrons and hadrons. However, some of the energy from the electromagnetic shower may leak into the hadronic calorimeter. Conversely, hadrons may interact with and shower in the CEM. Another significant difference between electrons and hadrons is the transverse size of their showers: electron showers tend to be small, a few centimeters across, whereas hadronic showers tend to be large, on the order of tens of centimeters across. The calorimeter geometry allows some checking of this transverse energy distribution. There is also a layer of wire proportional chambers (CES) near shower maximum in the CEM. The anode wires run along the z direction, measuring the shower profile in the $r\phi$ plane, whereas the cathode strips measure in the z view. The layout is

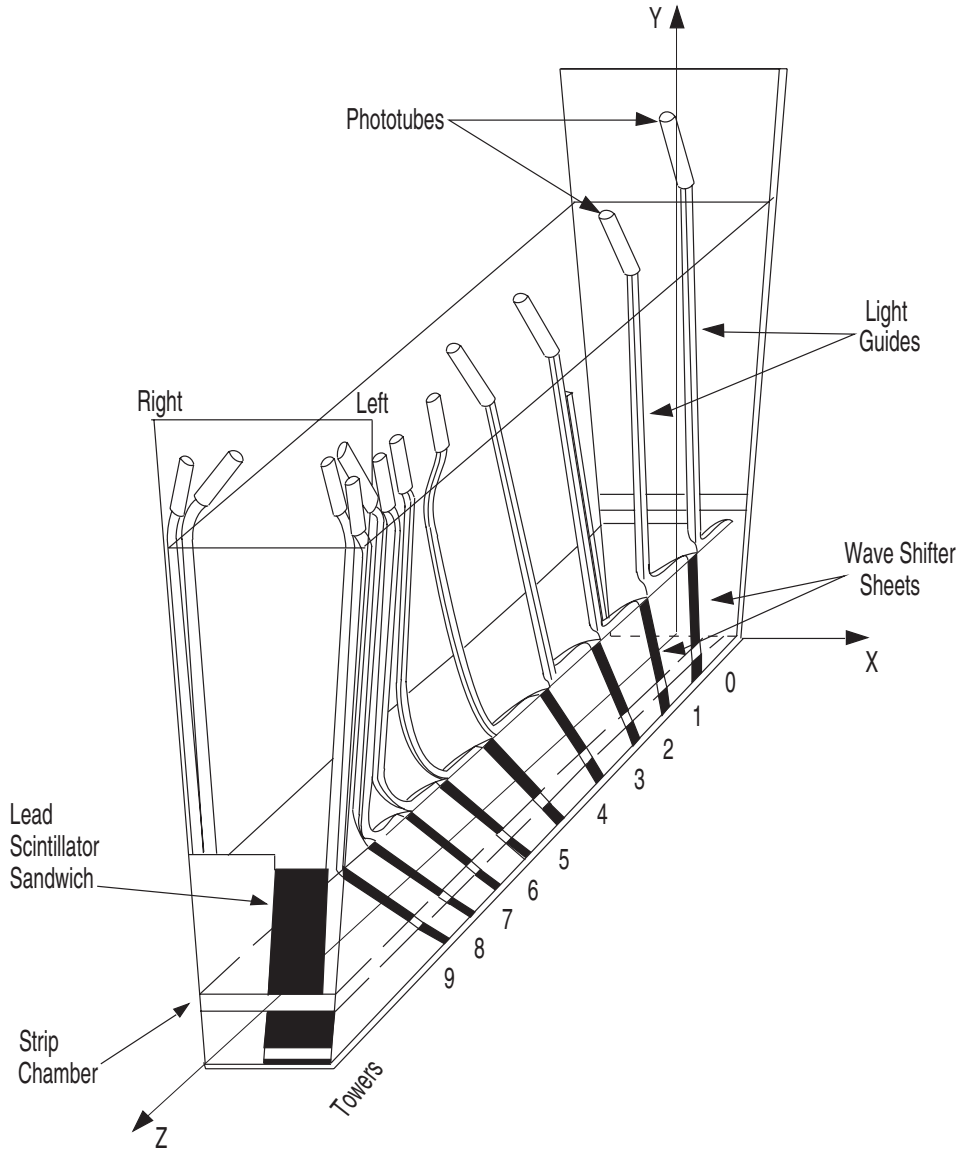

Figure 2.7: 15° calorimeter wedge. This drawing also shows the projective tower segmentation.

shown in Figure 2.8. The typical channel width is 1.5 cm, allowing good shower size, shape, and position measurement.

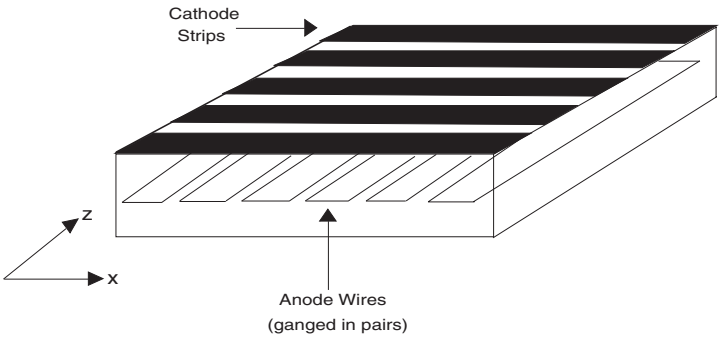

Figure 2.8: CES chamber, showing anode wires and cathode strips.

The calorimeters are further segmented in $\Delta\eta = 0.11$ projective towers, also shown in Figure 2.7. The towers point back to the nominal interaction point. This geometry minimizes the number of towers over which a shower develops. Furthermore, to keep the amount of material traversed by an electron shower constant over η, acrylic plates have replaced lead absorber in higher-η towers.

2.2.4 Muon Chambers

As noted the previous section, muons deposit little energy in the calorimeters, which completely absorb most other particles. An array of ionization chambers has been placed outside the calorimeters to detect muons. In addition, since these muons will have been deflected by the central magnetic field, their flight angle through the chambers provides a quick measurement of the muon p_T. As described in Section 3.6, this analysis uses the fact that some events passing the muon triggers also contain an electron which may or may not have passed the electron triggers.

This fact enables us to calculate the efficiency of the electron triggers.

2.2.5 Trigger

The total $\overline{p}p$ cross section is about 75 mb, which is orders of magnitude larger than the cross section of a process in which a typical non-minimum bias physics investigation is interested. This fact drives interaction rates and beam intensities higher, in order to generate more rare events. However, it is impossible to save all the data for all the resulting events; it is also useless to save it all if only 0.01% at most will be analyzed. Furthermore, it takes time to read and store 100,000 channels of data, time during which the detector cannot register data on subsequent, possibly more interesting, events. Therefore it is advantageous to implement event selection during data taking utilizing characteristics of these interesting processes, characteristics which occur infrequently for the typical beam interaction. High-energy leptons, for instance, are rare occurrences, and are characteristic of bottom semileptonic decay.

This on-line event selection process is accomplished at CDF with a four-layer trigger system. The multi-layer structure minimizes deadtime by using fast, relatively simple triggers to filter events for slower, more sophisticated triggers. Overall, the trigger system must reduce a 300kHz event rate to about 5Hz of potentially interesting events which are then recorded on magnetic tape. For this analysis, we use triggers designed to distinguish high energy electrons. We also use triggers which distinguish high energy muons in order to measure the electron trigger efficiency.

Level 0

The simplest trigger at CDF is a coincidence of hits in the BBC, indicating some form of $\overline{p}p$ interaction. In 1992-93 running conditions, however, the average collision rate was more than one per beam crossing, so this trigger essentially accepted every beam crossing.

Level 1

The first level of triggers must make its decision every beam crossing, that is, every 3.5 μs. Only the most elementary threshold comparisons are possible at this speed, and the trigger criterion relevent for this analysis is to look for a single CEM tower containing more than 8 GeV. There is also a lower threshold trigger at 4 GeV, but only one out of twenty events is passed. This artificial rate reduction is called a trigger "prescale," and is valuable for rate studies.

Events containing a muon candidate have been used to examine the behavior of the electron triggers. The Level 1 muon triggers look for hits in the muon chambers. Since the muons have been passed through the central magnetic field, the angle of the hits in the transverse plane yield a p_T measurement, and Level 1 requires a minimum p_T of 6 GeV/c.

Level 2

The second trigger level has more time to make a decision on keeping an event, and more sophisticated processing is therefore possible. Calorimeter towers may be joined into "clusters" which contain most of the energy of an individual shower. Prompt hits in the CTC may also be joined into preliminary tracks using the Central Fast Tracker (CFT).

The primary electron trigger at this level requires a 9 GeV CEM cluster, where the CHA energies in the same cluster contribute less than 12.5% of the total. A CFT track of at least 9.2 GeV/c must point to the cluster. Since this analysis uses all the electrons associated with this trigger, its threshold must be measured and parameterized. We do this using the muon triggers and the prescaled, lower-threshold electron trigger. The prescaled electron trigger looks for 6 GeV CEM clusters with the same CHA requirement, and a 6 GeV/c CFT track, and the prescale varies between 1, accepting all, and 10^4, depending on the instantaneous luminosity.

The muon triggers at this level match muon stubs reconstructed in the central muon chambers to CFT tracks within 5°.

Level 3

The Level 3 trigger consists of 48 Silicon Graphics computers. When Level 2 accepts an event, the event data is packaged and shipped to one of these computers, which then processes it in a manner similar to offline reconstruction. More sophisticated reconstruction may take place at this level. Calorimeter clusters are reclustered, and tracks reconstructed with the full CTC hit data. In addition, the CES data is analyzed to make sure that it is reasonably consistent with that expected from an electron shower, and that the shower position matches an extrapolated CTC track. Energy sharing between adjacent calorimeters is also checked. These cuts will be described in Chapter 3.

The Level 3 muon triggers also take advantage of the CTC track reconstruction and refine the match between the CTC track and the muon chamber hits. When Level 3 accepts an event, it is written to tape for further analysis.

Chapter 3

Electron Identification

Identifying the electron is the first step of this analysis. The electron is the most readily identifiable decay product of the Λ_b. Moreover, high-energy electrons are produced only in rare processes. For these reasons, as noted before, they are used as an on-line event selection criterion. However, the trigger uses loose cuts in order to be as inclusive as possible within the constraints of the data output rate. Tighter cuts are applied in this analysis to further purify the trigger-selected sample, while the eliminated data can be used for background studies. The cuts described in this chapter fall into three categories: those that make sure the electron candidate is well-measured, so that it does not pass cuts simply because of a bad measurement; those that make sure the candidate matches our expectations for electrons; and those that remove real electrons which originate from processes we know are unrelated to bottom decay.

3.1 Trigger Requirement

For the purposes of a rate measurement, we must select electron candidates from a sample for which we can measure an absolute efficiency. In this case we use the sample of events which caused a 9 GeV trigger at Level 2 as well as all the quality cuts described in this chapter. We measure its efficiency in Section 3.6.

3.2 Fiducial Cuts

The first cuts are those which make sure the electron candidate falls into regions where detector measurements are well understood. The first requirement is that the electron is in the central region of the detector: the tower number must be 6 or less. This corresponds to a detector pseudorapidity range of $|\eta| < 0.66$. More forward towers lack sufficient steel to entirely absorb hadronic showers within the CHA, yielding an inaccurate hadronic energy measurement, which is important for electron-hadron separation.

A uniform calorimeter response to electrons is necessary for a rate calculation. Certain calorimeter towers have been removed from consideration in order to maintain this uniformity. First, one calorimeter tower was physically removed to make way for electrical connections as well as the liquid helium input line to the solenoid; any "candidates" registered in this tower must therefore be spurious. Other towers have been removed from consideration due to known detector problems, such as low wire chamber voltage and shorted cables. After removing these towers, the electron rate should be uniform with respect to the ϕ for a given tower. Two towers were observed to give abnormally low rates relative to their neighbors, and were therefore also removed. The result is the desired uniform calorimeter response.

The local coordinate system for a given calorimeter wedge defines the z direction along the length of the wedge, increasing with $|\eta|$. The z axis runs down the center of the wedge, and the x direction is orthogonal to the z axis and the radial direction. This coordinate system is of most interest in the CES: the wire anodes give x measurements, and the strip cathodes give z measurements.

The CES is used to make sure that the candidate falls sufficiently far away from the wedge boundary, because there are inactive regions between the wedges. A study of CEM response shows that a margin of 1.6 cm is sufficient, and therefore a cut of $|x_{CES}| < 21.5$ cm is applied. [21]

The electron must also be well measured by the CES: for this to be true, the z_{CES} must fall between 9.0 cm and 200.0 cm. The joint between the two sections of strips falls at 121.2 cm, and therefore the region between 120.0 cm and 122.0 cm is also excluded.

3.3 Matching

The detector provides several checks to make sure that the electron candidate match expected electron behavior. These cuts divide into three categories: energy sharing, shower shape, and track matching.

3.3.1 Energy Sharing

We consider two kinds of energy sharing in the calorimeter: between towers, and between the CEM and CHA layers in the same tower. The CEM is constructed such that electromagnetic energy is not shared across ϕ boundaries.

A typical electron shower is only a few centimeters in diameter, and is well contained within a single tower, whereas hadronic showers tend to span several.

Towers may share the electron's energy if the electron enters the CEM near a tower boundary. An electron shower therefore has a distinct lateral energy profile, and a variable "Lshr," for lateral energy sharing, has been defined as a χ^2-like quantity,

$$\mathrm{Lshr}n = 0.14 \sum_k \frac{M_k - P_k}{\sqrt{0.14^2 E_{cl} + (\Delta P_k)^2}} \tag{3.1}$$

where the sum is over the $n-1$ adjacent towers. M_k is the measured energy in that tower, compared with P_k, the predicted energy given the CES z measurement. The resolution of the cluster electromagnetic energy measurement, E_{cl}, is $0.14\sqrt{E_{cl}}$, and ΔP is the change in P_k due to a 1 cm change in z. The Lshr variable can be defined for two or three towers. The adjacent tower in the two-tower case is its paired trigger tower—0 is paired with 1, 2 with 3, and so forth. The Lshr distributions are shown in Figure 3.1. Lshr2 is calculated by the Level 3 trigger, which applies the cut Lshr2 < 0.2. We apply the more stringent three-tower cut, Lshr3 < 0.2, offline.

A typical electron also deposits most of its energy in one or two towers of the CEM, whereas a hadron will deposit most of its energy in the CHA. We define the variable "Hadem" as the ratio of hadronic to electromagnetic E_T measurements, and again there are two-tower and three-tower varieties. The distributions are shown in Figure 3.2, in which can be seen the long tails due to shower leakage. The Level 2 trigger requires Hadem2 < 0.125. Offline, we make a tighter cut on the three-tower quantity, Hadem3 < 0.1.

Because hadrons produced close to the electron will obscure the Hadem measurement, the Hadem cut is an implicit isolation cut. Since we are looking for electrons from b decay, the electrons will be produced in association with hadronic jets resulting from the b fragmentation. If the electron is buried within the jet, it will be not be detected.

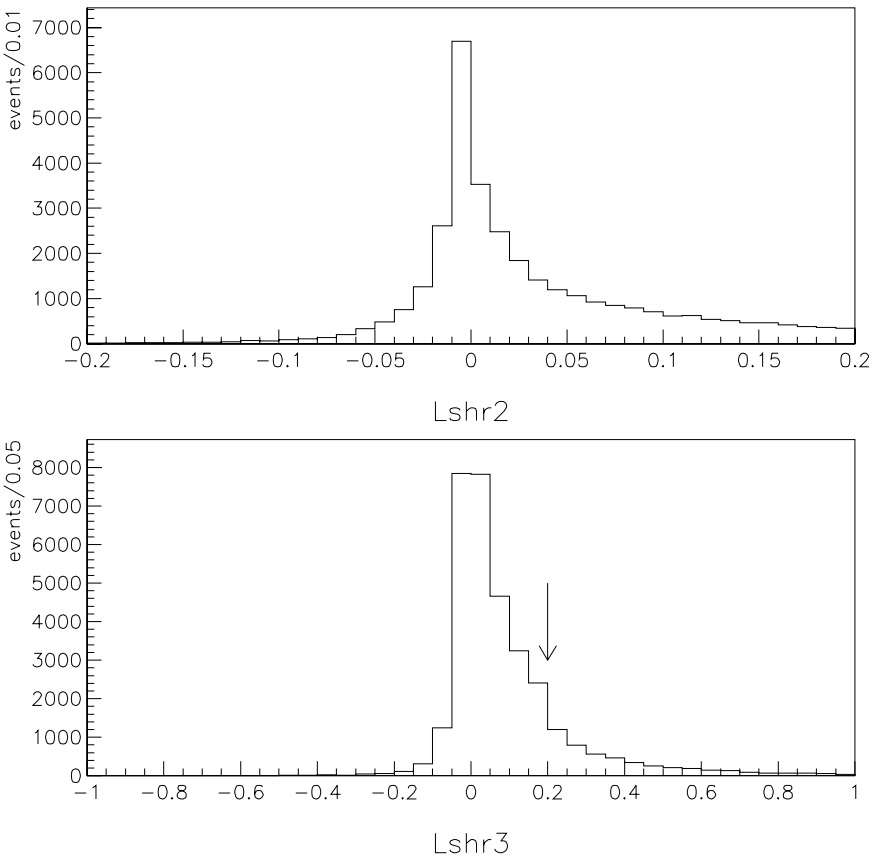

Figure 3.1: Lshr distributions after other cuts have been applied. The Level 3 trigger applies the cut Lshr2 < 0.2. The more stringent cut, Lshr3 < 0.2, shown by the arrow, is applied offline.

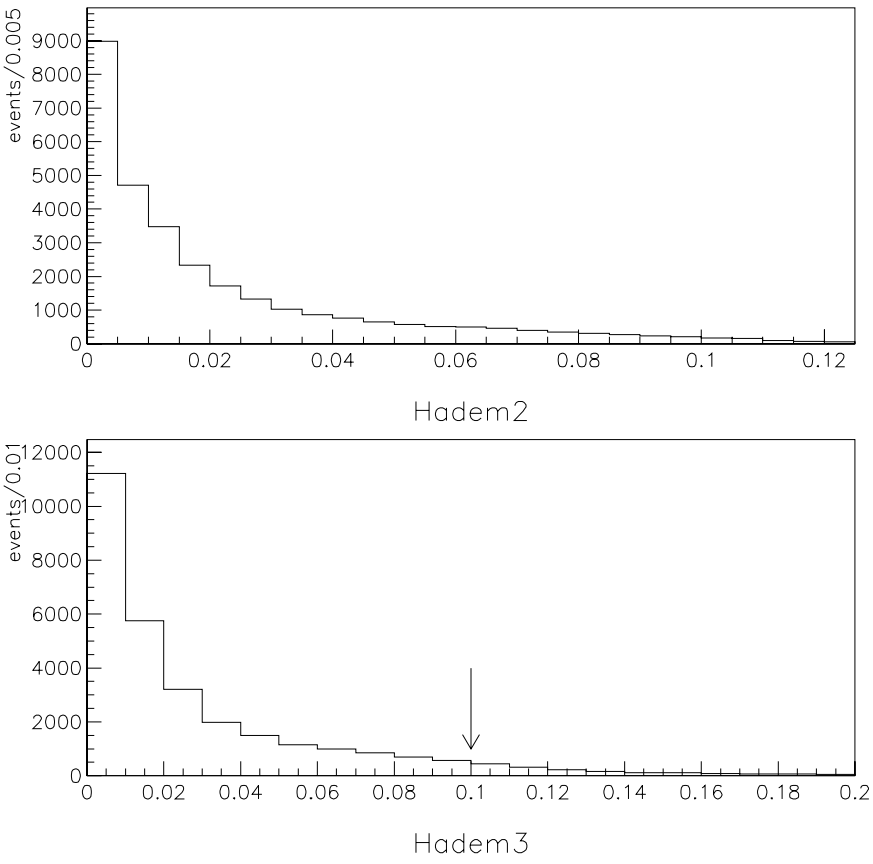

Figure 3.2: Hadem distributions after other cuts have been applied. The trigger cut is Hadem2 < 0.125, whereas the offline cut is Hadem3 < 0.1 as shown in the lower figure.

3.3.2 Shower Shape

The CES provides orthogonal views of the shower in the CEM. A typical shower will be measured by several adjacent CES channels, and therefore these two views can be compared with measurements performed in a test beam. [22] A measure of the match is provided by a χ^2 formula:

$$\chi^2 = \frac{1}{4}\sum_{i=1}^{11}\frac{(q_i^{obs} - q_i^{pred})^2}{\sigma_{q_i}^2}, \tag{3.2}$$

where the q_i are normalized pulse heights and σ_{q_i} the uncertainties. A cut on χ^2 distinguishes electrons from hadrons because of their differing shower developments. The trigger uses the cuts $\chi^2 < 10$ in the strip view and $\chi^2 < 15$ in the wire view. The distributions are shown in Figures 3.3 and 3.4. We cut slightly tighter offline at $\chi^2 < 10$ in both views.

Eleven channels are used in a CES cluster to distinguish individual electron showers from photon pairs from π^0 decay. These photon pairs are typically separated by several centimeters, and are therefore generally contained in the same cluster, but with large χ^2's.

3.3.3 Track-cluster Matching

Since the electron leaves a track in the central trackers, hits in the CES, and energy in the calorimeter, we have three measurements of the same particle in three complementary detectors. The best strip cluster in the CES is taken to be the highest-energy cluster consistent in position with the calorimeter cluster, and similarly for the best wire cluster. The best track is the highest-p_T track pointing to any tower in the cluster. The trigger requires the CEM energy to exceed 9 GeV, and that the track have $p_T > 6$ GeV/c. The number of fully reconstructed CTC tracks pointing to the calorimeter cluster is plotted in Figure 3.5. To make sure that

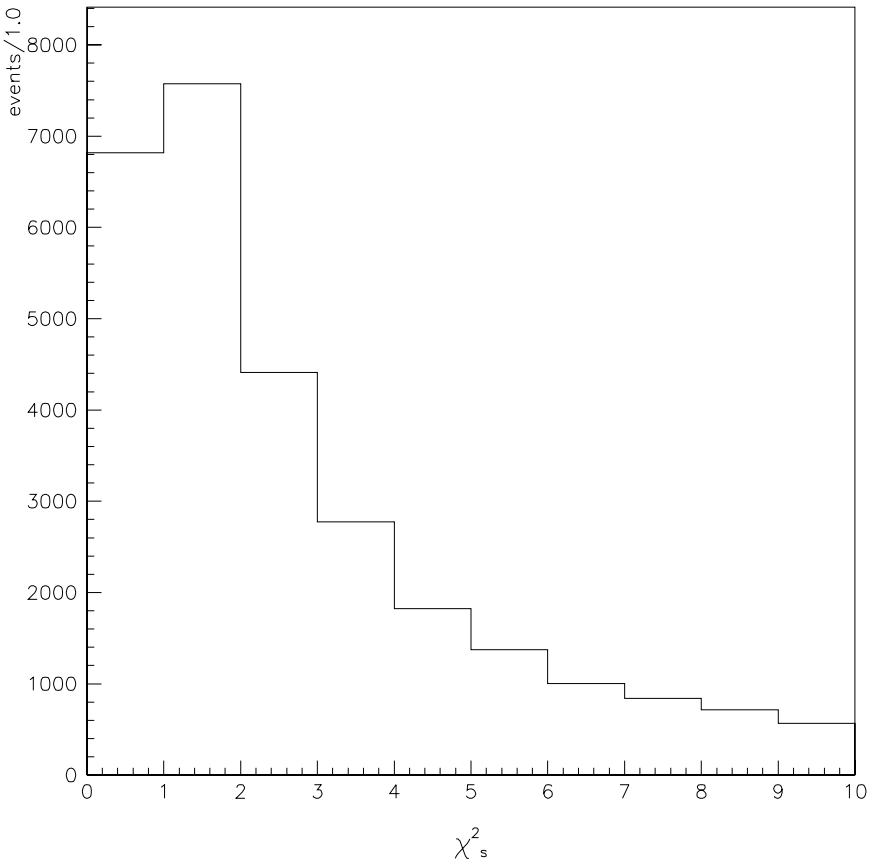

Figure 3.3: Strip-view shower shape χ^2 after other cuts. The trigger cut is $\chi^2 < 10$.

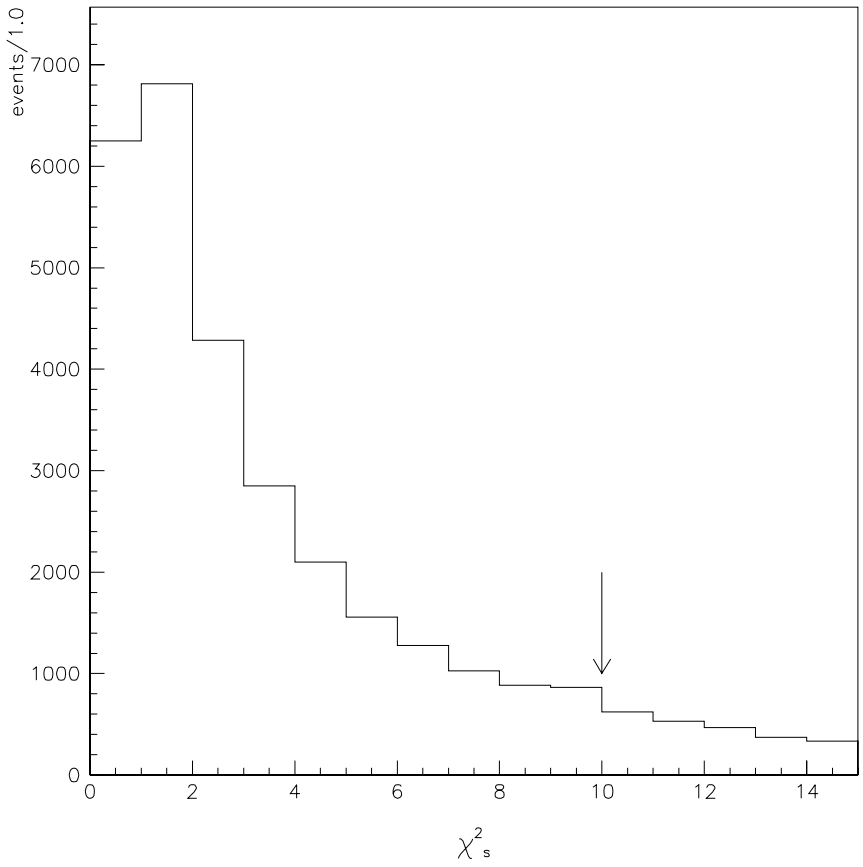

Figure 3.4: Wire-view shower shape χ^2 after other cuts. The offline cut is $\chi^2 < 10$.

the energy measurement is not significantly contaminated by nearby hadrons, only one additional track is permitted to point to the calorimeter cluster. Furthermore, since we will use the SVX to reconstruct the charm hadron, we require that the electron has been tracked in the SVX.

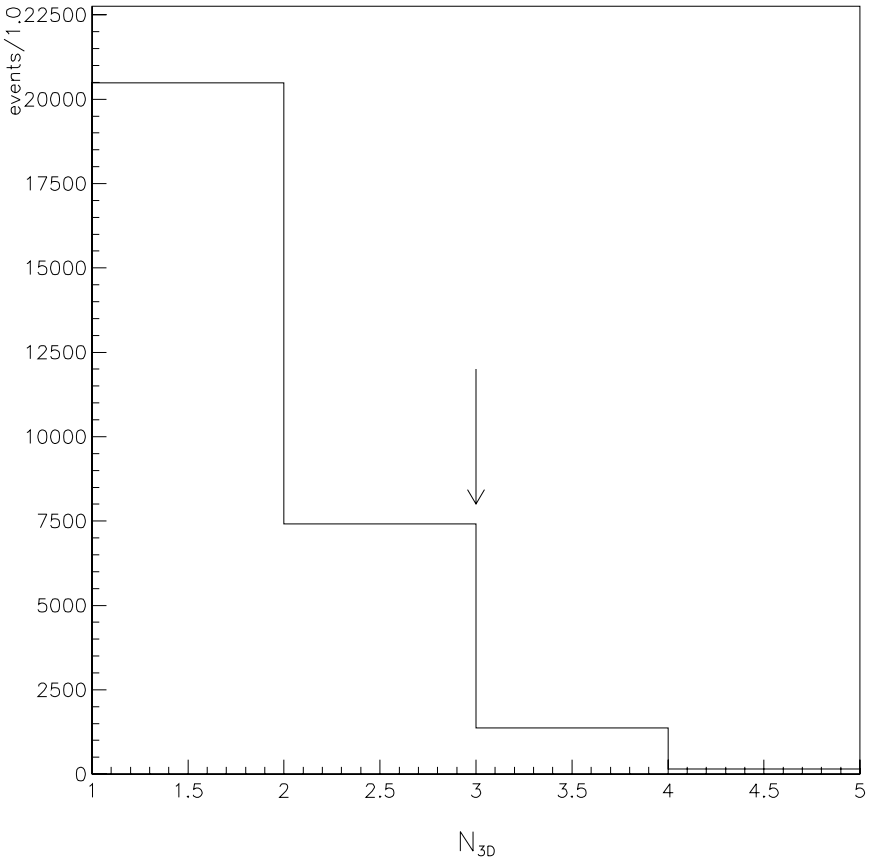

Figure 3.5: Number of tracks pointing to CEM cluster. The cut, shown by the arrow, allows at most one additional track.

To compare the track with the CES position measurements, the track is extrap-

olated to the CES. The mismatch between the CES cluster and the extrapolated track is shown in Figures 3.6 and 3.7. The x, or wire, view must be consistent within 2 cm, and the z, or strip, view within 3 cm.

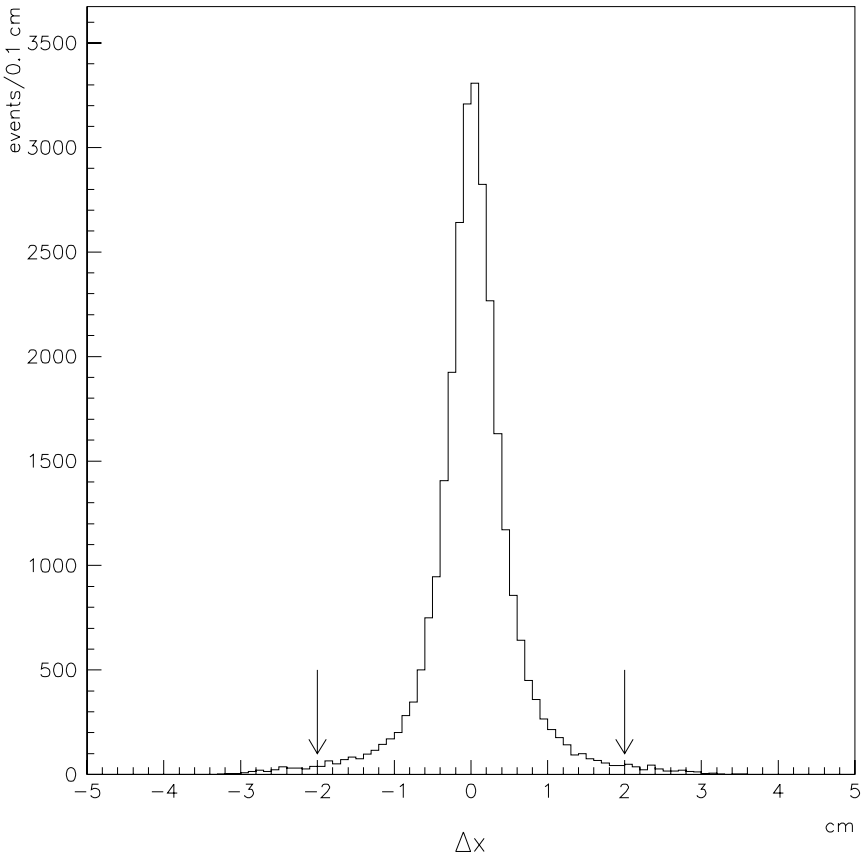

Figure 3.6: Wire-view difference between shower position and track extrapolation to CES. The arrows indicate the selected events.

The measured energy and momentum of the electron candidate may also be compared. Figure 3.8 shows the E_T/p_T distribution after all the other cuts. It is

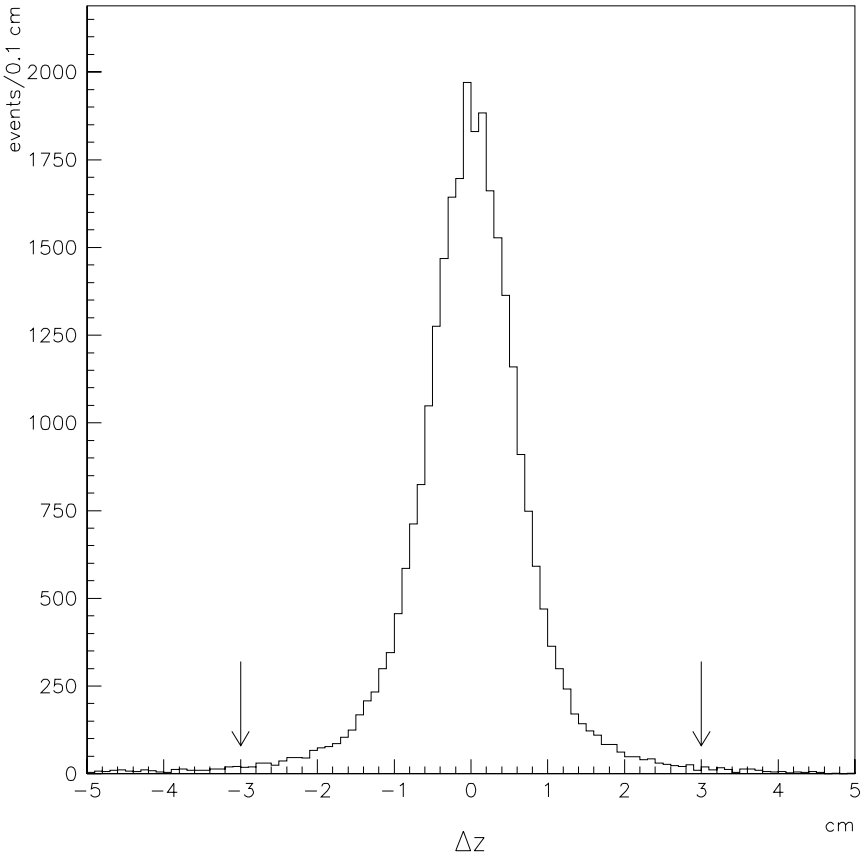

Figure 3.7: Strip-view difference between shower position and track extrapolation to CES. The arrows indicate the selected events.

peaked at unity, as expected. We require that the E_T be not more than twice the p_T.

3.4 W Removal

The decay of a real W boson to an $e\overline{\nu}_e$ pair is characterized by a very isolated high-energy electron produced in an event with large missing energy due to the undetectable neutrino. We select events with electron E_T exceeding 25 GeV and missing transverse energy greater than 20 GeV directed into the opposite ϕ-hemisphere as the electron. The isolation requirement is that the towers bordering the electron cluster contain less than 2 GeV in total E_T. The electron is also required to originate from near the primary vertex, as would be expected for W decay, in this case within 0.3 cm. If the event passes all these cuts, it is removed as a W candidate.

3.5 Conversion Removal

Another background source of electrons is that of photon conversions to e^-e^+ pairs. In these events, the two leptons are produced nearly parallel to one another. We scan through the other tracks in the event and calculate $\Delta\cot\theta$ between them and the candidate electron track, and the quantity S, which is the transverse separation between the electron and partner track where the two tracks are parallel in the transverse plane. Conversions are characterized by small $\Delta\cot\theta$ and S. These quantities are shown in Figure 3.9. There is a clear excess of nearly parallel tracks at small $\Delta\cot\theta$. This excess is attributed to photon conversions. We therefore identify conversions with the cuts $|S| < 0.2$ cm and $|\Delta\cot\theta| < 0.06$ and eliminate them from our data sample. This elimination leaves some residual conversions,

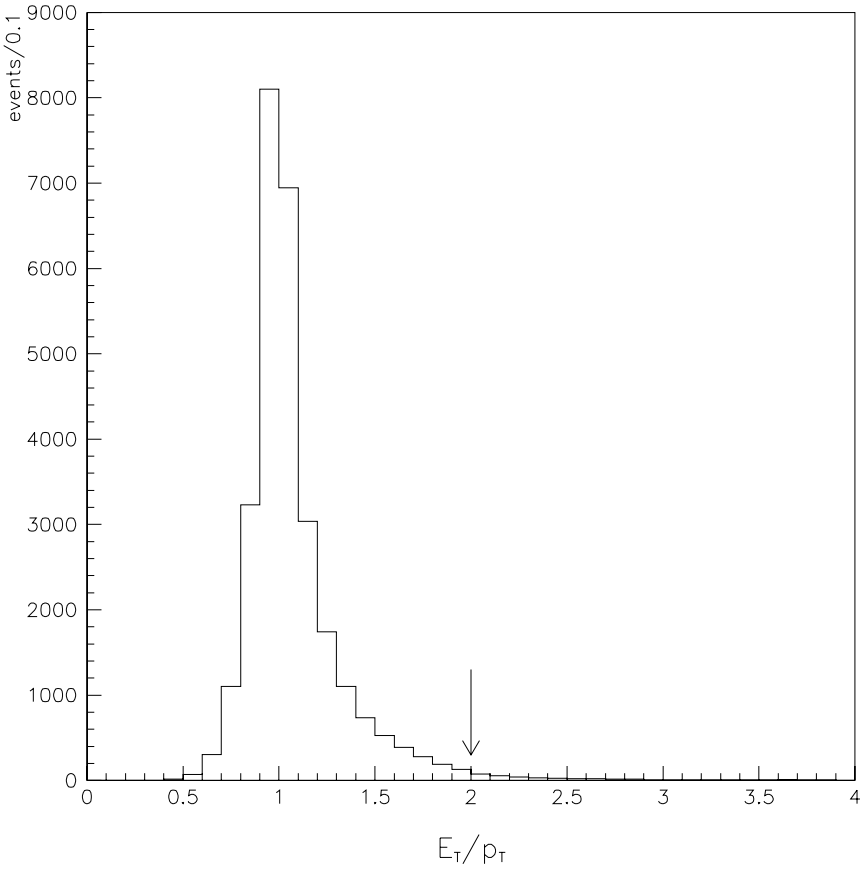

Figure 3.8: Ratio of the electron transverse energy, as measured in the calorimeter, and transverse momentum, as measured from the CTC track. The cut selects events below the arrow, with $E_T/p_T < 2$.

mostly due to the failure to reconstruct the partner track.

Since photons can only convert near matter, plotting the radius at which conversions occur yields Figure 3.10 in which features of the inner tracking chambers can be clearly seen.

3.6 Level 2 Trigger

The Level 2 trigger response is modeled from data by counting events passing the 9 GeV trigger within some parent sample. For the shape of the turn-on, the pre-scaled 6 GeV trigger sample is used as the parent sample. For the absolute normalization of the plateau, the muon trigger sample is used, where the muon is in a different ϕ wedge from that of the electron in the event. The trigger parameterization is the product of two error functions which model the separate calorimeter and CFT turn-ons, with low-energy and high-energy plateaus

$$P_{\mathrm{CEM9}}(E_T) = A\left[(1-B)\mathrm{freq}\left(\frac{E_T-\mu_1}{\Gamma_1}\right)\mathrm{freq}\left(\frac{E_T-\mu_2}{\Gamma_2}\right)+B\right], \tag{3.3}$$

where the function $\mathrm{freq}(x)$ is defined in terms of the standard error function $\mathrm{erf}(x)$,

$$\mathrm{freq}(x) = 1+\frac{1}{2}\mathrm{erf}(x). \tag{3.4}$$

A binomial likelihood function is used to the fit the data,

$$\log\mathcal{L} = \sum_i \left[n_i \log P_{\mathrm{CEM9}} + (m_i - n_i)\log(1-P_{\mathrm{CEM9}})\right], \tag{3.5}$$

where m_i are the number of 6 GeV or muon triggers in the bin i, and n_i the number of events firing both the parent trigger and the 9 GeV trigger in that bin. The fits are shown in Figure 3.11.

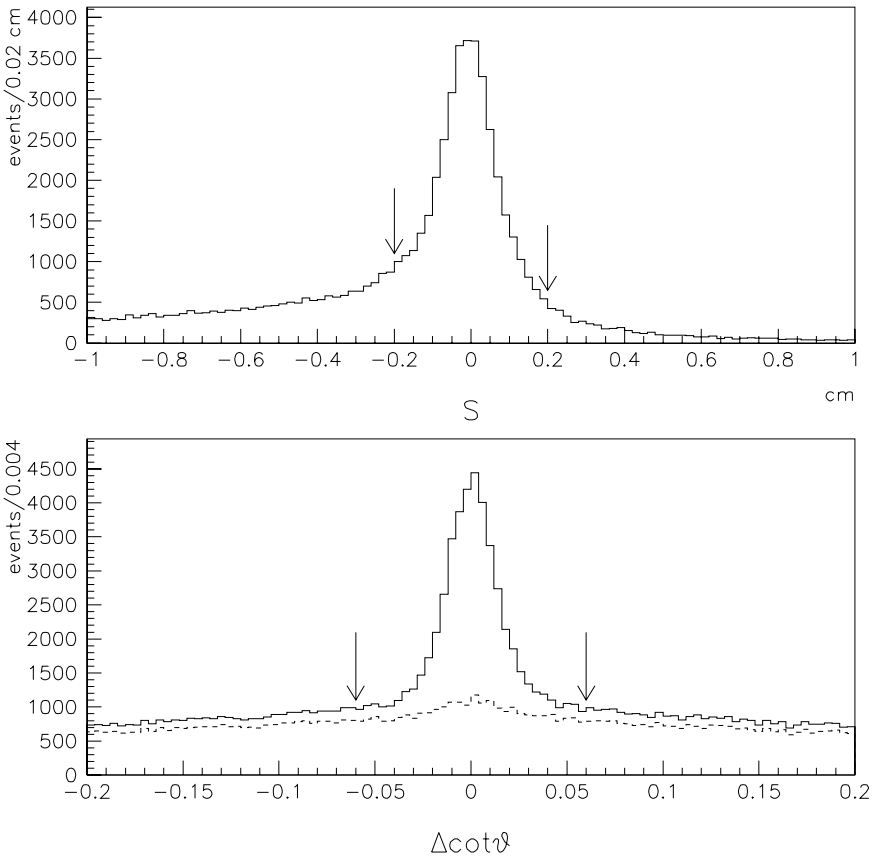

Figure 3.9: Top: transverse separation, $|S|$, of the nearest partner track to the electron. $S > 0$ cm indicates non-intersecting helical tracks. The distribution is skewed negative because most tracks do intersect. Bottom: $\Delta \cot \theta$ distribution for nearest partner tracks (solid), and for those with $|S| > 0.2$ cm. In both plots the arrows show the conversion identification cuts.

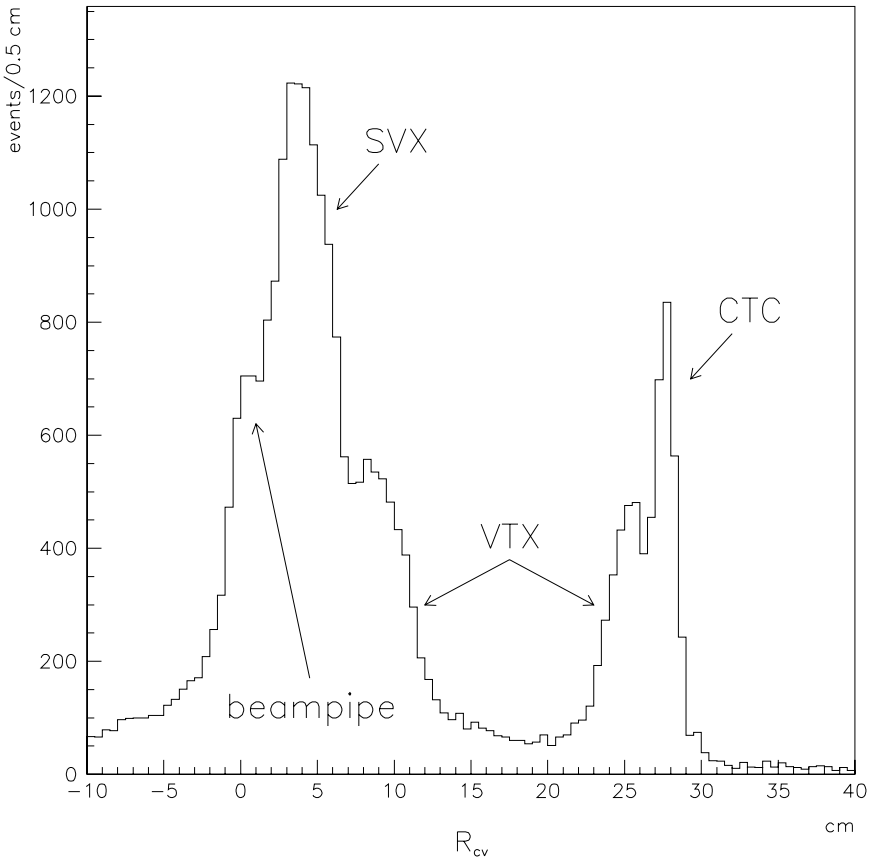

Figure 3.10: Radial profile of the detector from identified photon conversions.

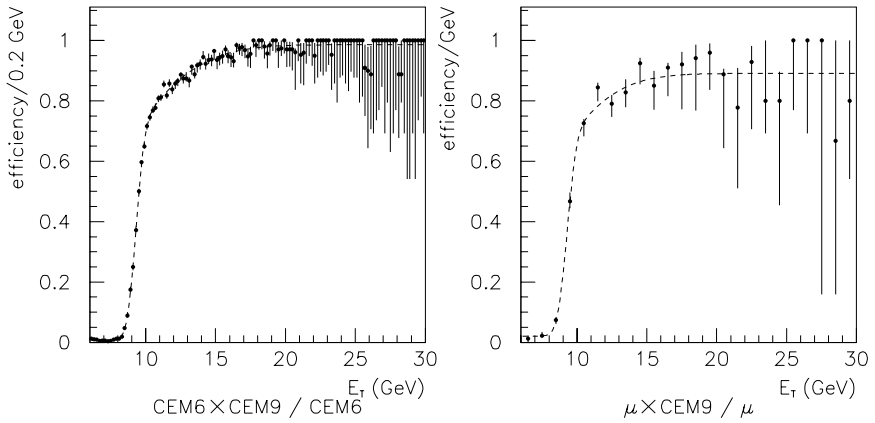

Figure 3.11: Number of CEM9 triggers within the parent trigger samples, divided by the number of parent triggers, for the CEM6 parent trigger (left) and the muon parent trigger (right). The curve is the parameterized fit, $P_{\mathrm{CEM9}}(E_T)$, to these binned efficiency measurements of the Level 2 CEM9 trigger.

3.7 Summary

The electron identification cuts are summarized in Tables 3.1 and 3.2. After these cuts, there are 282027 electron candidates with an E_T spectrum shown in Figure 3.12. The events containing these electron candidates is the data sample in which we will look for Λ_c's.

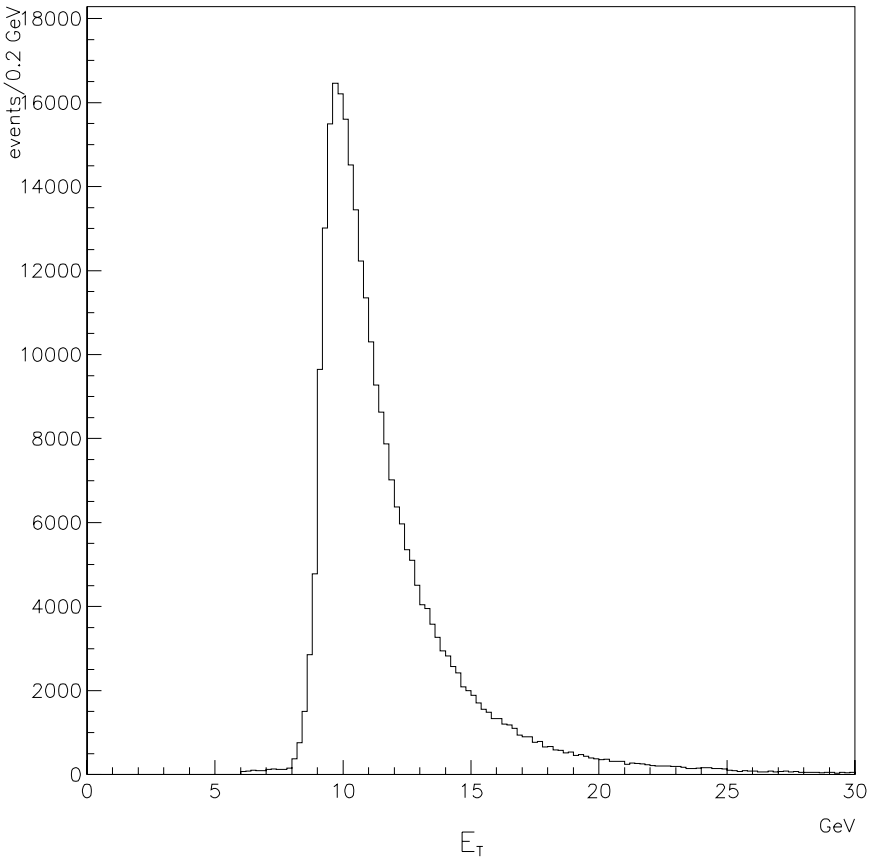

Figure 3.12: Electron E_T spectrum after all cuts except for the E_T cut.

Trigger	9 GeV
Fiducial	towers 0 to 6
	$\lvert x_{CES}\rvert < 21.5$ cm
	$\lvert z_{CES}\rvert \in (9, 120)$ cm or $\lvert z\rvert \in (120, 200)$ cm
Energy sharing	Level 3 Lshr2 < 0.2
	Level 3 Hadem2 < 0.125
	Offline Lshr3 < 0.2
	Offline Hadem3 < 0.1
Shower shape	$\chi^2_s < 10$
	$\chi^2_w < 10$
Track-cluster matching	1 or 2 tracks pointing to the cluster
	$\lvert\Delta x\rvert < 2.0$ cm
	$\lvert\Delta z\rvert < 3.0$ cm
	$E_T/p_T < 2.0$
	highest-p_T track has an SVX link
	$E_T > 9.0$ GeV
	$p_T > 6.0$ GeV

Table 3.1: Electron identification cuts.

W electron removal	$E_T > 25$ GeV
	missing $E_T > 20$ GeV, direction opposite electron in ϕ
	border $E_T < 2$ GeV
	electron track impact parameter $d_0 < 0.3$ cm
Conversion electron removal	$\lvert S \rvert < 0.2$ cm
	$\lvert \Delta \cot \theta \rvert < 0.06$

Table 3.2: Identification cuts for removing W and conversion electrons.

Chapter 4

Event Reconstruction

The distinctive features of Λ_b semileptonic decay are the Λ_c and the electron, and that they are produced with opposite charges. Therefore we look for Λ_c's in the data sample of electron candidates: there should be an excess of $e^-\Lambda_c^+$ and $e^+\Lambda_c^-$ ("right-sign") pairs over $e^-\Lambda_c^-$ and $e^+\Lambda_c^+$ ("wrong-sign").

To find Λ_c candidates, we use the decay mode $\Lambda_c^+ \to pK^-\pi^+$. This decay mode yields three long-lived charged particles which can easily pass through the CTC volume. On the other hand, the Λ_c has a lifetime of only 60 μm. If it is in the proper fiducial region, its decay products will also pass through the SVX. We use the SVX-CTC tracks to reconstruct Λ_c candidates, taking advantage of the CTC's momentum resolution and the SVX's tracking resolution to purify the resulting sample.

4.1 Track Reconstruction

Charged track reconstruction at CDF begins by reconstructing the track stubs in each of the CTC superlayers. These stubs are then joined into CTC tracks,

starting from stubs in the outermost superlayer. For the purpose of eventually calculating the CTC track reconstruction efficiency, we require that the track exit the chamber at a radius greater than 130 cm, thus ensuring that the track has crossed all superlayers. In the 14.116 T axial magnetic field, this cut implicitly requires that the track have $p_T > 280$ MeV/c, but we use a higher threshold, 450 MeV/c, above which the tracking efficiency is well understood. [26]

Joining the stubs into tracks also resolves the left-right ambiguity inherent in stub reconstruction, since an individual wire cannot tell from which side the ionization originated. Resolving this ambiguity is further assisted by the CTC geometry. With the wire cells tilted 45° with respect to the radial direction, the alternate stubs typically have significantly different impact parameters which prevent their linking with stubs in other superlayers.

Multiple hits on a single wire are the leading cause of hit inefficiency. Regions of high track density, such as in jets, therefore yield lower tracking efficiency. Indeed, for tracks with $p_T > 450$ MeV/c, the CTC tracking efficiency can be parameterized as a function of the number of overlaps with another track in the event, as described in Section 6.2.2. We therefore impose the same requirement on the tracks in this analysis. A further manifestation of this inefficiency is that the inner superlayers are often unusable for track reconstruction, not only because of the higher density characteristic of smaller radii, but also because of the plethora of low-p_T particles which cannot be reconstructed. The SVX, with its considerably higher sense wire density, can therefore significantly improve CTC track measurements.

A well-measured CTC track typically has an impact parameter resolution of about 350 μm. SVX tracks are reconstructed by searching for SVX hits within a 4σ road around the extrapolated CTC track, starting from the outermost layer and working inwards, re-extrapolating the track with each additional hit. The

resulting SVX track typically has an impact parameter resolution of about 50 μm. The reconstruction algorithm admits the possibility of mis-steering a track by associating spurious SVX hits with the CTC track. However, this effect is limited by the 4σ road. We also apply a track fit χ^2 cut of 6 per hit, and require that four SVX hits may be expected for the track. This requirement defines the fiducial volume for which the SVX tracking efficiency is defined.

4.2 Vertexing

The short lifetime of the Λ_c not only allows us to require that our tracks include SVX information, but also to consider the tracks only on short distance scales—that is, as straight lines, ignoring the curvature induced by the magnetic field. This approximation allows us to use a simple least-squares fit to vertex three tracks.

To reconstruct the Λ_c, we use tracks which fall within the z region $|z_0 - z_e| <$ 6 cm, where z_0 is the z of the track at its point of closest approach to the z axis, and z_e is the z_0 of the electron track. This cut eliminates tracks from other collision vertices in the beam crossing. As shown in Figure 4.1, tracks from the same collision vertex fall well within this window. We also eliminate some tracks from consideration by requiring that the combined invariant mass of the electron and the track, assigning the track the π^+ mass, is less than 6.5 GeV/c^2. This cut eliminates tracks which are inconsistent with b quark semileptonic decay. As shown in Figure 4.2, 6.5 GeV/c^2 is well above the corresponding mass distributions for the Λ_c daughters. Since the cut is used only to reduce computing time by eliminating tracks from consideration, we are only concerned that it be fully efficient for reconstruction, and make no attempt to optimize it.

We loop through all the remaining tracks, forming three-track combinations

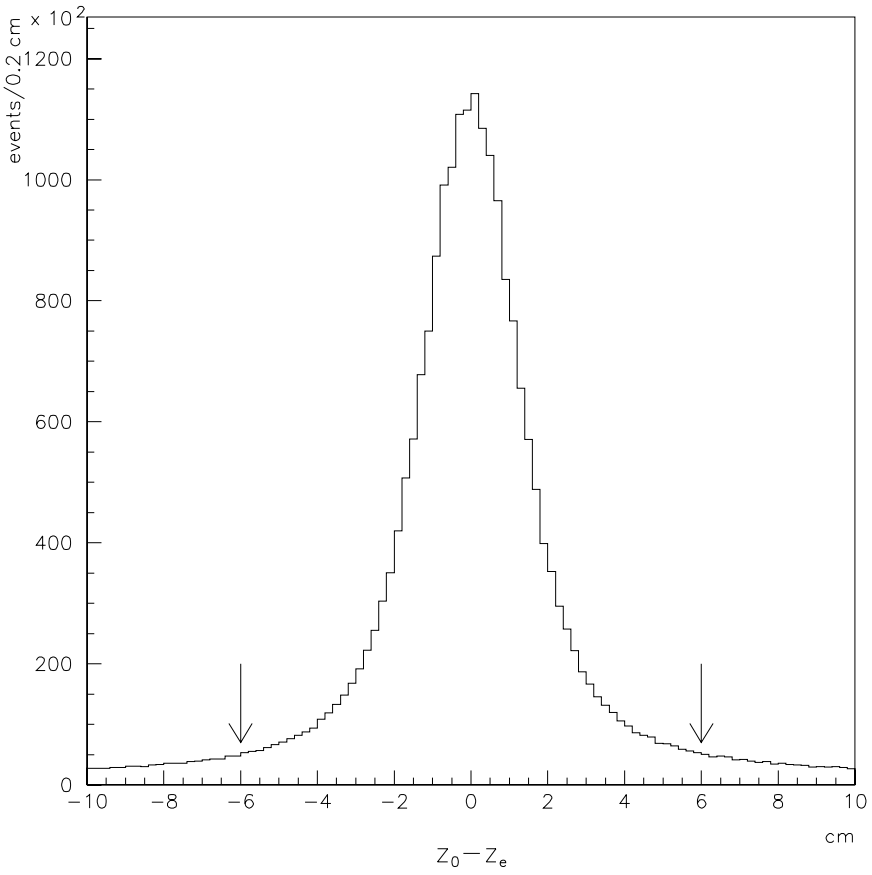

Figure 4.1: $z_0 - z_e$ distribution for tracks in electron data. The arrows indicate the $|z_0 - z_e| < 6$ cm window used in this analysis.

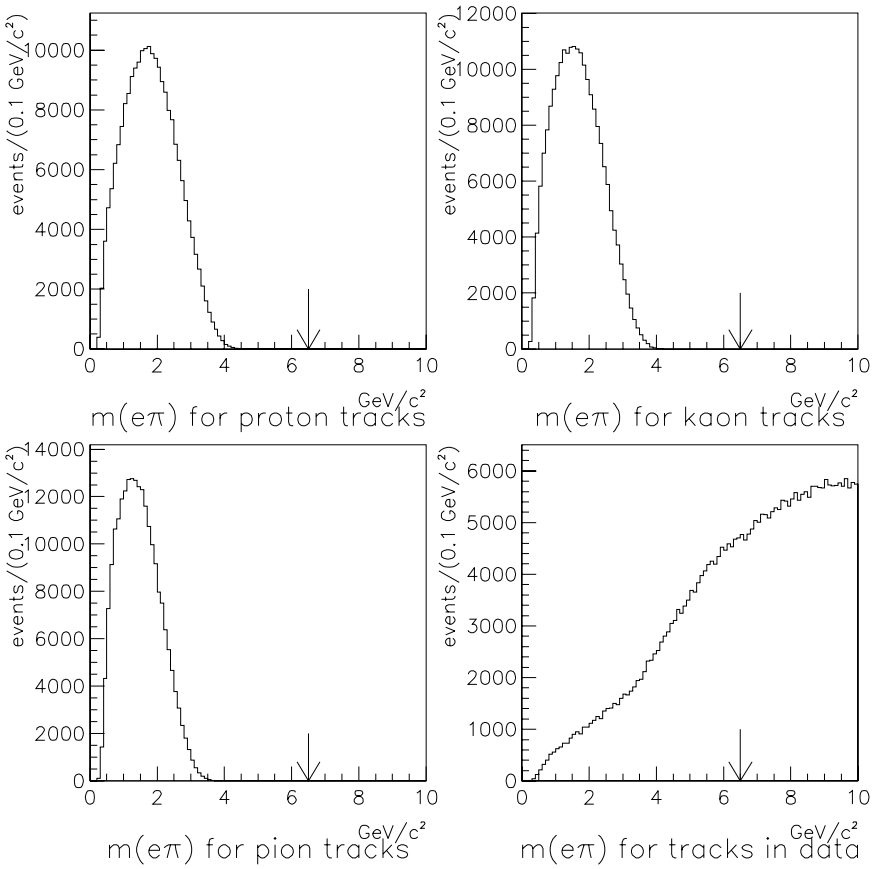

Figure 4.2: Monte Carlo generator-level mass distributions for the Λ_c daughters, when the Λ_c originates in Λ_b semileptonic decay. The hadronic track has been assigned the π^+ mass. All three tracks fall below the 6.5 GeV/c^2 cut which eliminates non-b tracks. The lower right plot shows the same distribution in data.

where the total charge is ± 1. The least-squares fit must have a fit $\chi^2 < 6.5$, corresponding to a fit probability exceeding 1%. The χ^2 distribution from simulated Λ_c decays is shown in Figure 4.3.

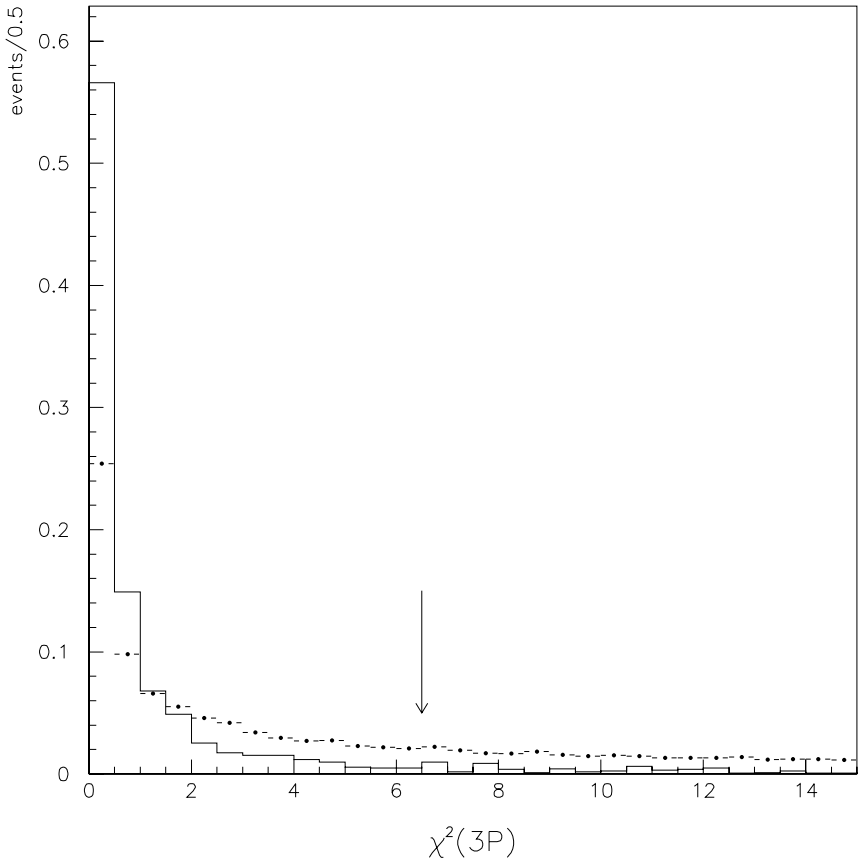

Figure 4.3: Simulated vertex χ^2's. The solid histogram is of the simulated signal, and the points from data sidebands, both normalized to unit area.

The transverse event topology is shown in Figures 4.4 and 4.5. The beam position and slope is measured for each run by the tracking detectors; the primary

vertex is taken to be the beam location at the z_0 of the electron track. All topological cuts are made with respect to this primary vertex. To make sure that the three-prong vertex is reasonably well measured, we require that the uncertainty on its transverse flight distance, $\sigma_{L_{xy}^{3P}}$, is less than 400 μm. Figure 4.6 shows that this cut keeps most of the signal.

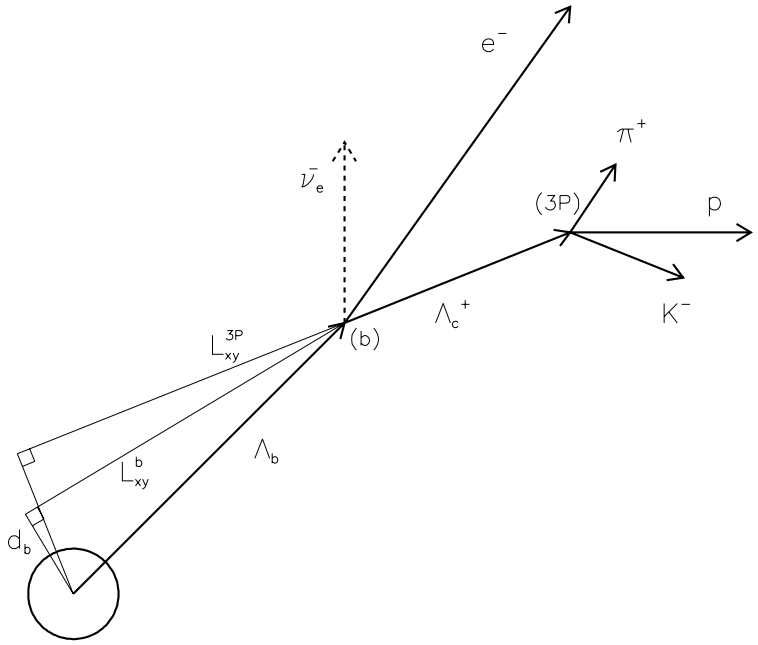

Figure 4.4: Transverse event topology, showing possible topological cut quantities (d_b, L_{xy}^b, and L_{xy}^{3P}) for vertex selection.

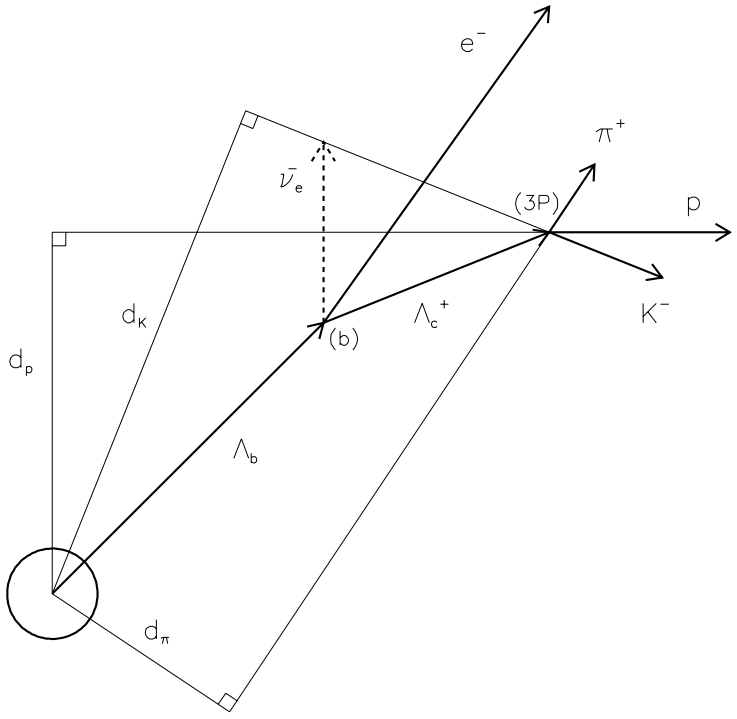

Figure 4.5: Transverse event topology, showing possible topological cut quantities (d_p, d_K, and d_π) for track selection.

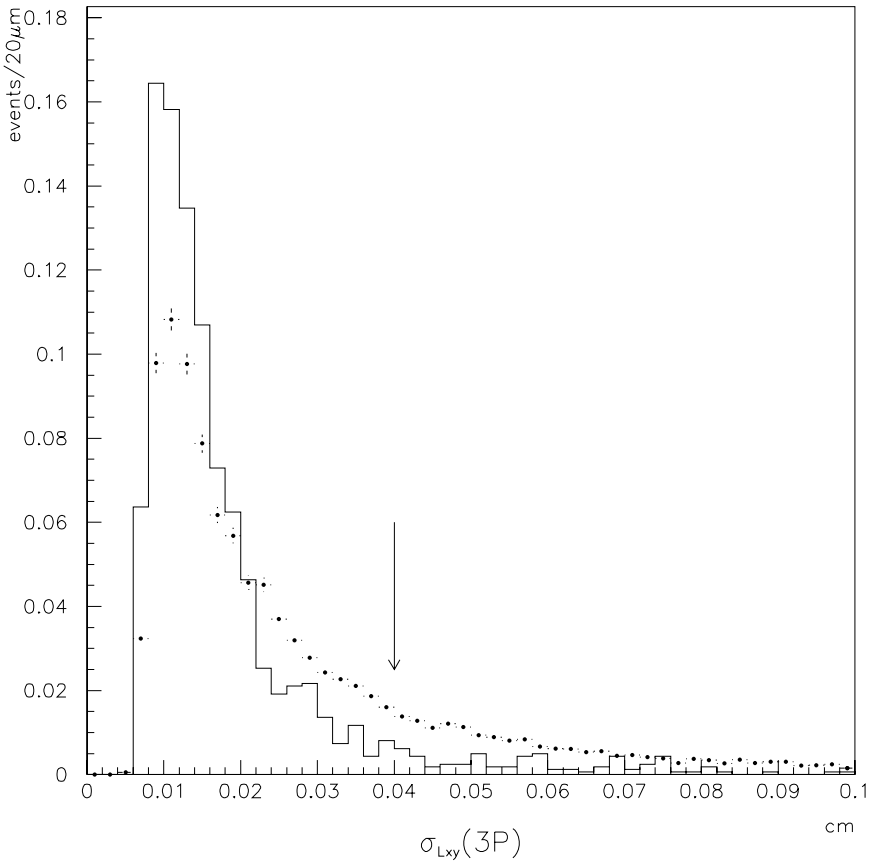

Figure 4.6: Simulated transverse flight distance uncertainties. The solid histogram is of the simulated signal, and the points from data sidebands.

We assign the masses of the three tracks as follows: one track's charge will be different from that of the other two; this track we assign the K^+ mass. The same-sign tracks are alternately assigned the proton and pion masses. This ambiguity presents the possibility of the same track combination appearing twice in the mass distribution. This issue is discussed in Section 5.4.2.

If the Λ_c candidate mass falls between 2.1 and 2.5 GeV/c^2, we extrapolate the Λ_c backwards, opposite its flight direction, and intersect it with the electron track. The $epK\pi$ mass is then required to fall between 3.5 and 6 GeV/c^2, to make sure it is consistent with Λ_b decay. As will be seen later, the lower bound distinguishes Λ_b decay from that of B mesons. The upper bound eliminates a significant amount of background, much of which is higher in mass than the signal, as shown in Figure 4.7.

Since most tracks are prompt, and therefore vertex very near the primary vertex with other prompt tracks, we require that the transverse flight distance, L_{xy}^{3P}, exceed 500 μm. This cut significantly reduces the combinatoric background.

The cuts described in this section are listed in Table 4.1. In the next section, we will use Monte Carlo and data to optimize a set of cuts to find the Λ_c signal in the electron dataset.

4.3 Cut Optimization

In a counting experiment, the statistical error on a signal of size S is $\sqrt{S+B}$, where B is the background. Minimal statistical error is achieved, therefore, when $S^2/(S+B)$ is maximized. Where the signal is small compared to the background, however, S^2/B is a reasonable approximation. It has the further advantage of its minimum being insensitive to the relative normalizations of the signal and

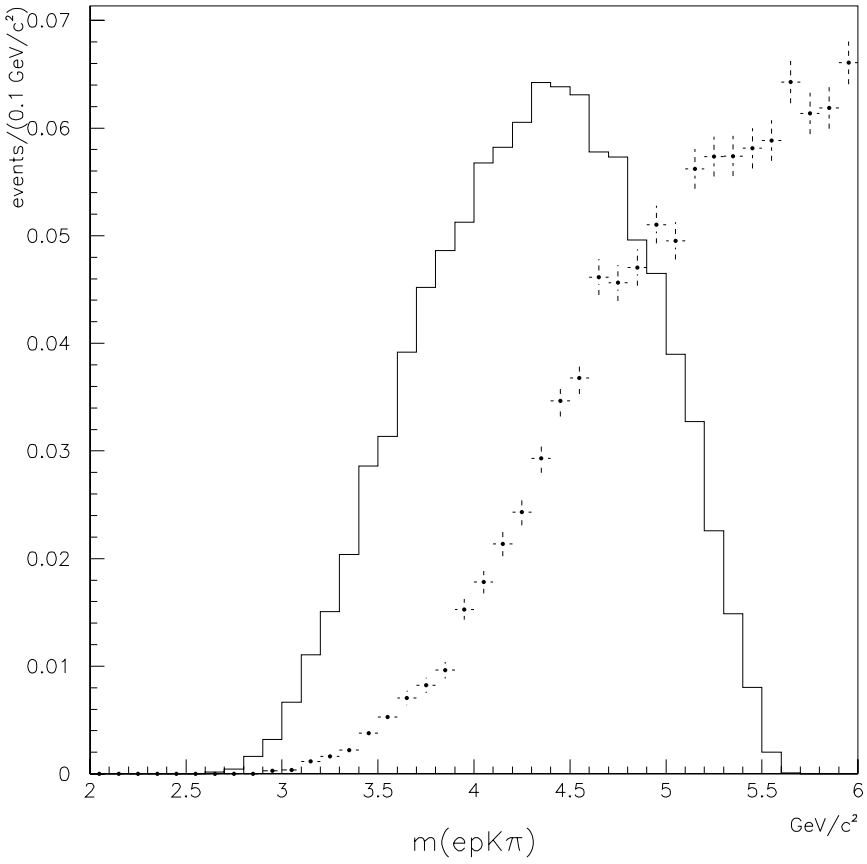

Figure 4.7: Generator-level $epK\pi$ mass spectrum for Λ_b decay (solid), and from the data sidebands (points). This analysis uses $epK\pi$ combinations between 3.5 and 6 GeV/c^2.

SVX quality	≥ 2 hits
	$\chi^2 < 6$ per hit
	4 hits expected
CTC quality	exit radius > 130 cm
daughter tracks	$p_T > 450$ MeV/c
	$\lvert z_0 - z_e \rvert < 6$ cm
	$m(e\text{“}\pi'') < 6.5$ GeV/c^2
Λ_c candidate	$P(\chi^2) > 1\%$
	$L_{xy}^{3P} > 500$ μm
	$\sigma_{L_{xy}^{3P}} < 400$ μm
Λ_b candidate	$m(epK\pi) \in (3.5, 6)$ GeV/c^2

Table 4.1: Cuts applied to the monte carlo signal and data sidebands before optimization.

background models. If one has a collection of events which reflect a reasonable model of the signal and of the background, he can obtain an estimate of S^2/B for a given set of cuts simply by counting the modeled signal and background events which survive. The cuts can then be varied to maximize S^2/B.

We use Monte Carlo to model the signal behavior. For the background, we can use data from the Λ_c mass sidebands. We assume for this purpose that the distributions which characterize the background underneath the signal vary smoothly from the low to high sidebands. Since we use Monte Carlo to model the signal, this method will not artificially enhance a statistical fluctuation.

It should be noted that for the rate calculation, the actual cuts used are irrelevent as long as the efficiencies are measurable. The effect of the optimization is to reduce the statistical uncertainty in the size of the signal. The method described above is useful to find a reasonable signal in an unbiassed manner, and depends only upon a reasonable signal model. This optimization was done with an older Monte Carlo model. However, this fact did not necessitate an update.

The Monte Carlo model used for the cut optimization was as follows: the b quarks were generated and fragmented using PYTHIA version 5.6, which incorporates the Lund symmetric fragmentation model as implemented by JETSET version 7.2. Events containing Λ_b's were selected, and the Λ_b's decayed using the QQ decay package, version 9.0, which in this case used a quark-level $V-A$ model for the exclusive decay $\Lambda_b \to \Lambda_c^+ e^- \overline{\nu}_e$. The detector is simulated with QFL, which reflects the detector geometry and models the behavior of the various detector components with parameterized distributions which have been tuned to match data. A 9 GeV E_T cut suffices for the Level 2 trigger at this point.

The updated Monte Carlo is described in detail in Section 4.3.3, and amounts to a complete overhaul: an integrated spectrum is used to generate the b quark

p_T's, and the color-coherent Lund model is replaced by the independent Peterson model. The Λ_b decay is simulated with form factors described in Section 1.2.2.

4.3.1 Cut Selection

The decay $\Lambda_c \to pK\pi$ offers little in the way of helpful decay characteristics. For instance, the two-body components of the $pK\pi$ final state,

$$\begin{aligned}
\Lambda_c^+ &\to p\overline{K}^{*0}, \\
&\quad \overline{K}^{*0} \to K^-\pi^+ \\
\Lambda_c^+ &\to \Lambda(1520)\pi^+, \\
&\quad \Lambda(1520) \to pK^- \\
\Lambda_c^+ &\to \Delta^{++}K^-, \\
&\quad \Delta^{++} \to p\pi^+
\end{aligned}$$

do not help much, since all the resonances are wide. Furthermore, the resonant components of the decay make up perhaps half the total $pK\pi$ decay width.

We are therefore restricted to using straightforward cuts such as those on momenta, flight distances, and impact parameters. We can also use a cone cut to take advantage of the boost of the decay. However, this cut is redundant with mass cuts. All momentum cuts, whether for parent or daughter particles, are also correlated. We have chosen to cut on the p_T's of the four observed daughter particles.

The cuts to be considered are therefore as follows:

- Λ_c daughter tracks
  - proton p_T

  - kaon p_T
  - pion p_T
  - d/σ_d, the impact parameter significance of the daughter tracks, to select tracks inconsistent with the primary vertex

- three-prong vertex, or Λ_c candidate
  - L_{xy}^{3P}, the apparent flight distance of the Λ_c candidate, in the $\vec{p}_T^{3P}$ direction, relative to the primary vertex

- $epK\pi$ vertex, or partially reconstructed Λ_b candidate
  - L_{xy}^{b}, the apparent transverse flight distance of the $e\Lambda_c$ combination, in the $\vec{p}_T^{3P} + \vec{p}_T^{e}$ direction, relative to the primary vertex
  - d_b, the impact parameter of the partially reconstructed Λ_b with respect to the primary vertex

An upper bound of 1 cm is applied to all flight distance quantities, since these combinations are likely to be random combinations. Straight cuts on flight distance quantities and d_b are preferred over significance cuts because the latter can include very badly measured vertices. On the other hand, d/σ_d is preferred to select tracks because badly measured tracks tend to have large errors and are thus removed from consideration.

4.3.2 Results

We do not vary all seven cut thresholds simultaneously. Instead, we vary them in order of importance: these are the thresholds with the most strongly peaked S^2/B curves. The first cuts we vary are therefore those on the Λ_c daughter p_T's.

daughter tracks	$p_T^p > 2.0$ GeV/c
	$p_T^K > 1.0$ GeV/c
	$p_T^\pi > 0.45$ GeV/c
	$\lvert d_0/\sigma_{d_0}\rvert > 1.5$
Λ_c candidate	$L_{xy}^{3P} > 500$ μm
Λ_b candidate	$L_{xy}^b > -300$ μm
	$\lvert d_b\rvert < 250$ μm
other cuts	D^{*+} exclusion
	proton dE/dx

Table 4.2: Reconstruction cuts after optimization.

The signal and background distributions are shown in Figure 4.8, and the S^2/B curves are shown in Figure 4.9. The thresholds are set at $p_T^p > 2$ GeV/c and $p_T^K > 1$ GeV/c. The pion p_T cut is left at 450 MeV/c.

After the daughter p_T thresholds are applied, the S^2/B profiles broaden. The $|d_0/\sigma_{d_0}|$, $|d_b|$, and L_{xy}^b cuts are then optimized in that order, and the results shown in Table 4.2. The L_{xy}^{3P} threshold remains at 500 μm, indicating that this threshold could be placed lower. However, the cut was applied to reduce the combinatoric background to a manageable level.

As will be discussed in Section 5.4.2, a D^* exclusion cut must be applied to eliminate D^* reflections: the proton candidate track is assigned a pion mass and paired with the kaon. If the mass falls between 1.815 and 1.915 GeV/c^2, that is, consistent with a D^0 mass, then the mass difference is computed between the D^0 combination and the $D^0\pi$ combination. If this mass difference is less than 0.15 GeV/c^2, the three-prong vertex is rejected.

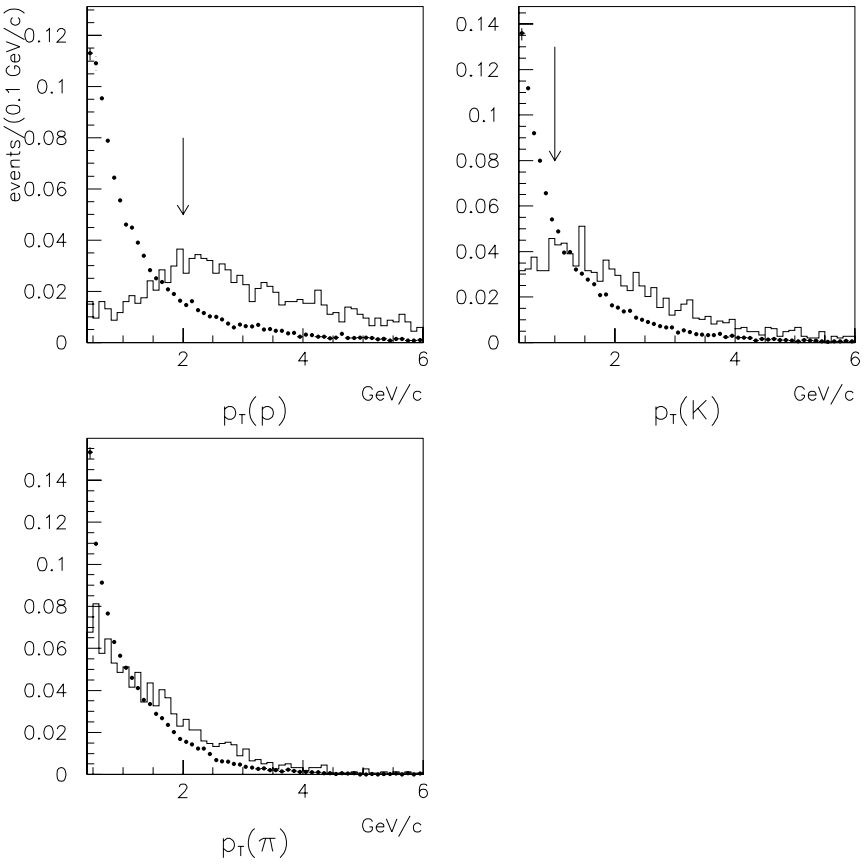

Figure 4.8: Simulated Λ_c daughter track p_T spectra with only pre-optimization cuts applied (solid). The points are from data sidebands. The pion cut is left at the 450 MeV/c minimum.

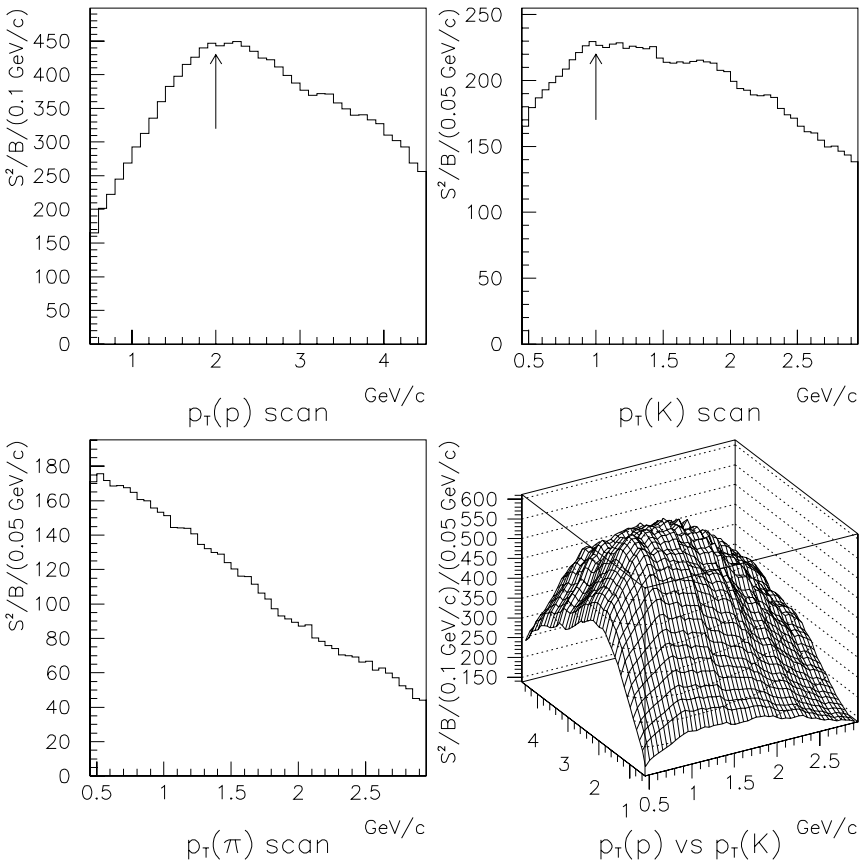

Figure 4.9: S^2/B profiles for Λ_c daughter track p_T cuts. The pion p_T cut is set at 450 MeV/c, the minimum threshold. The lower right plot shows the result of simultaneously varying the proton and kaon p_T cuts. There is no difference between varying the two cuts independently and simultaneously.

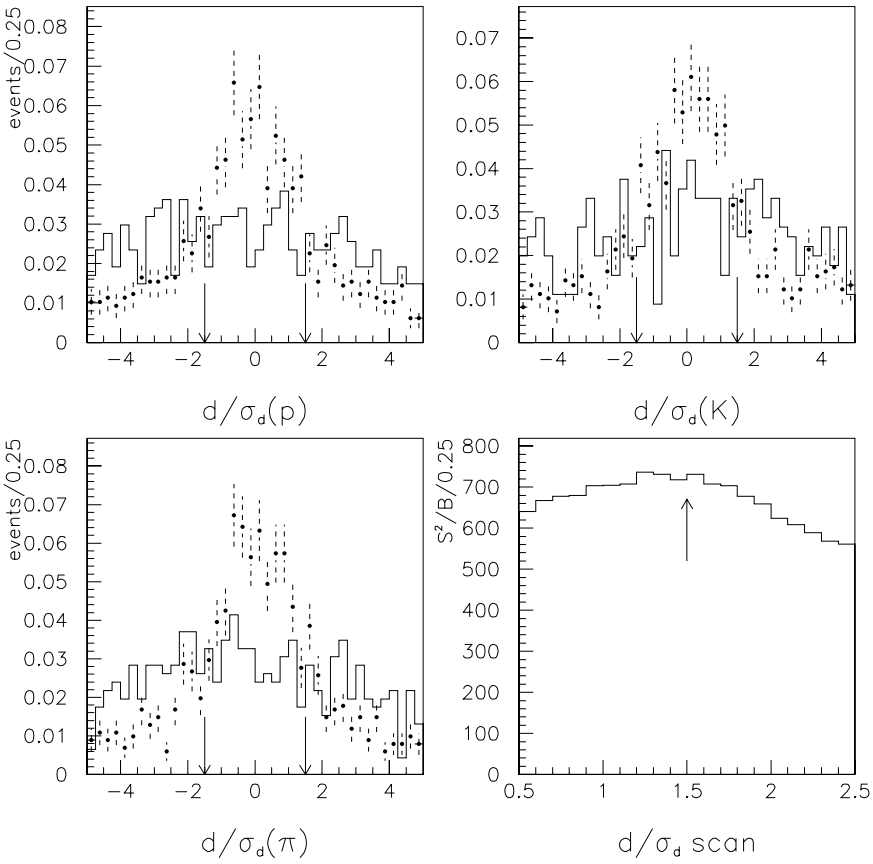

Figure 4.10: d_0/σ_{d_0} distributions from Monte Carlo (solid) and data sidebands (points). The lower right plot shows the S^2/B profile as all three thresholds are varied simultaneously.

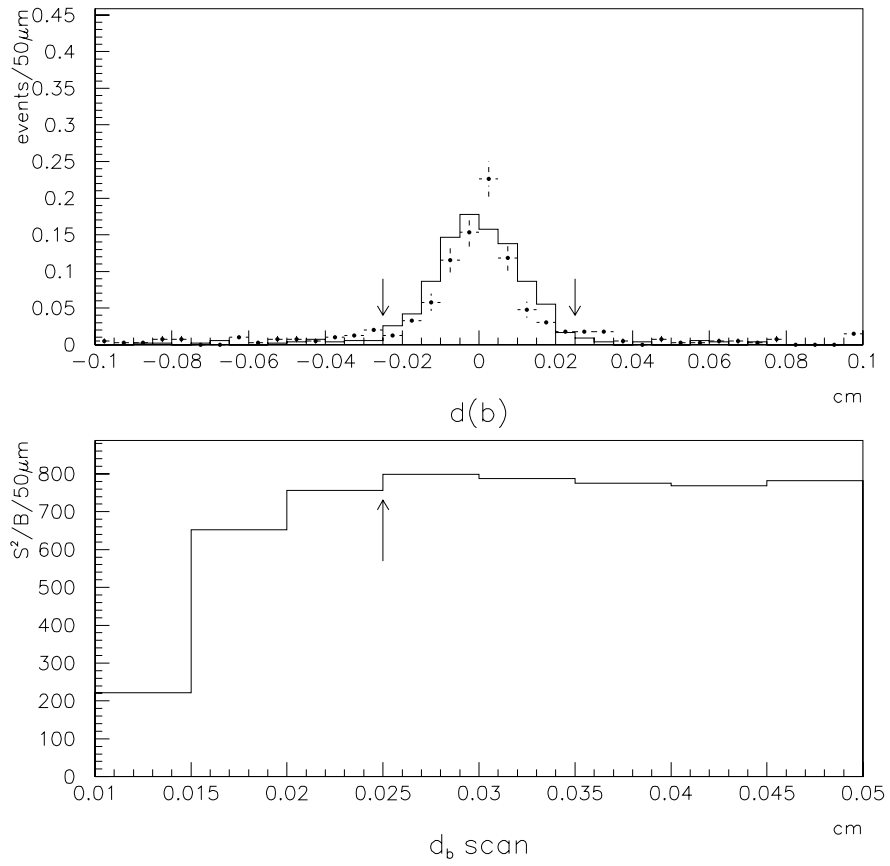

Figure 4.11: Top: d_b distributions from Monte Carlo (solid) and data sidebands (points). Bottom: S^2/B profile. S^2/B decreases slowly in the positive direction.

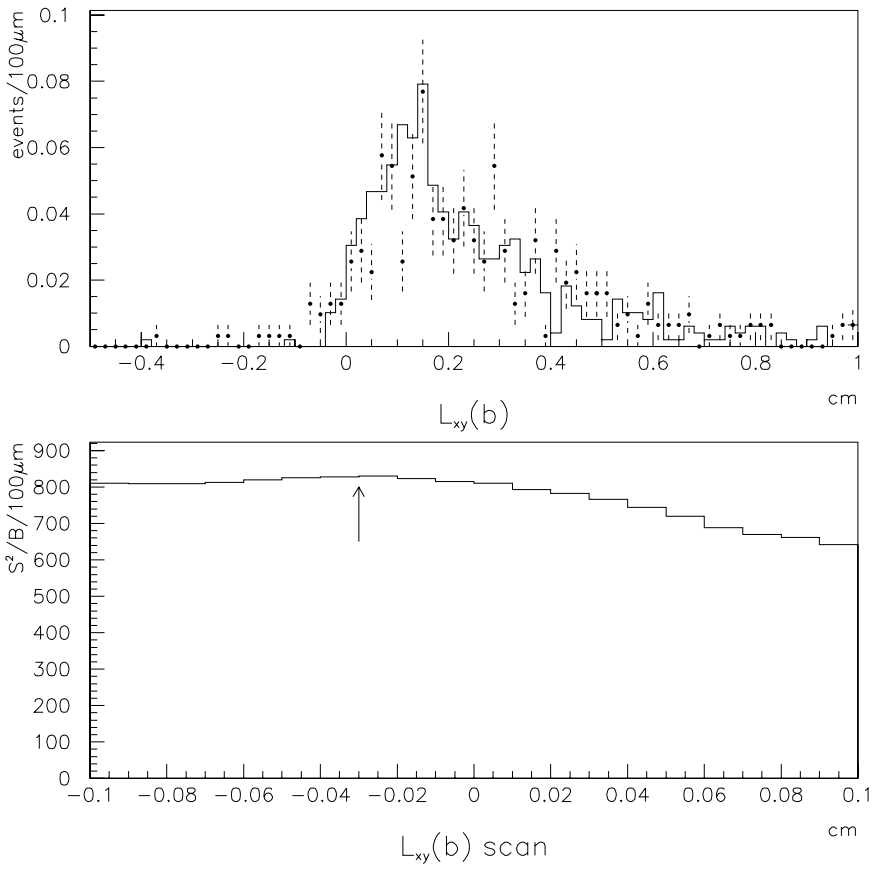

Figure 4.12: Top: L_{xy}^{b} distributions from Monte Carlo (solid) and data sidebands (points). Bottom: S^2/B profile. S^2/B decreases slowly in the negative direction.

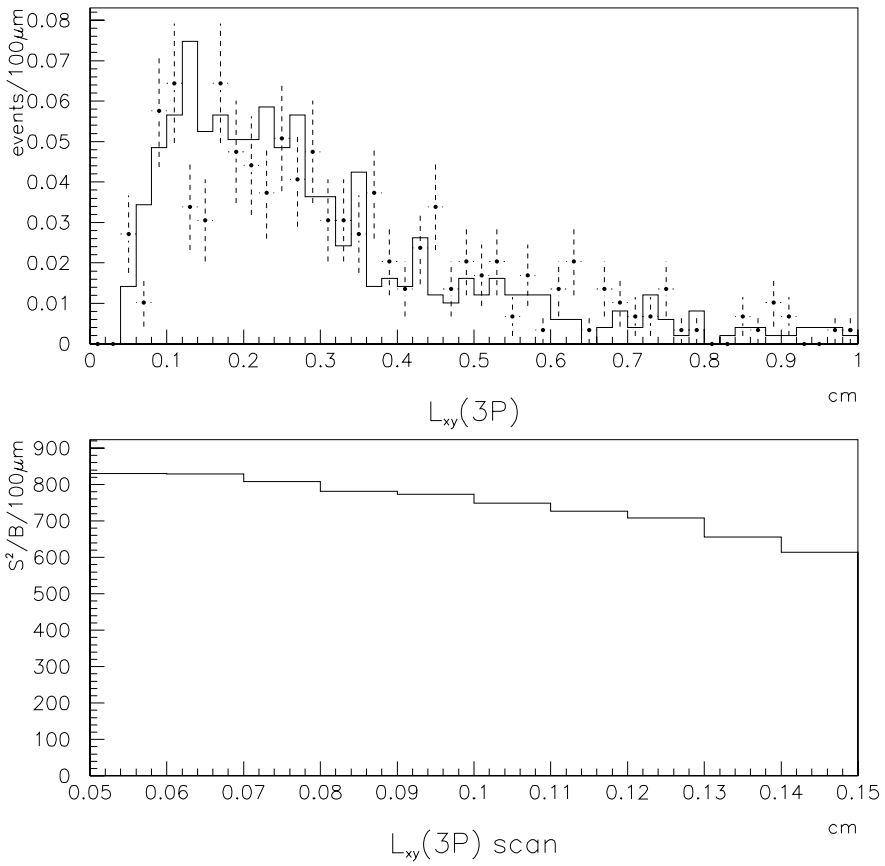

Figure 4.13: Top: L_{xy}^{3P} distributions from Monte Carlo (solid) and data sidebands (points). Bottom: S^2/B profile. The $L_{xy}^{3P} > 500$ μm cut is the minimal cut, having been applied to reduce combinatorial background before optimization.

Finally, the dE/dx measurements from the CTC are used to make sure that the energy loss along the proton candidate track is consistent, within about 2σ, with that of a real proton.

The efficiency of these cuts will be discussed in Section 6.2.

4.3.3 Monte Carlo

As mentioned previously, the cut optimization is somewhat historical, performed with a Monte Carlo package later superseded. For the purpose of efficiency and acceptance calculation, as well as for comparing Monte Carlo and data distributions, we use another package. In this updated simulation, the b quarks are generated according to the next-to-leading-order calculation of Nason, Dawson, and Ellis with mass scale $\mu = \mu_0$ and b quark mass 4.75 GeV/c^2. [4] The b quark is then hadronized into a Λ_b using the independent fragmentation model of Peterson with $\epsilon = 0.006$. [6] For the exclusive semileptonic decay distribution we use Scora's quark potential model calculation. [14] The detector simulation is the same as before. The Level 2 trigger is simulated by weighting each event in any histogram by the trigger parameterization.

Besides the model differences, the updated Monte Carlo generates only the Λ_b. Underlying event and fragmentation particles are not simulated. Their effect on the simulation will be discussed in Section 6.2.1.

The updated Monte Carlo has the advantages not only of using distributions tuned to previous experimental data, as well as a more sophisticated decay model, but also of speed. A sample of two million Λ_b's was generated with the updated Monte Carlo. The mass distribution for the right-sign events is shown in Figure 4.14. The width is 7.9 ± 0.3 GeV/c^2.

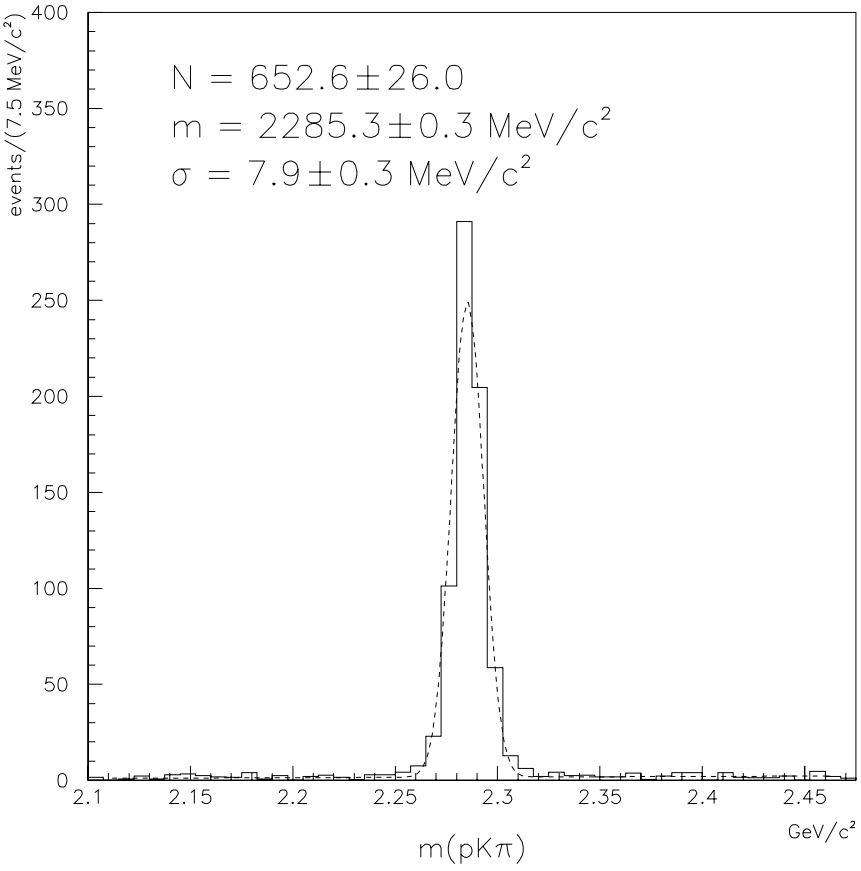

Figure 4.14: Monte Carlo right-sign $e\Lambda_c$ signal.

4.4 Data

Applying our event selection to the data, we first reconstruct D^+'s as a check. The resulting signal is shown in Figure 4.15. We reconstruct 74.2±10.5 events at a mass of 1869.6±1.3 MeV/c^2. The 1994 world average D^+ mass is 1869.4±0.4 MeV/c^2. [1] The width, at 7.9 ± 1.0 MeV/c^2, is consistent with the Monte Carlo expectation.

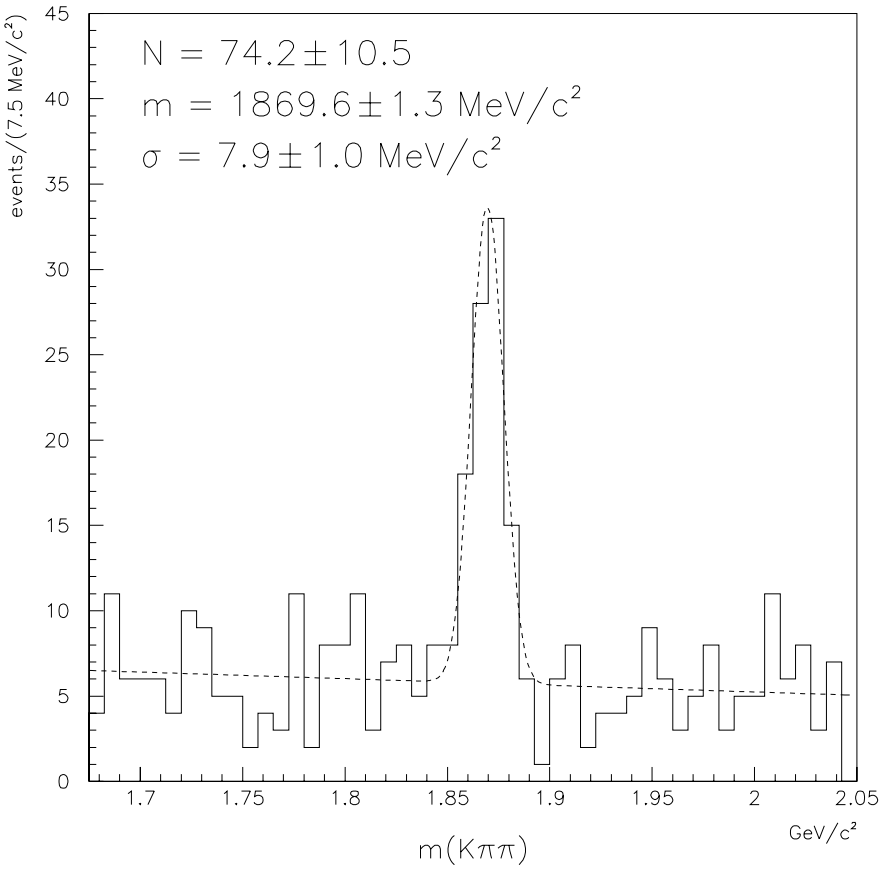

Figure 4.15: $K\pi\pi$ mass distribution of right-sign $eK\pi\pi$ combinations in data.

Figure 4.16 shows the right-sign combinations in data after applying the above

cuts to the fitted $pK\pi$ vertices. There is an obvious signal at the Λ_c mass. Fitting the signal with a gaussian over a linear background shows that the peak consists of 35.7 ± 9.4 signal events at a mass of 2288.3 ± 2.5 MeV/c^2. The 1994 world average mass is 2285.1 ± 0.6 MeV/c^2. The width is 8.0 ± 1.9 MeV/c^2, again consistent with the Monte Carlo expectation.

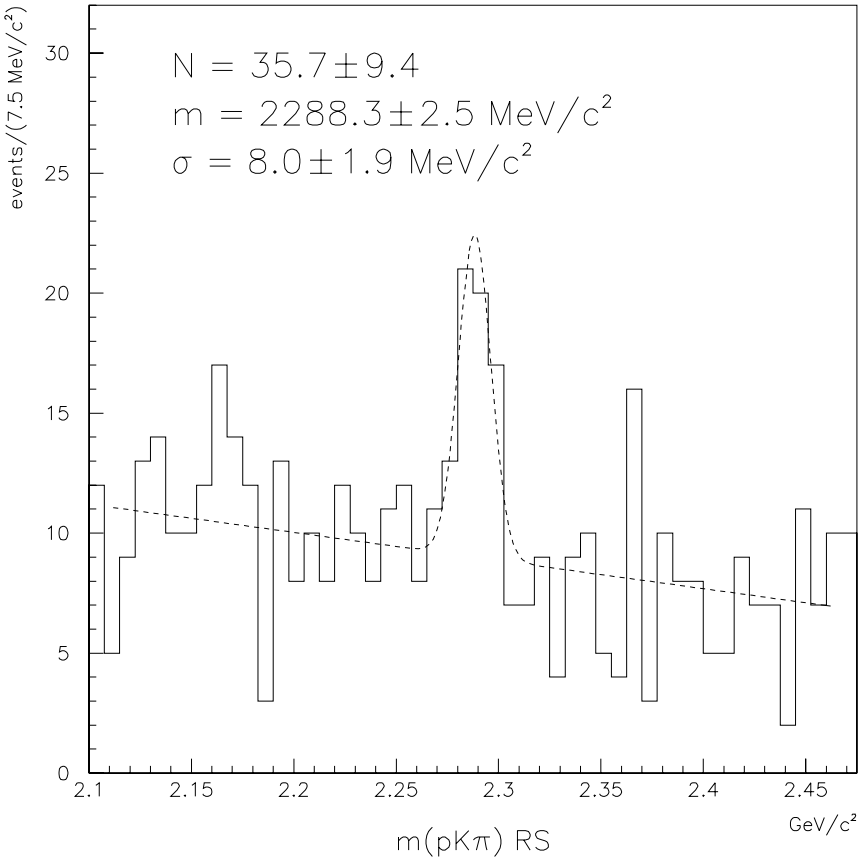

Figure 4.16: $pK\pi$ mass distribution of right-sign $epK\pi$ combinations in data.

The wrong-sign combinations shown in Figure 4.17 show no discernible Λ_c

signal. If the mass and width are fixed to the values they hold in Figure 4.16, the yield is 5.2 ± 5.1 events, due to the one high bin. Since it lies near to a low bin, we expect this is due to statistical fluctuations in the background.

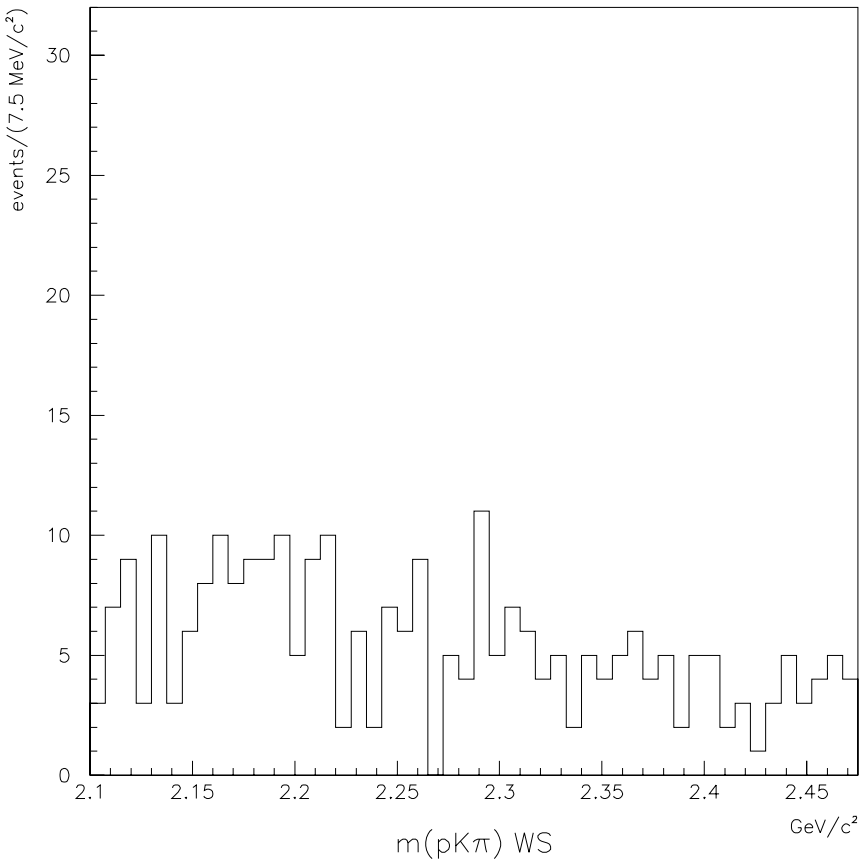

Figure 4.17: $pK\pi$ mass distribution of wrong-sign $epK\pi$ combinations in data.

We can compare data and Monte Carlo distributions for kinematic distributions. For this purpose, we select the mass region between 2.26 and 2.31 GeV/c^2 as the signal region and compute the background contribution to this region by

linear extrapolation from the sidebands. We then subtract the distribution from the sidebands, normalized to the computed background contribution. The results are shown in Figures 4.18 and 4.19. The signal being small, little more can be said than that the signal in data behaves in a manner consistent with Monte Carlo expectations for Λ_b semileptonic decay.

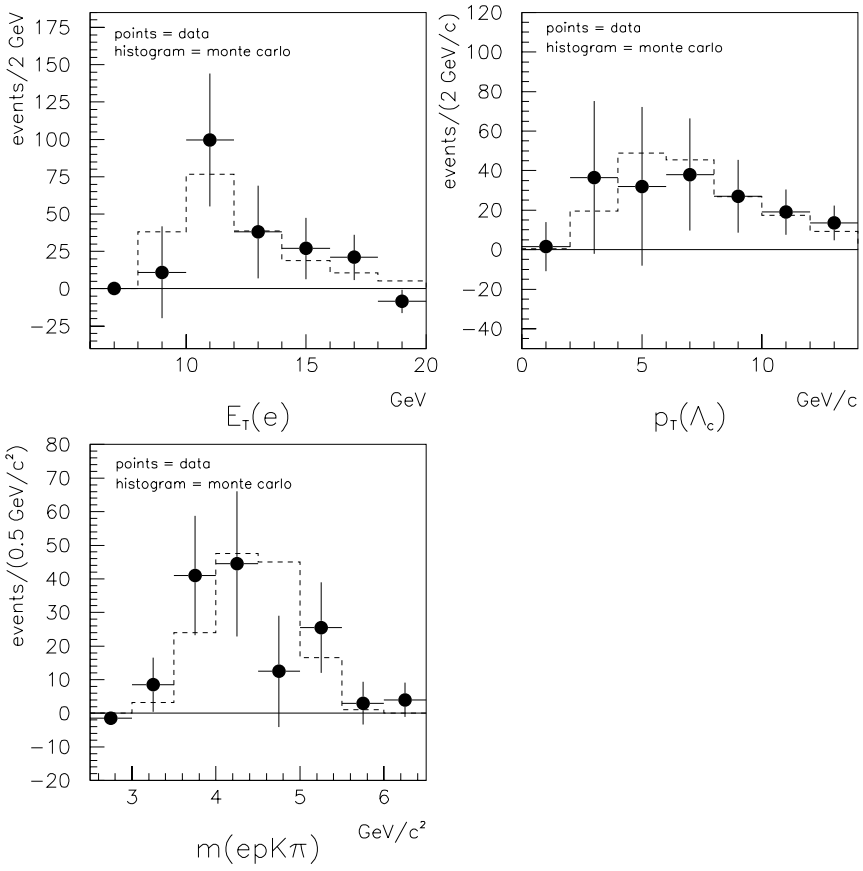

Figure 4.18: Comparison between sideband-subtracted data (points) and Monte Carlo (histogram) distributions.

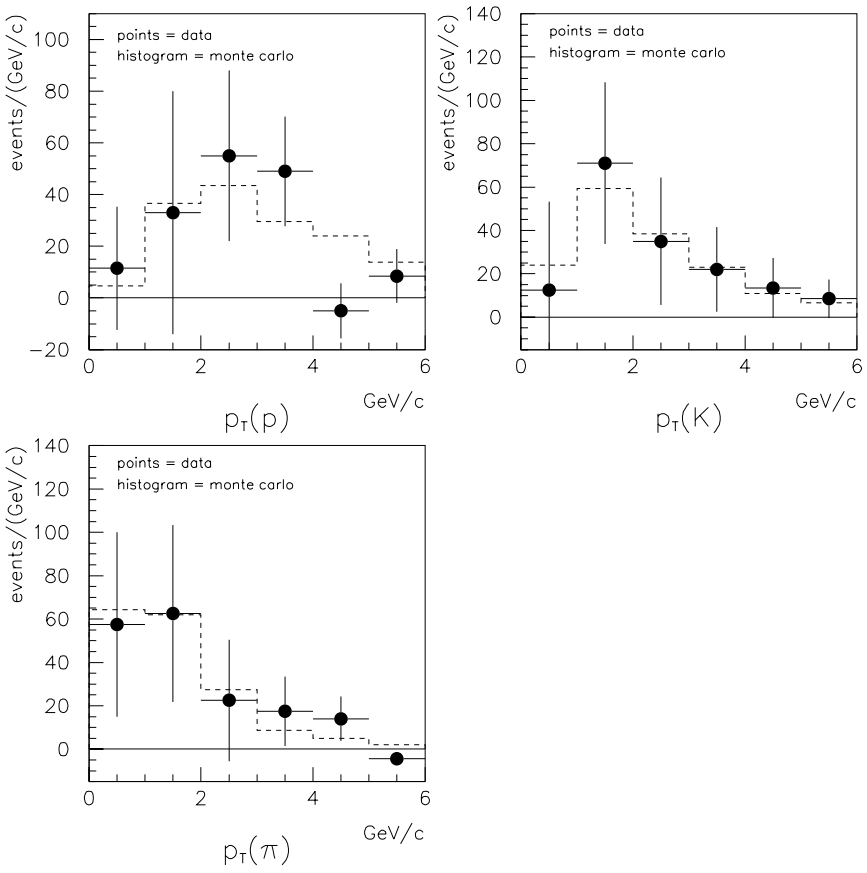

Figure 4.19: Comparison between sideband-subtracted data (points) and Monte Carlo (histogram) distributions for Λ_c daughter tracks.

Chapter 5

Backgrounds

A right-sign Λ_c signal does not by itself prove that Λ_b's have been produced. It merely shows that there is a sign correlation. To show that the sign correlation is a Λ_b signal, one must enumerate other possible sources of sign-correlated $\Lambda_c e$ pairs and either show that they do not contribute to the signal, or that they contribute negligibly. The first backgrounds we will consider will consist of real electrons and real Λ_c's. These include b hadron decays, $\overline{b}b$ and $\overline{c}c$ pairs, and real Λ_c's produced in conjunction with conversion electrons. Second, we will consider those backgrounds where a real electron is associated with a fake Λ_c candidate. These include reflections from other charm particles as well as from Λ_c itself, and the combinatoric background for $pK\pi$ mass combinations. Finally, hadronic fake "electrons" will be considered.

5.1 b Hadron Decays

Possible b hadron decays with electrons and Λ_c's in their final state are as follows:

- $\Lambda_b \to \Lambda_c^+ D_s^- X$,
  $D_s^- \to e^- X'$

- $B \to \Lambda_c^+ D_s^- X$,
  $D_s^- \to e^- X'$

- $B \to \Lambda_c^+ e^- \overline{\nu}_e X$

It should be noted that there are no direct experimental observations of these decay modes. CLEO has reported upper limits on the last process, [23] and $D_s^- \to e^- X'$ is only known as an upper limit. [24] However, even with small branching fractions and smaller efficiencies due to antibaryon production, the B meson decays must be examined, since B meson production is expected to an order of magnitude greater than that of b baryons.

5.1.1 $\Lambda_b \to \Lambda_c^+ D_s^- X, D_s^- \to e^- X'$

This first mode represents a hadronic decay of Λ_b. The simplest diagram for this process, excluding additional hadrons, is illustrated in Figure 5.1. Physically, its rate is suppressed by the D_s semielectronic branching fraction, for which there is a 90% C.L. limit of 20%. We have simulated this Λ_b decay mode assuming phase space decay distributions and no additional hadron production. The electron, as is typical with electrons from charm decay, is softer than those from bottom decay. The $epK\pi$ mass distribution is also softer, as shown in Figure 5.2. The resulting efficiency is 0.034 of the standard value. The branching fraction may be reasonably expected to be within a factor of two of that of the corresponding decay $\overline{B} \to D_s^{(*)} D^{(*)}$, which is $(5.0 \pm 0.9)\%$. [1] We therefore deduce that this decay mode contributes less than one half an event to the signal.

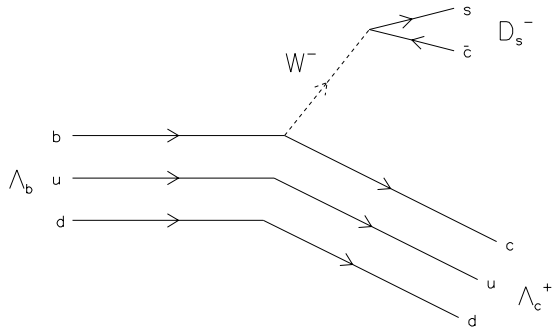

Figure 5.1: Lowest-order diagram of the process $\Lambda_b \to \Lambda_c^+ D_s^-$, a background to the Λ_b semileptonic decay signal when the D_s^- decays semileptonically.

5.1.2 $B \to \Lambda_c^+ D_s^- \overline{N} X, D_s^- \to e^- X'$

This decay mode is the analogue of the above, the parent particle being a meson instead of a baryon. This process is shown in Figure 5.3. The antibaryon must be produced to conserve baryon number. This effect softens kinematic distributions for the other daughter particles. It has been simulated with phase space distributions and no additional hadrons, and we note from the resulting distribution shown in Figure 5.4 that all the events fall below the 3.5 GeV/c^2 $epK\pi$ mass cut. They cannot contribute to the signal.

5.1.3 $B \to \Lambda_c^+ e^- \overline{N} \overline{\nu}_e X$

This is the semileptonic decay of a B meson with a Λ_c in its final state, as shown in Figure 5.5. CLEO has measured the branching fraction of B mesons produced at $\Upsilon(4S)$ to any final state including a charm baryon: [23]

$$\mathrm{Br}(\overline{B}_{u,d} \to \mathit{charm\ baryon} X) = 0.064 \pm 0.008 \pm 0.008. \qquad (5.1)$$

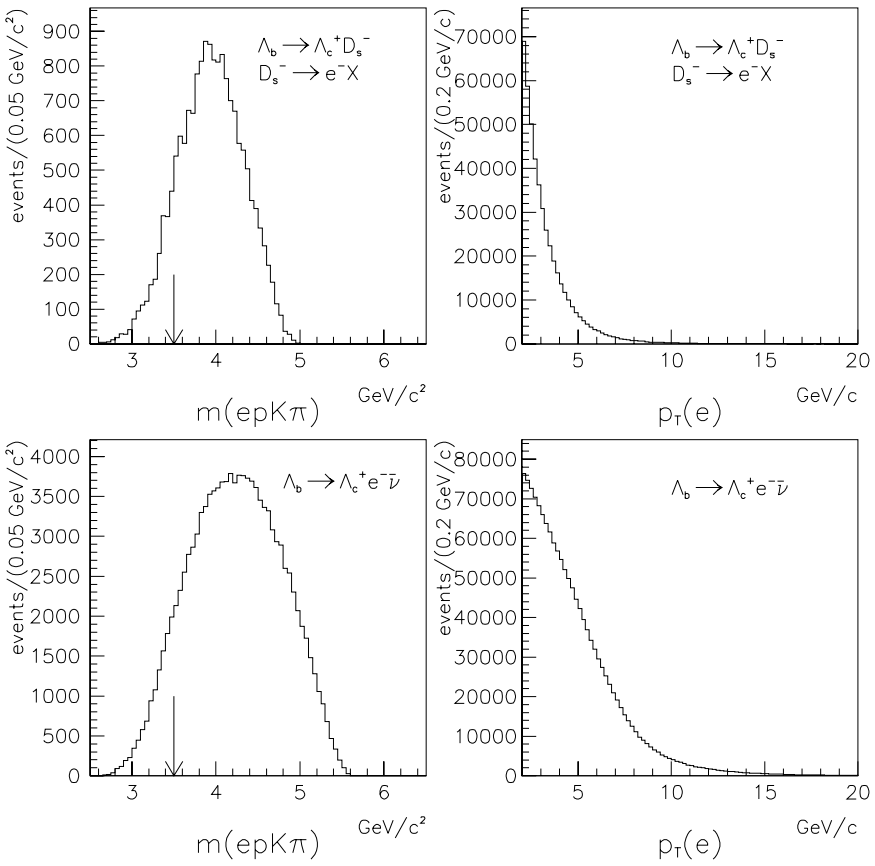

Figure 5.2: Top: Monte Carlo $epK\pi$ invariant mass (left) and electron p_T (right) distributions for the process $\Lambda_b \to \Lambda_c^+ D_s^-$ followed by $D_s^- \to e^- X$, to be compared with bottom plots for $\Lambda_b \to \Lambda_c^+ e^- \overline{\nu}_e$.

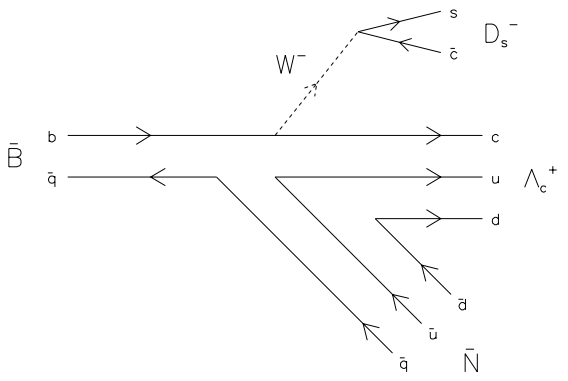

Figure 5.3: Lowest-order diagram of the background process $\overline{B} \to \Lambda_c^+ D_s^- \overline{N}$, where $\overline{N}$ is the appropriate antibaryon.

An upper limit has also been established for the semileptonic decay, relative to the branching fraction to any final state including a Λ_c: [25]

$$\frac{\mathrm{Br}(\overline{B}_{u,d} \to \Lambda_c^+ e^- \overline{\nu}_e \overline{N} X)}{\mathrm{Br}(\overline{B}_{u,d} \to \Lambda_c^+ X')} < 5.7\%(90\% C.L.). \tag{5.2}$$

We combine these two measurements, assuming that Λ_c saturates the first branching fraction, and taking the upper limit of the second as the branching fraction, to get

$$\mathrm{Br}(\overline{B}_{u,d} \to \Lambda_c^+ e^- \overline{\nu}_e \overline{N} X) = 0.36\% \tag{5.3}$$

It should be noted that if charm baryons are produced in $\overline{B}_{u,d}$ decay other than Λ_c, and those charm baryons do not decay through Λ_c, the above rate limit will be smaller.

As in the $\overline{B}_{u,d} \to \Lambda_c^+ D_s^- \overline{N} X$ case, the extra antibaryon softens the kinematic distributions, though in this case the effect is not as noticeable since the electron is from bottom rather than charm decay. The main difference is that the $m(epK\pi) > 3.5$ GeV/c^2 requirement eliminates about half the meson signal, but keeps most of

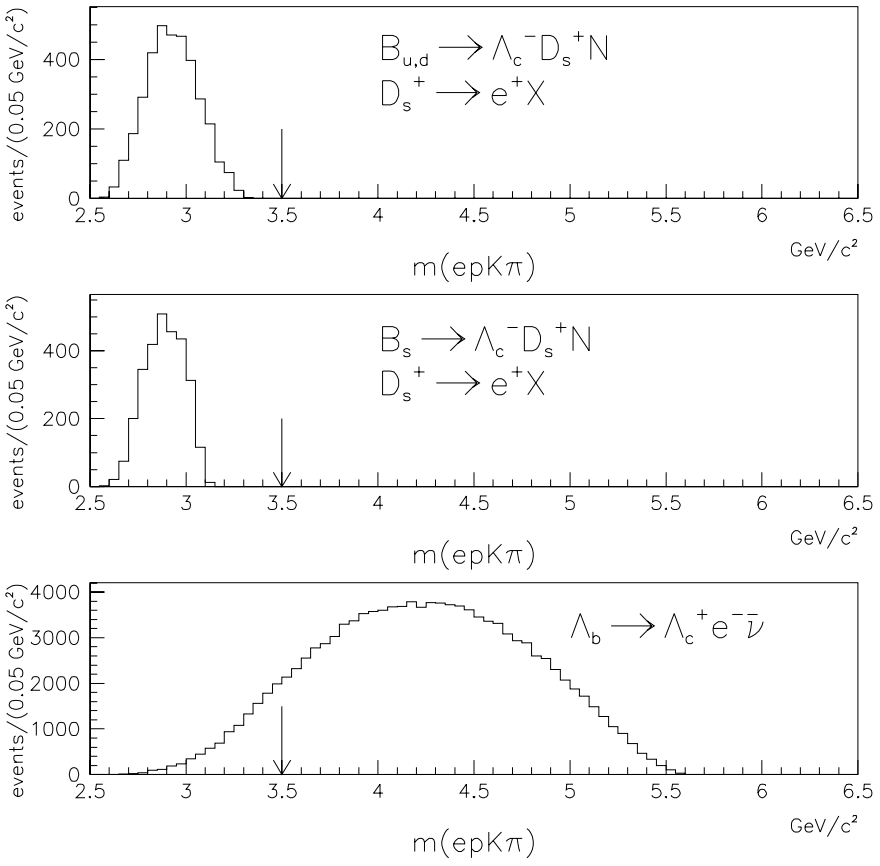

Figure 5.4: Simulated $epK\pi$ mass distributions for $B_{u,d} \to \Lambda_c^+ D_s^- \overline{N}$ followed by $D_s^- \to e^- X$ (top) and $B_s \to \Lambda_c^+ D_s^- \overline{N}$ (middle), to be compared with that for $\Lambda_b \to \Lambda_c^+ e^- \overline{\nu}_e$.

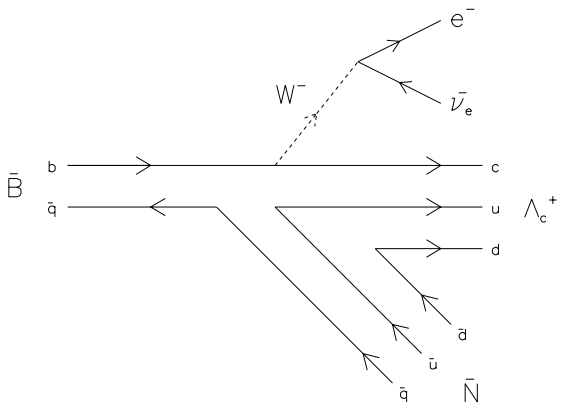

Figure 5.5: Lowest-order diagram of B meson semileptonic decay, with a Λ_c in the final state.

the Λ_b events. The efficiency for these baryonic B_u and B_d decays, without any additional decay products, is measured to be 7.4% of that of $\Lambda_b \to \Lambda_c^+ e^- \overline{\nu}_e$. If we assume that the production ratio of B_u and B_d to Λ_b is 0.375:0.10 each, and that the Λ_b semileptonic branching fraction is a conservatively low 5%—it is more likely to be about 9%, as indicated in Section 1.3—then this decay mode contributes at most 4% of the $e\Lambda_c$ signal, which in this case is 1.4 of an event.

There is no corresponding measurement for the decay mode $\overline{B}_s \to \Lambda_c^+ e^- \overline{\nu}_e \overline{N} X$, but since the strange quark is a spectator in the decay we assume for the purpose of this background study that the branching fraction is the same. In this case the efficiency is 0.8% of the Λ_b efficiency. If we assume that the production fraction of B_s to Λ_b is 0.15:0.10, then this decay mode contributes less than 0.3 events to the signal.

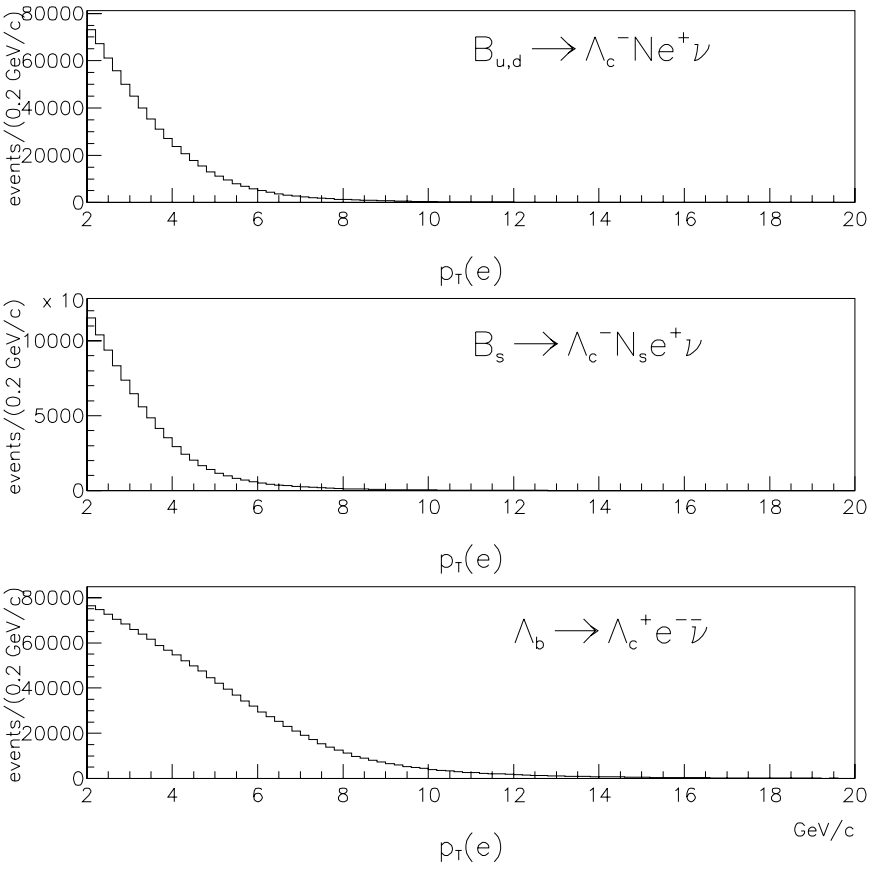

Figure 5.6: Electron p_T distributions for simulated semileptonic b hadron decays with a Λ_c daughter.

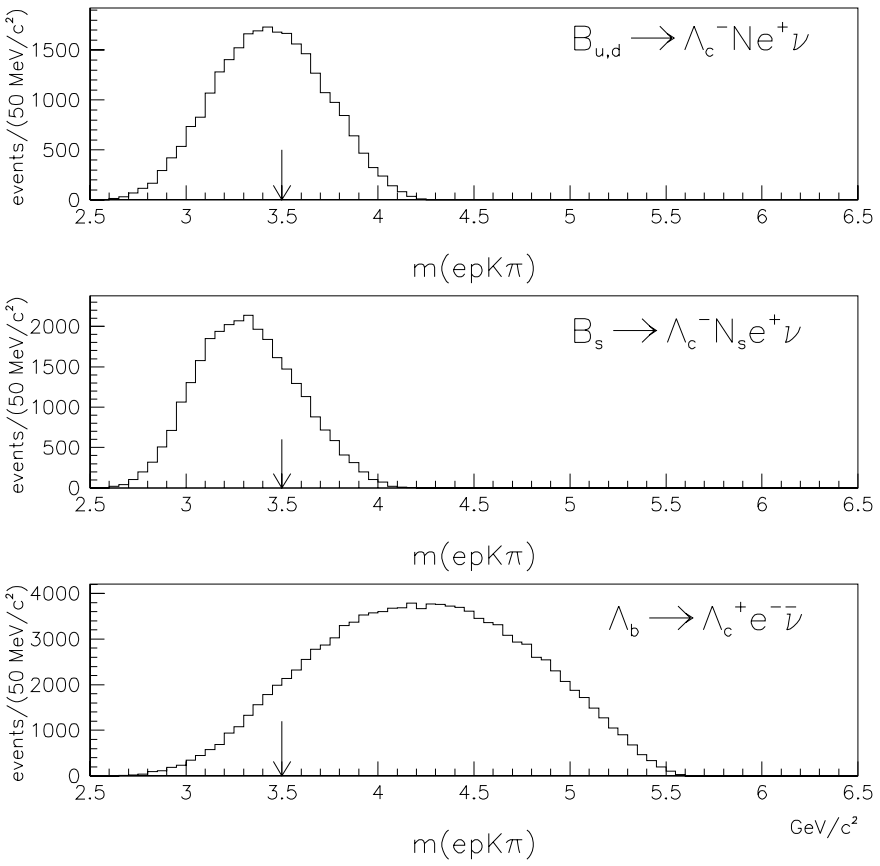

Figure 5.7: Monte Carlo $m(epK\pi)$ mass distributions for semileptonic b hadron decays with a Λ_c daughter.

5.2 Quark Pairs

Quarks are generally produced in quark-antiquark pairs. If one produces a Λ_c while the other eventually produces an electron, these events represent a potential sign-correlated background to our signal. Since in such events the angle between the Λ_c and the electron is not constrained by the mass of the parent particle, most of this background is eliminated by the upper limit on the $e\Lambda_c$ mass. However, in high-energy $\overline{p}p$ collisions, gluon splitting, which produces the quark and antiquark with small angular separation, becomes increasingly important. We consider both $\overline{b}b$ and $\overline{c}c$ pairs.

5.2.1 $\overline{b}b$ Pairs

If the $\overline{b}b$ pair resulted from gluon splitting, the two quarks are nearly collinear, and therefore might produce an electron from one b and a Λ_c from the other with small combined invariant mass. However, it should be noted that if the electron originates from the opposite b quark decay, this process produces wrong-sign pairs, of which none are seen in data. If the electron comes instead from the opposite charm decay, the process yields a right-sign pair, but is further suppressed by its softer p_T spectrum, as well as its branching fraction. If we assume that all b decays produce charm hadrons, and that the semileptonic branching fractions of these charm particles are about 20%, as in the case of the upper limit on D_s semielectronic decay, then the right-sign yield of this process is about the same as the wrong-sign yield resulting from direct b semileptonic decay. Since no wrong-sign pairs are observed, we neglect the right-sign contribution from $\overline{b}b$ pairs as well.

5.2.2 $\overline{c}c$ Pairs

In the case of $\overline{c}c$ pairs, the Λ_c must have resulted from one of the c quarks, and the electron from the other. Again, if the pair was not produced by gluon splitting, the combined mass in unrestricted, and most of these fail that cut. However, regardless of how the quark pair was produced, the Λ_c is prompt. Since $c\tau_{\Lambda_c} = 60$ μm, the 500 μm flight distance cut eliminates most of the possible contribution of this process to the signal. We therefore include no background from this source.

5.3 Conversion Electrons

As described in Section 3.5, conversion electrons result from processes unrelated to b hadron decay. Moreover, the conversion process does not preferentially boost either the electron or positron to higher energy than the other. Therefore we expect no sign correlation between real conversion electrons and Λ_c candidates.

We have isolated a sample of conversion electrons and can check this expectation. As shown in Figure 5.8, the rate is small, and there is no hint of a Λ_c signal among either right-sign or wrong-sign combinations. Indeed there is no suggestion that the sidebands are correlated, either. From Monte Carlo studies, this conversion sample represents about 70% of the actual conversions in our total data sample, and we expect that the unseen conversions behave in like manner. We therefore include no background from such $e\Lambda_c$ combinations.

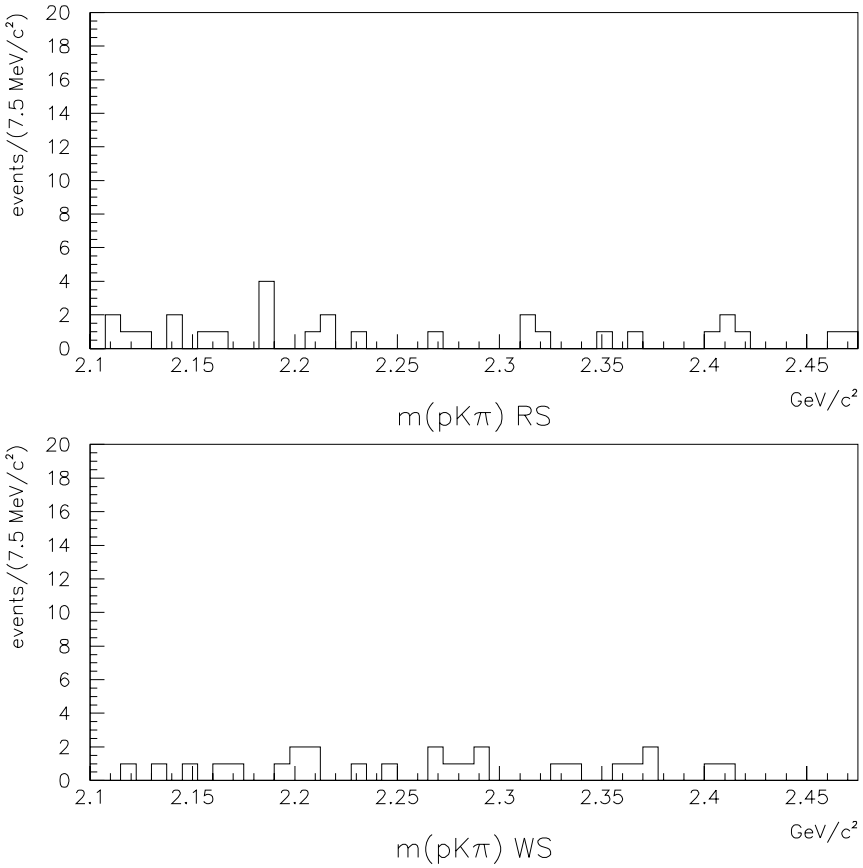

Figure 5.8: $pK\pi$ mass distribution in data for right-sign (top) and wrong-sign (bottom) $epK\pi$ combinations where the electron has been identified as a photon conversion daughter.

5.4 Charm Reflections

5.4.1 Λ_c Duplicates

Since the proton-pion dE/dx separation is only about 1σ in the relativistic rise region, many pions will have dE/dx measurements statistically consistent with those of protons. As a result, many real Λ_c's will enter twice into the mass spectrum, one with the correct mass assignment, and the other with the proton and pion mass assignments switched. If the mass spectrum resulting from the misassignment peaks underneath the Λ_c signal, it may deceptively enhance it.

This distribution may be checked with generator-level Monte Carlo since the most important cuts affecting the mass distribution are those on p_T and combined mass. As shown in Figure 5.9, the Λ_c duplicate distribution is relatively broad and flat in the region of interest. Fitting the combinatoric background below the signal has the effect of subtracting this background as well.

5.4.2 Reflections from Other Charm Hadrons

Charm mesons have three-prong decays corresponding to $\Lambda_c^+ \to pK^-\pi^+$:

- $D^+ \to \pi^+K^-\pi^+$
- $D_s^+ \to K^+K^-\pi^+$

When one of the daughters in these decays is misidentified as a proton, it is topologically indistinguishable from the process which interests us. Since most of the b quarks produce B mesons, these reflections are a high-rate, sign-correlated background to the Λ_c signal. As in the case with the Λ_c duplicates, the resulting mass distributions have been checked with generator-level Monte Carlo with B meson

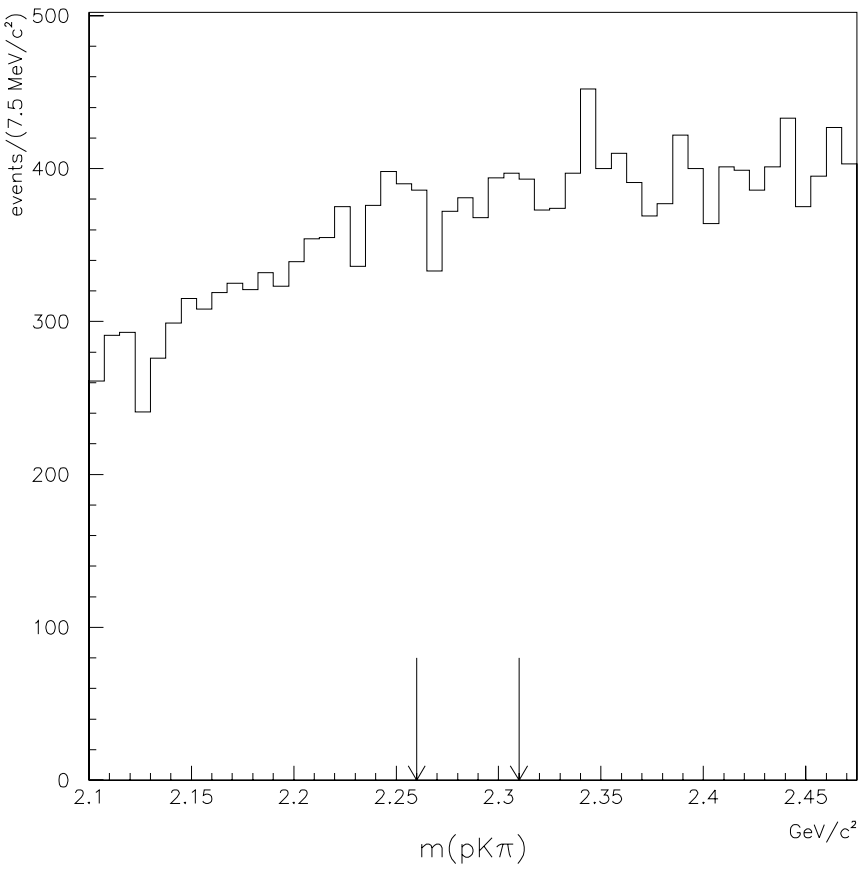

Figure 5.9: Generator level mass distribution of $\Lambda_c^+ \to pK^-\pi^+$ where the proton and pion masses have been switched. The arrows indicate the Λ_c mass region.

mixture $B_u : B_d : B_s = 0.375 : 0.375 : 0.15$. For the D and D_s, they are broad in the region of interest, as shown in Figures 5.10 and 5.11, and will be subtracted with the combinatoric background and Λ_c duplicates.

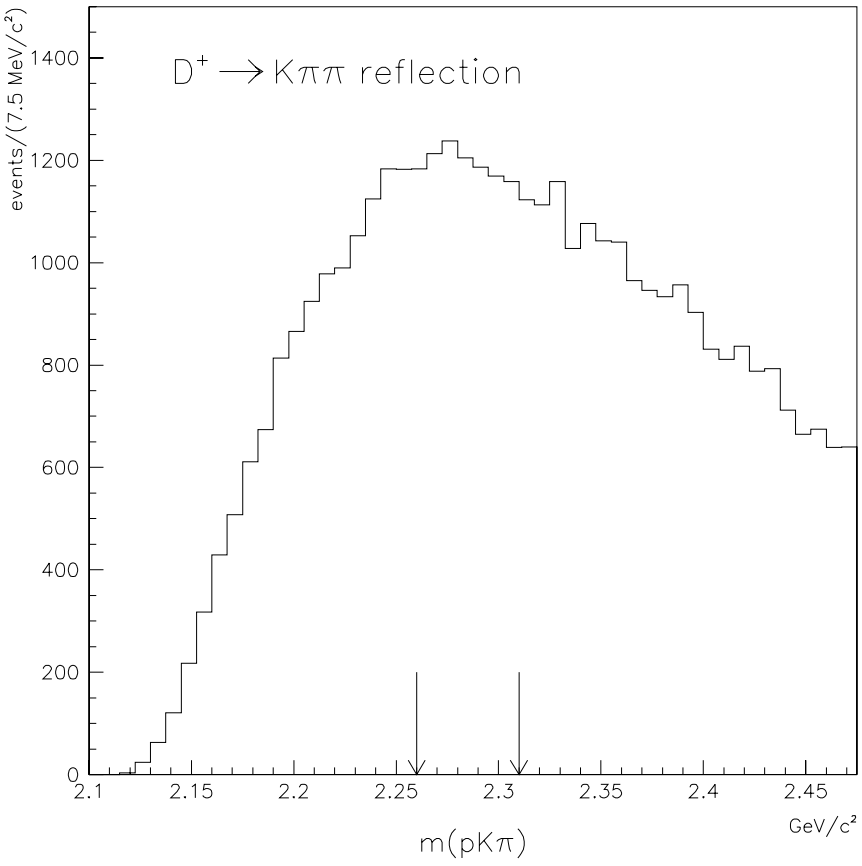

Figure 5.10: Reflections from $D^+ \to K\pi^+\pi^+$ events, using generator-level simulation of B and B_s mesons. The arrows indicate the Λ_c mass region.

More problematic is the case where a B meson gives a D^{*+} which decays to $D^0\pi^+$, the D^0 decaying further into $K^-\pi^+$. When the pion from the D^0 decay

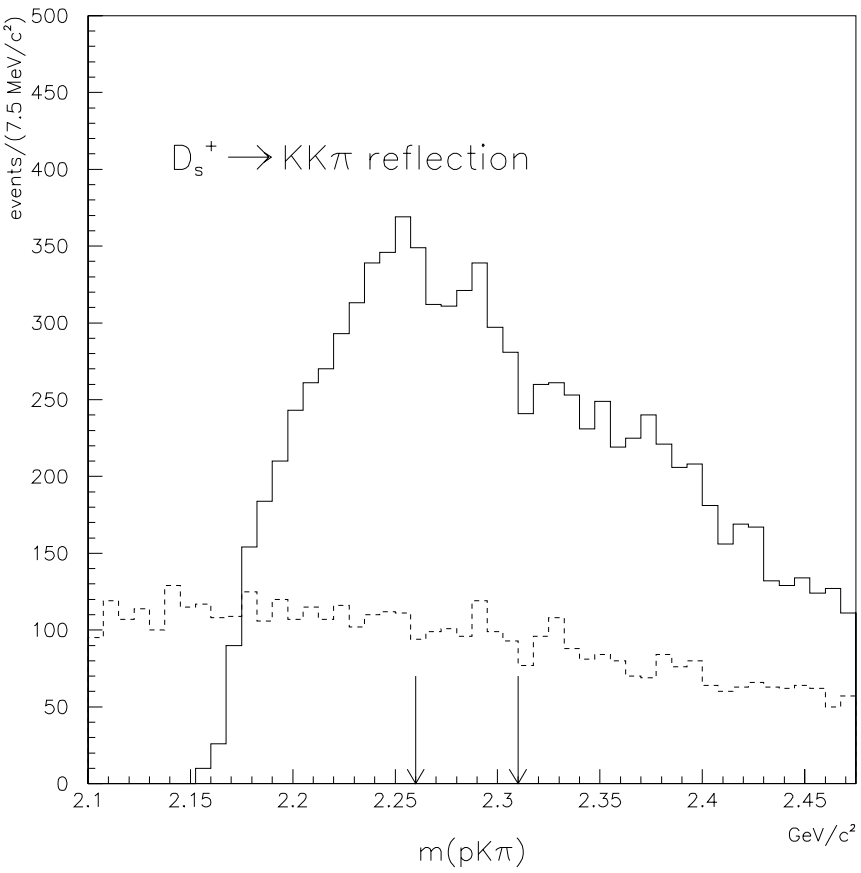

Figure 5.11: Reflections from $D_s^+ \to K^+K^-\pi^+$ events, using generator-level simulation of B_s mesons. The solid histogram is from misassigning the proton the kaon mass, and the dashed curve is from misassigning the proton the pion mass and the pion the kaon mass.

is misassigned the proton mass, the reflected mass distribution strongly peaks underneath the Λ_c signal, as shown in Figure 5.12. Several factors serve to suppress these reflections: first, the D^0 is long-lived, with $c\tau = 124.4$ μm. However, the D^0 may decay close enough to the D^{*+} decay vertex that the $K^-\pi^+\pi^+$ combination may be fit into one vertex, albeit with a large χ^2. Second, the pion from the D^{*+} decay is typically very soft and is therefore not reconstructed.

However, it is possible to entirely eliminate this background. The D^{*+} mass difference distribution, shown in Figure 5.13, shows that all the D^{*+}'s have mass differences $m(K^-\pi^+\pi_s^+) - m(K^-\pi^+) < 0.15$ GeV/c^2, where π_s indicates the pion from the D^{*+} decay. At the same time, as shown in Figure 5.14, generator-level Monte Carlo indicates that very few Λ_c's pass this cut when the proton is misassigned the pion mass. This number is further reduced if one makes a mass window cut around the D^0 as shown in Figure 5.15. Hence few Λ_c's are lost when all D^{*+}'s are eliminated from the sample.

5.5 Combinatorial Background

The combinatorial background results from the random association of any three tracks in the event passing the cuts. This background forms most of the wrong-sign mass distribution, which shows no evidence for a Λ_c-like signal. It is subtracted by fitting a linear function underneath the gaussian signal function.

5.6 Hadronic Fake "Electrons"

Hadrons may sometimes shower early in the calorimeter, leaving significant electromagnetic energy deposition which may be mistaken for that of an electron.

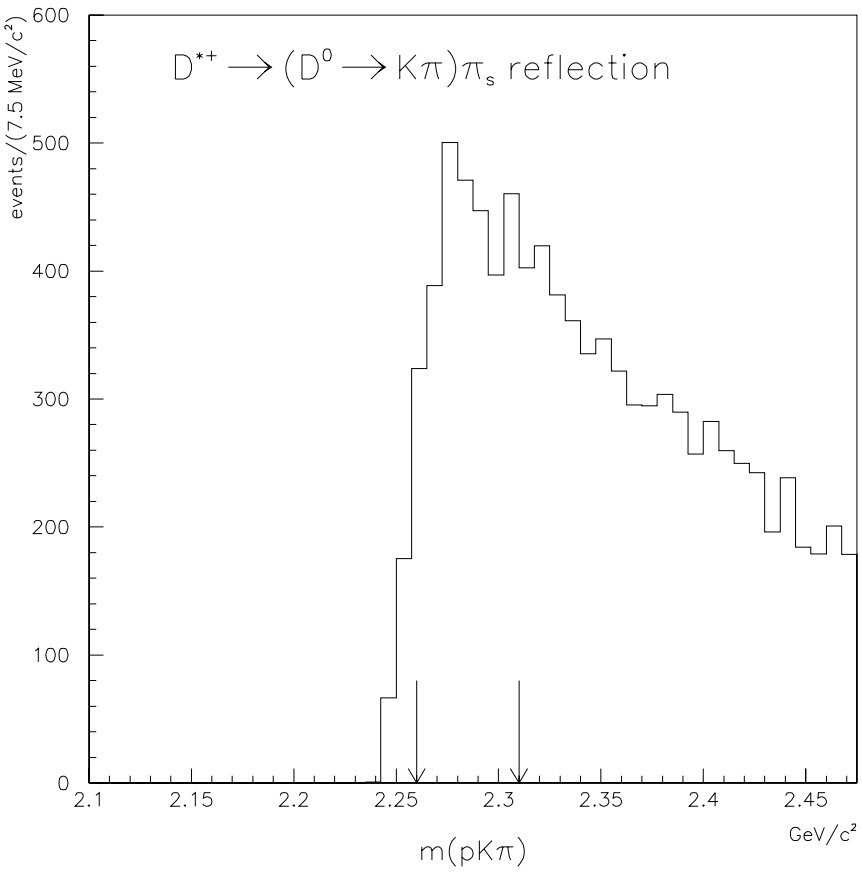

Figure 5.12: Reflections from $D^{*+} \rightarrow D^0\pi_s^+$, $D^0 \rightarrow K^-\pi^+$ events, using generator-level Monte Carlo. The pion from the D^0 decay has been misassigned the proton mass. If the other pion is assigned the proton mass, the spectrum lies in a higher mass region than shown here.

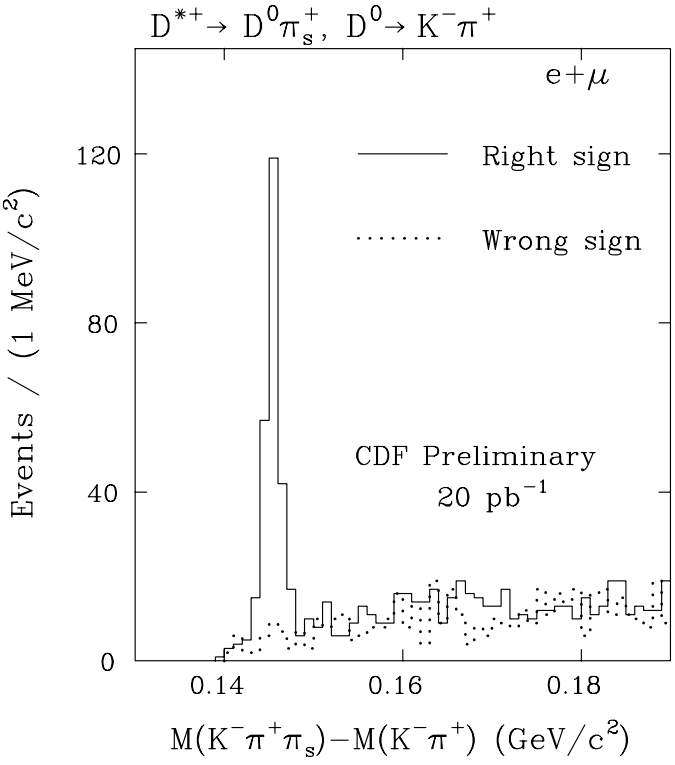

Figure 5.13: $m(K\pi\pi_s) - m(K\pi)$ mass difference distribution for the decay $D^{*+} \rightarrow D^0\pi_s^+$ followed by $D^0 \rightarrow K^-\pi^+$.

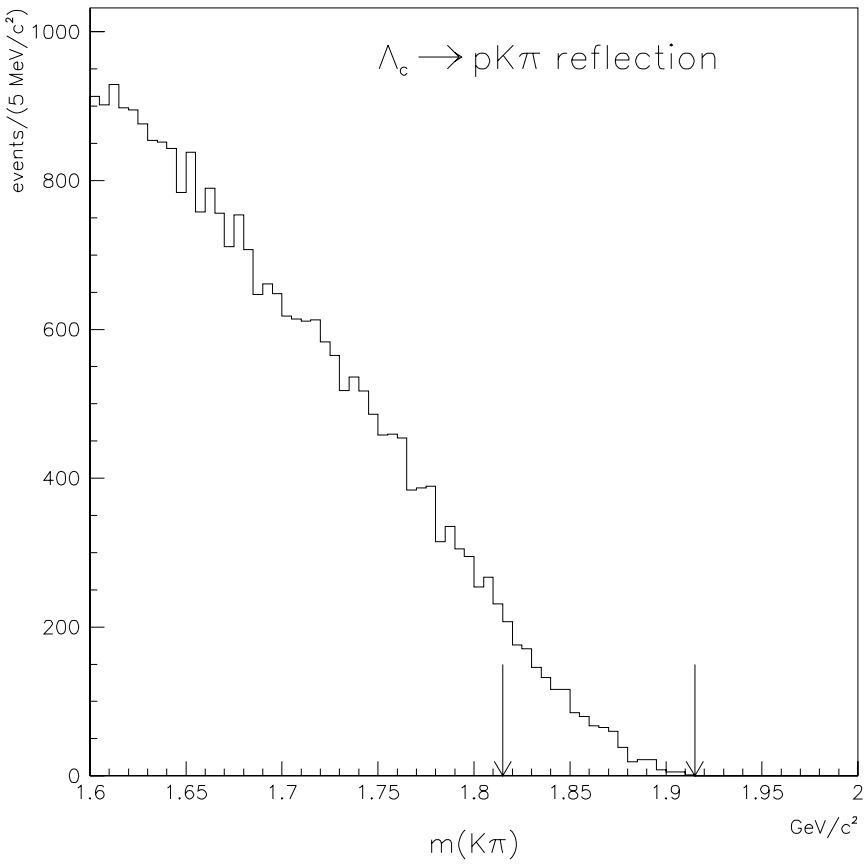

Figure 5.14: $m(K\pi\pi_s) - m(K\pi)$ mass difference distribution for Λ_c decay, where the proton has been given the pion mass and combined with the K into the D^0. The region below 0.15 GeV/c^2 is only 0.2% of this distribution.

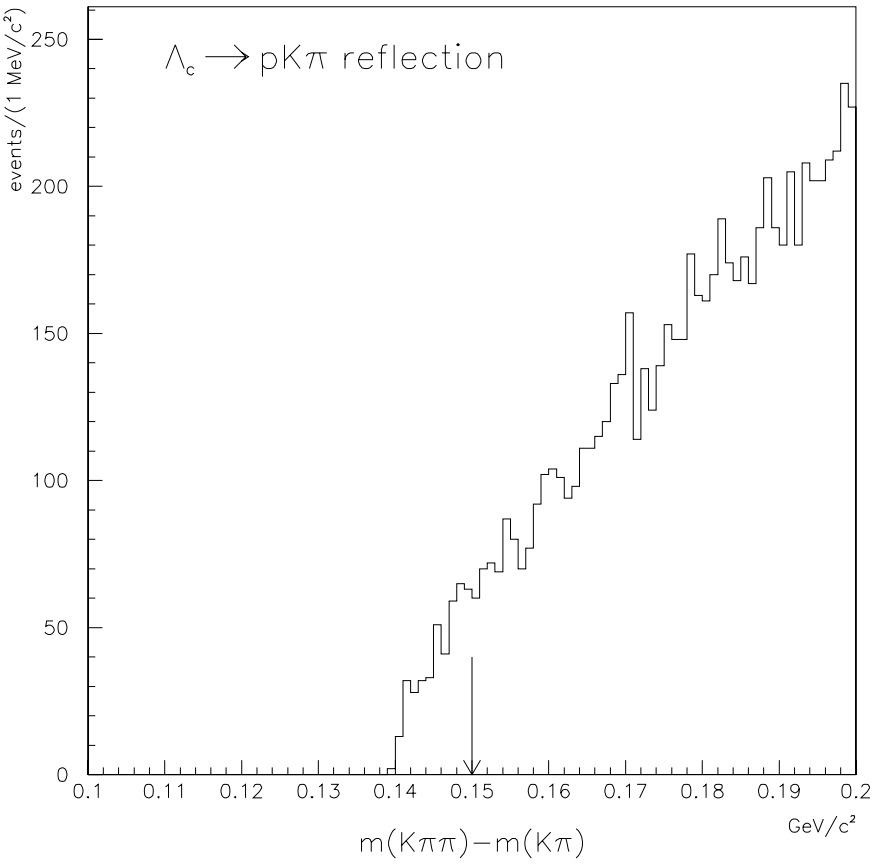

Figure 5.15: $m(K\pi)$ mass distribution for Λ_c decay, where the proton has been given the pion mass. The arrows demarcate the D^0 mass window, from 1.815 to 1.915 GeV/c^2. If the Λ_c pion is used instead of the proton, the resulting mass distribution lies entirely below this plot.

Possible sign correlations with these fake electrons have been investigated using data: a high-p_T track which has not been identified as an electron candidate is taken as the fake "electron" and associated with a Λ_c candidate. The results are shown in Figure 5.16. There is no evidence of a sign correlation either in the signal or sideband regions.

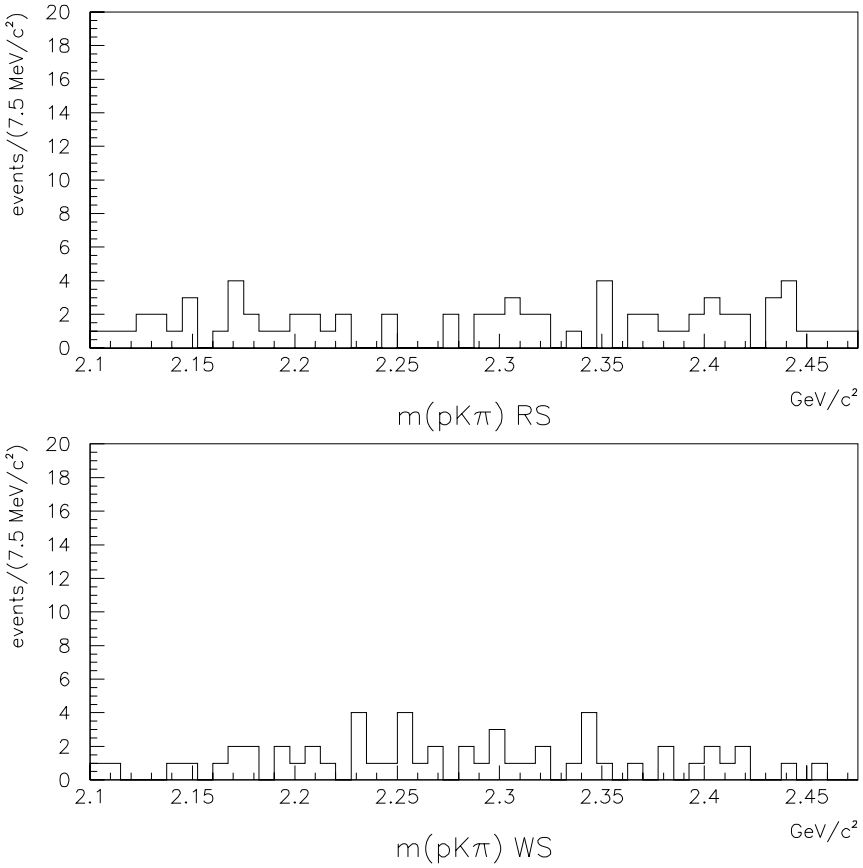

Figure 5.16: $pK\pi$ mass distribution for right-sign (top) and wrong-sign (bottom) combinations with a high-p_T non-electron track.

5.7 Conclusion

In this chapter we have enumerated the possible backgrounds to the right-sign Λ_c signal and demonstrated that they either contribute negligibly to the signal, are eliminated by the cuts, or have been subtracted by fitting the sideband distribution. We therefore take the 35.7 reconstructed right-sign Λ_c events to be evidence of Λ_b production and semileptonic decay at CDF. In the next chapter, we will use these events to measure the rate of this process.

Chapter 6

Rate Measurement

Having concluded that the observed sign-correlated $e\Lambda_c$ signal is due to Λ_b production and semileptonic decay, we can calculate the rate of this process. We use the formula

$$\begin{aligned} &\sigma_b(p_T^b > 10.5 \text{ GeV}/c, |y| < 1)\times \\ &f_{\Lambda_b}\text{Br}(\Lambda_b \to \Lambda_c^+ e^- \overline{\nu}_e X)\text{Br}(\Lambda_c^+ \to pK^-\pi^+) \\ &= \frac{N_{e\Lambda_c}}{2\mathcal{L}\mathcal{E}} \end{aligned} \tag{6.1}$$

where the terms are defined as follows:

- $\sigma_b(p_T > 10.5 \text{ GeV}/c, |y| < 1)$: the b quark production cross section for the specified p_T and rapidity range,

$$y = \frac{1}{2}\ln\left(\frac{E + p_z}{E - p_z}\right), \tag{6.2}$$

- f_{Λ_b}: probability of producing a Λ_b from direct b fragmentation or decay of higher resonance b baryons,

- $\text{Br}(\Lambda_b \to \Lambda_c^+ e^- \overline{\nu}_e X)$: the inclusive semileptonic branching fraction,

- $\mathrm{Br}(\Lambda_c^+ \to pK^-\pi^+)$: the exclusive Λ_c^+ branching fraction,
- $N_{e\Lambda_c}$: number of right-sign $e\Lambda_c$ combinations observed above background,
- $\mathcal{L}$: integrated luminosity of the data sample, and
- $\mathcal{E}$: the efficiency and acceptance.

We already have one factor,

$$N_{e\Lambda_c} = 35.7 \pm 9.4 \tag{6.3}$$

from Section 4.4. $\mathcal{L}$ and $\mathcal{E}$ are the subjects of the next sections.

6.1 Luminosity

The instantaneous luminosity can be calculated either from accelerator parameters or by comparing trigger rates with another experiment, in this case UA4 at $S\overline{p}pS$, which has performed an absolute cross section measurement, albeit at a different center-of-mass energy. [2] The first method gives an uncertainty of about 10%, and is used at CDF mostly as a check on the second method, which is described below. [3]

The BBC trigger rate at a given center-of-mass energy is the product of the BBC trigger cross section, $\sigma_{BBC}^{\sqrt{s}}$, and the luminosity as calculated from accelerator parameters, $L_{acc}^{\sqrt{s}}$, corrected by a factor $\chi^{\sqrt{s}}$ which takes into account multiple interactions per beam crossing,

$$R_{BBC}^{\sqrt{s}} = \sigma_{BBC}^{\sqrt{s}} L_{acc}^{\sqrt{s}} / \chi^{\sqrt{s}}, \tag{6.4}$$

The trigger cross section includes all physical processes which would produce a BBC trigger. As noted in Section 2.2.5, the average collision rate in 1992-93 was

more than one per bunch crossing. Using Poisson statistics, the probability of a second interaction given the first is found to be

$$P_2(R_{BBC}^{\sqrt{s}}) = 1.75 \times 10^{-6} \times R_{BBC}^{\sqrt{s}}, \tag{6.5}$$

where $R_{BBC}^{\sqrt{s}}$ is the BBC rate in Hertz. This probability has been checked with vertex reconstruction in data, which yields $(1.91 \pm 0.08) \times 10^{-6}$ as the coefficient, which is within 2σ of the predicted value. The correction factor is then

$$\chi^{\sqrt{s}} = 1 + P_2(R_{BBC}^{\sqrt{s}}). \tag{6.6}$$

The cross section at $\sqrt{s} = 1800$ GeV is therefore related to that at $\sqrt{s} = 546$ GeV by the ratio

$$\frac{\sigma_{BBC}^{1800}}{\sigma_{BBC}^{546}} = \frac{R_{BBC}^{1800}}{R_{BBC}^{546}} \frac{L_{acc}^{546}}{L_{acc}^{1800}} \frac{\chi^{1800}}{\chi^{546}}, \tag{6.7}$$

which is insensitive to systematic effects in the overall normalization. The rates, $R_{BBC}^{\sqrt{s}}$, are measured quantities, and the instantaneous luminosities, $L_{acc}^{\sqrt{s}}$, are calculated from accelerator parameters, with the 10% uncertainties dropping out in the ratio. After further small corrections are made for energy-dependent beam-beam interaction effects, all that remains is to calculate σ_{BBC}^{546}. As mentioned above, a calculation using accelerator parameters gives about a 10% error,

$$\sigma_{BBC}^{546} = 32.8 \pm 3.6 \text{ mb}. \tag{6.8}$$

We may also use the UA4 cross section measurement, which was also performed at $\sqrt{s} = 546$ GeV. This measurement must be corrected for geometric acceptance and the measured effects of radiation damage on the BBC, and yields a 5% error,

$$\sigma_{BBC}^{546} = 37.1 \pm 2.1 \text{ mb}. \tag{6.9}$$

These two measurements are averaged, weighted by their respective errors, to yield

$$\sigma_{BBC}^{546} = 36.0 \pm 1.8 \text{ mb} \tag{6.10}$$

which then implies

$$\sigma_{BBC}^{1800} = 46.8 \pm 3.2 \text{ mb.} \tag{6.11}$$

The instantaneous luminosity is then calculated from the instantaneous BBC rate,

$$L = \frac{R_{BBC}^{1800}}{\sigma_{BBC}^{1800}}, \tag{6.12}$$

where σ_{BBC}^{1800} is that measured above. The integrated luminosity is defined as

$$\mathcal{L} = \int L dt, \tag{6.13}$$

and is calculated for each data-taking run. The sum over good runs used in this analysis represents an integrated luminosity of 19.3 ± 0.8 pb^{-1}.

6.2 Efficiency

The reconstruction efficiency for finding the $e\Lambda_c$ pair from Λ_b decay is the product of five factors,

$$\mathcal{E} = \mathcal{E}_{MC}\mathcal{E}_{CTC}\mathcal{E}_{SVX}\mathcal{E}_{dE/dx}\mathcal{E}_{L3}. \tag{6.14}$$

The first is the efficiency computed by simulating the event in the detector; this factor also models the detector acceptance. The other factors are the CTC and SVX tracking efficiencies, the efficiency of the proton dE/dx cut, and the Level 3 trigger efficiency. All but the last efficiency are given as relative to the preceding ones. The Level 3 efficiency is relative to the detector acceptance, but is considered independent of the others.

6.2.1 Monte Carlo Efficiency

The b quark cross section, as generally quoted, is proportional to the number of b quarks produced above a p_T threshold p_T^{min} and within a rapidity window $|y| < 1$.

The number of b quarks produced in this kinematic window is simply the cross section multiplied by the integrated luminosity,

$$N_b = \mathcal{L}\sigma(p_T > p_T^{min}, |y| < 1). \tag{6.15}$$

The efficiency must be defined relative to this kinematic window. However, we do not know the original b quark energy or direction for any reconstructed Λ_b. The reconstructed events may in principle originate from b quarks outside the window. For simulation purposes, we define a larger window in which to generate events. We note, first, that CDF is sensitive to electrons only with $p_T > 6$ GeV/c. The Monte Carlo b quark p_T spectrum for these electrons is shown in Figure 6.1. By convention, we set p_T^{min} to where 90% of all these electrons originate from b quarks with $p_T > p_T^{min}$. In this case, p_T^{min} is set to 10.5 GeV/c.

With $p_T > 10.5$ GeV/c, we see that b quarks with $|y| > 2$ fall outside the CDF acceptance. Thus we count in simulation reconstructed events where the generated b quarks fall in the larger rapidity window, $|y| < 2$, but normalize the efficiency to the number of b quarks generated in the $|y| < 1$ window. If the former number is denoted by $N^{rec}_{|y|<2}$ and the latter by $N^{b}_{|y|<1}$, the efficiency calculation is

$$\mathcal{E}_{MC} = \left(\frac{N^{rec}_{|y|<2}}{N^{b}_{|y|<1}} \right)_{MC} \tag{6.16}$$

where the numerator and denominator are counted from the same Monte Carlo sample.

As noted previously, the standard Monte Carlo does not include the effects of the underlying event and fragmentation jet particles. We calculate this efficiency factor independently using the cut optimization Monte Carlo with its PYTHIA-generated underlying event and fragmentation jets. We see the efficiency decrease by 6%, and we correct the reconstruction efficiency accordingly.

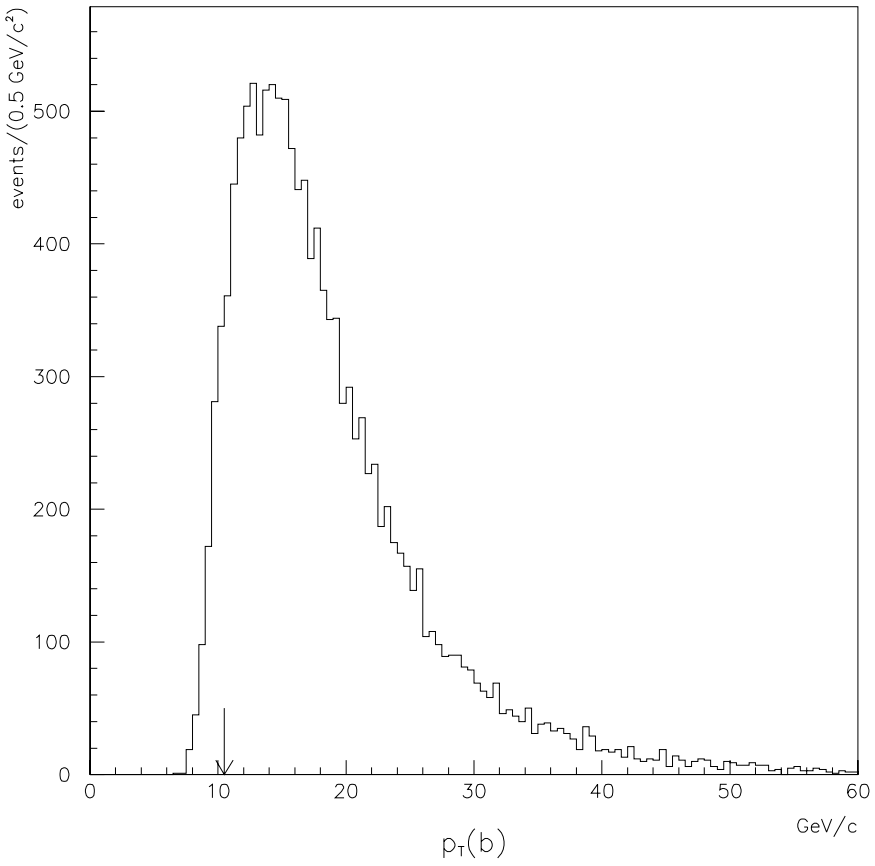

Figure 6.1: b quark p_T spectrum for events with electron $p_T > 6$ GeV/c. Ninety percent of the events have b quark $p_T > 10.5$ GeV/c.

6.2.2 Tracking Efficiency

The tracking efficiency can be broken into two parts: the probability that the track is reconstructed in the CTC, and the probability that the track is linked to an SVX track. The CTC tracking efficiency has been parameterized as a function of an isolation variable Q, which is defined as follows:

$$Q = 1 - \min(1, N_{overlap}/50) \tag{6.17}$$

where $N_{overlap}$ is the number of times the track overlaps with other tracks in the event. The overlaps are counted at each sense wire layer, and are counted twice for the innermost 30 layers, to account for hits from unreconstructed soft tracks. Two tracks are said to overlap at a layer if they are separated by less than a certain distance—0.2 cm for the inner 30 layers, 0.3 cm for the outer 54—at the layer's radius.

The tracking efficiency as a function of Q is given by [26]

$$\mathcal{E}(Q) = \begin{cases} \mathcal{E}_{max} & Q > 0.5 \\ \mathcal{E}_{max}[x_0 + (2 - 2x_0)Q] & Q < 0.5 \end{cases} . \tag{6.18}$$

A fit to the data gives $x_0 = 0.40 \pm 0.02$. [26] $\mathcal{E}_{max}$, the plateau efficiency, has been measured to be $(98.5 \pm 1.4)\%$, by embedding simulated tracks into raw data events and testing whether the tracks are reconstructed. Knowing the efficiency function, we can correct the measured Q distributions of the reconstructed Λ_b events. This corrected distribution reflects the sum of events found and events lost due to tracking inefficiency. Dividing the number of events found by the corrected number gives the overall tracking efficiency.

Using Figure 4.16, we define the Λ_c signal region to be between 2.26 and 2.31 GeV/c^2. There are 96 events in this window, which also contains 99.7%

of the gaussian peak of 35.7 ± 9.4 events. The sideband-subtracted Q distributions for the Λ_b daughter tracks are shown in Figure 6.2. Most of the signal tracks have $Q > 0.5$, and are thus reconstructed at the plateau efficiency. As a result, most of the events are reconstructed at the plateau efficiency for four tracks, as shown in Figure 6.3. The efficiency for events within the signal region, including both signal and background events, is 0.8948 ± 0.0010 relative to the plateau efficiency. The efficiency in the sidebands above and below the signal region is 0.9265 ± 0.0004. Figure 6.3 shows that the event efficiency distributions in the upper and lower sideband regions are similar. Assuming that the efficiency in the sideband regions is the same as that for the background events underneath the signal, we perform a weighted subtraction to calculate the efficiency for the pure Λ_c sample, and get 0.841 ± 0.023. Combining this number with the plateau efficiency per track, the total CTC tracking efficiency is

$$\mathcal{E}_{CTC} = (0.985 \pm 0.014)^4 (0.841 \pm 0.023) \quad (6.19)$$

$$= 0.792 \pm 0.050. \quad (6.20)$$

The SVX tracks we use in this analysis require only the coincidence of two hits when following the CTC track into the SVX volume, and that the CTC track be such that it should hit all four SVX layers. The quality cuts on the track are minimal. If the CTC tracks a charged particle which is actually outside the SVX acceptance—hence its SVX link is spurious—the tracks will only contribute to the background and not to the signal. If, on the other hand, the particle has left hits in the SVX, but the reconstruction algorithm has selected the wrong hits, the SVX track is steered wrong. Since the SVX does not significantly enhance the CTC mass resolution, the Λ_c's mass measurement is not affected; the steering only affects the topological quantities such as flight distance and impact parameters. However,

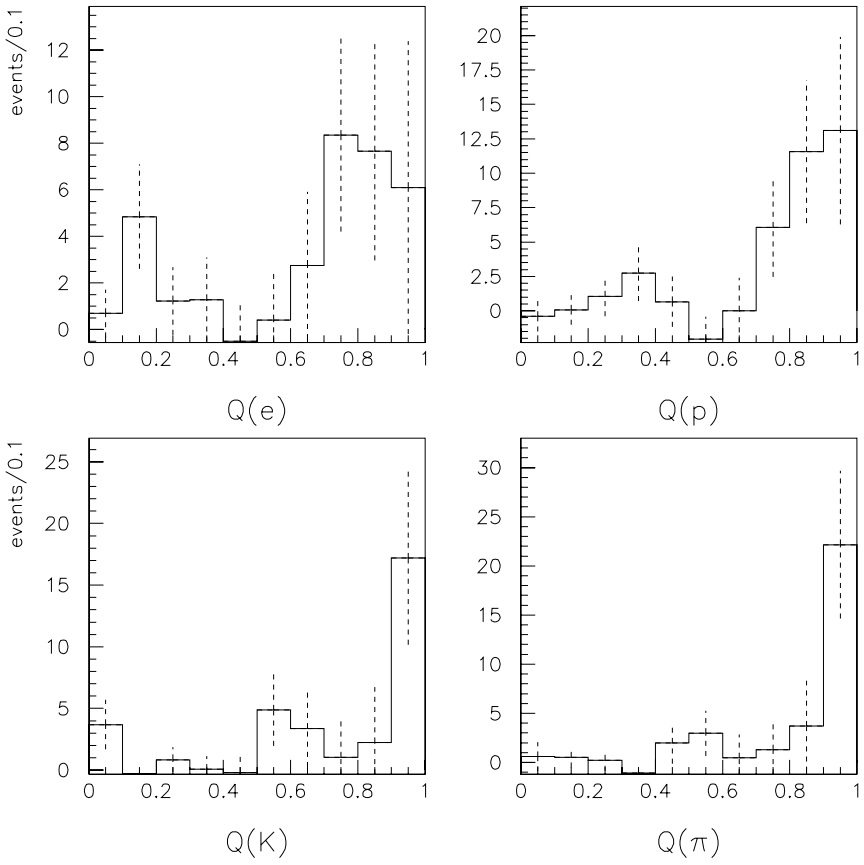

Figure 6.2: Sideband-subtracted Q distributions.

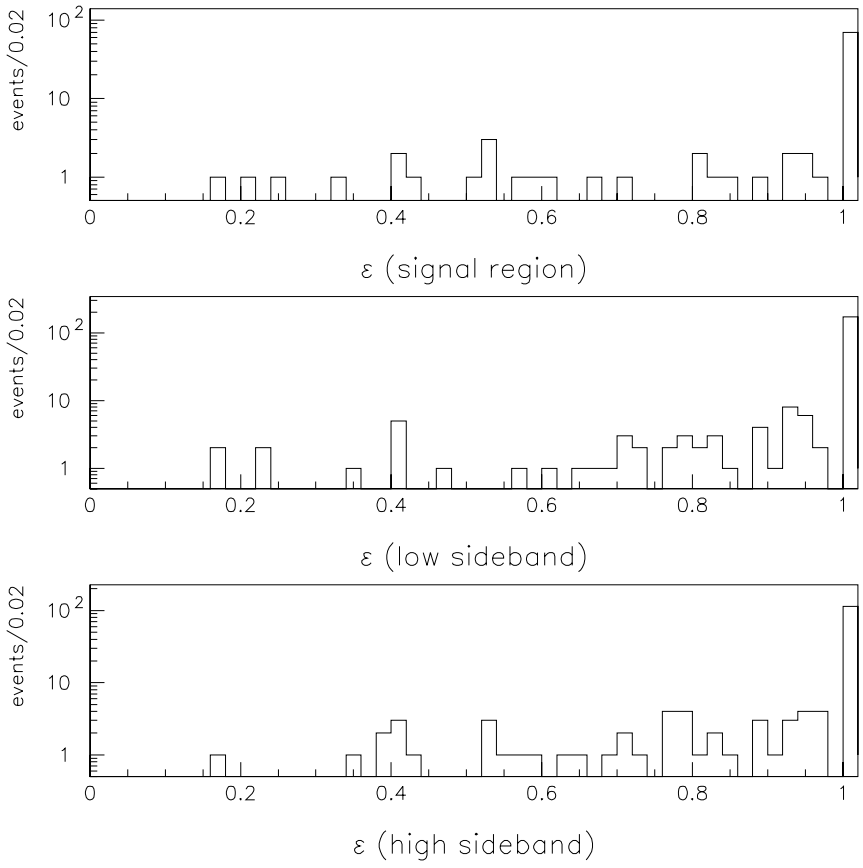

Figure 6.3: Event efficiency distributions for events in the signal (top), low sideband (middle), and high sideband (bottom) regions.

since the SVX track reconstruction algorithm is not biased towards the beam, this effect smears the quantities symmetrically and does not change the reconstruction efficiency. We therefore take $\mathcal{E}_{SVX}$ to be the probability of finding at least two hits out of the four possible. This efficiency is measured to be 97.4% in an early run, and 96.0% in a late one, with 1 or 2% statistical uncertainty in each. [27] We take the average, 97%, to be the single track efficiency, and the difference, 1.4%, as the uncertainty. The SVX tracking efficiency for the four tracks is therefore $(89 \pm 6)\%$.

6.2.3 dE/dx Efficiency

We calculate the dE/dx efficiency for the proton using 2 GeV/c protons and antiprotons from reconstructed Λ^0 and $\overline{\Lambda^0}$ decays. The mass spectrum is plotted in Figure 6.4 along with the proton p_T spectrum. The differences between the corrected and predicted dE/dx values, shown in Figure 6.5, is centered near zero and has a width of 17 TDC counts, which is narrower than the 21 counts found for inclusive hadrons. [28] This narrower resolution is due to the higher p_T of the sample. If we include softer protons, the overall resolution is 20 counts. In this analysis, the dE/dx of the proton is required to be within 42 counts, or twice the resolution found for inclusive hadrons, of the predicted value. Using the proton dE/dx plot, this cut has an efficiency of 0.986 ± 0.005, where the error is calculated by considering a 1σ fluctuation of the mean of the difference.

6.2.4 Level 3 Efficiency

The Level 3 trigger requires the reconstruction of a 6 GeV/c track in the event by the Level 3 filter program. This reconstruction algorithm is simpler than that used in offline because of speed constraints. This simplification results in a slight

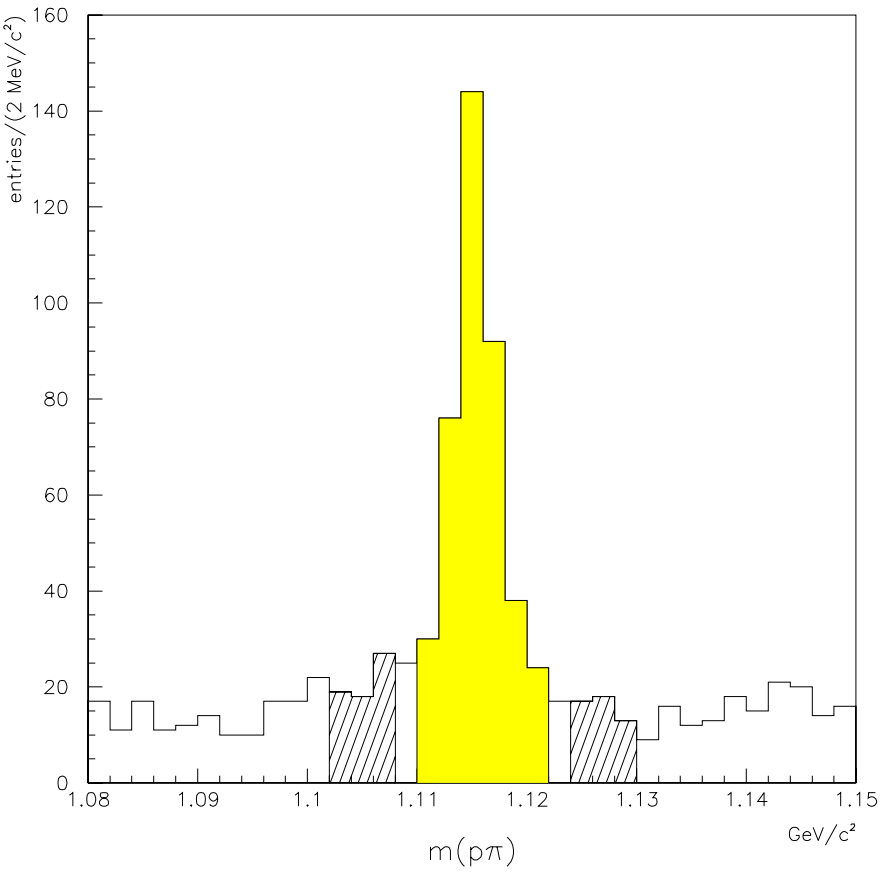

Figure 6.4: $\Lambda^0 \to p\pi^-$ mass spectrum, including charge conjugate decays, used in the proton dE/dx study. The signal region is shaded, and the sidebands hatched.

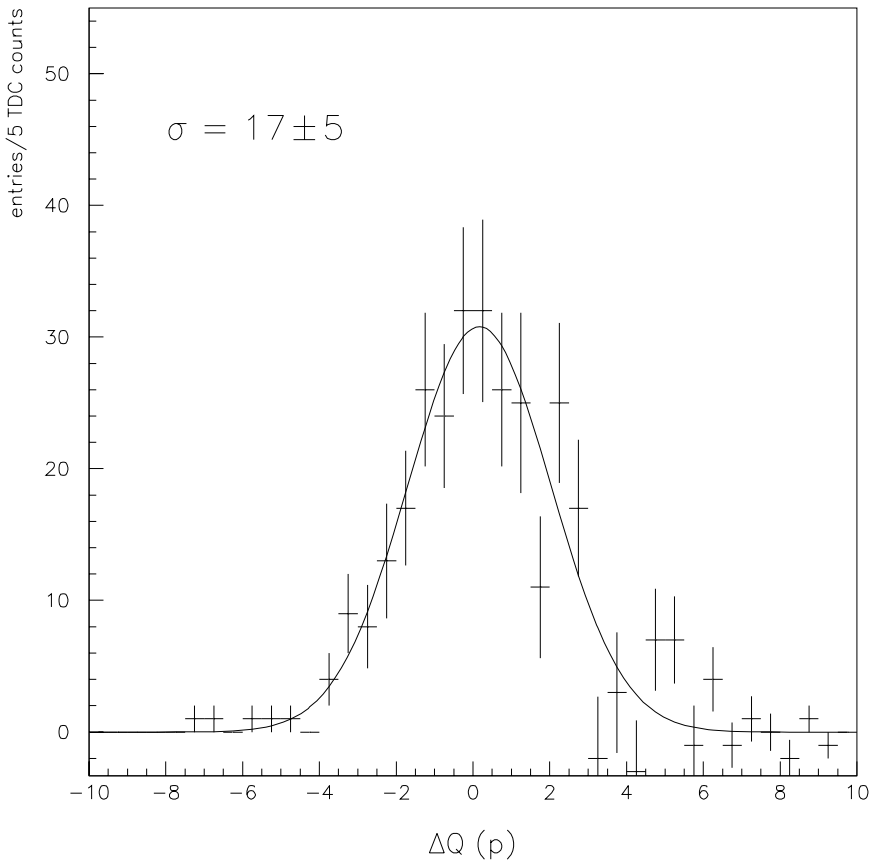

Figure 6.5: Difference between corrected and predicted dE/dx values for the protons and antiprotons, sideband subtracted.

	efficiency
Monte Carlo	$(4.9 \pm 0.2) \times 10^{-4}$
proton dE/dx	0.986 ± 0.005
CTC tracking	0.792 ± 0.050
SVX tracking	0.89 ± 0.06
Level 3 trigger	0.97 ± 0.02
total efficiency	$(3.3 \pm 0.3) \times 10^{-4}$

Table 6.1: Electron and Λ_c reconstruction efficiencies.

inefficiency, which has been measured by hand-scanning $J/\psi \to \mu\mu$ events, cross-checked with J/ψ events which fail Level 3 but were reconstructed offline. The efficiency is measured to be $97 \pm 2\%$ in this dimuon sample. [29] We take this to be the efficiency in the single electron sample as well, since the most important features of the sample—high-p_T tracks in a b environment—are the same.

6.2.5 Total Efficiency

The efficiency calculation is summmarized in the Table 6.1. The total efficiency is $(3.3 \pm 0.3) \times 10^{-4}$.

6.3 Calculation

To summarize the previous sections, we have the following numbers:

- $N_{e\Lambda_c} = 35.7 \pm 9.4$,
- $\mathcal{L} = 19.3 \pm 0.8$ pb^{-1}, and

- $\mathcal{E} = (3.3 \pm 0.3) \times 10^{-4}$.

Therefore the Λ_b production and semileptonic decay rate is calculated to be

$$\begin{aligned} &\sigma_b(p_T^b > 10.5 \text{ GeV}/c, |y| < 1)\times \\ &f_{\Lambda_b}\text{Br}(\Lambda_b \to \Lambda_c^+ e^- \overline{\nu}_e X)\text{Br}(\Lambda_c^+ \to pK^-\pi^+) \\ &= 2.8 \pm 0.72 \text{ nb} \end{aligned} \tag{6.21}$$

where the error at this point is entirely the statistical error on $N_{e\Lambda_c}$. The systematic uncertainties, including those from the luminosity and efficiency calculation, will be computed in the next chapter.

Chapter 7

Systematic Uncertainties

The uncertainty in the rate calculation of the previous chapter reflects statistical fluctuations in the actual number of observed events. However, there are additional uncertainties which arise from assumptions made in the process of the calculation. Systematic uncertainty is a measure of the robustness of these assumptions, and of the calculation with respect to them. These uncertainties can be divided into two categories: first, those which reflect the uncertainty in measured parameters and detector simulation, and, second, those which primarily reflect an uncertainty in theory.

7.1 Λ_b Mass

The mass of the Λ_b has been recently measured at CDF using 115 pb^{-1} of data to be $5623 \pm 5(stat.) \pm 4(syst.)$ MeV/c^2. [30] We have used this mass as the central value in our simulation. To find the 1σ variation, we add the two uncertainties in quadrature and re-run our simulation with the higher and lower masses. As expected for the small mass uncertainty, we find the variation in the rate to be

statistically insignificant.

7.2 Λ_b Lifetime

The Λ_b lifetime has been measured by various experiments at LEP using $\Lambda_c\ell$, $\Lambda\ell$, and $p\ell$ charge correlations. [31] The average result is $c\tau = 357 \pm 21$ μm, which we use as the Λ_b lifetime in our simulation. Instead of regenerating the entire Monte Carlo sample with longer or shorter lifetimes, we have applied a "reweighting" algorithm: we compute the ratio of normalized $c\tau$ distributions

$$w(x) = \frac{c\tau}{c\tau'} e^{-x(\frac{1}{c\tau'} - \frac{1}{c\tau})} \tag{7.1}$$

where $c\tau = 357$ μm, $c\tau'$ is the new lifetime, and x is the proper lifetime of a given event. Since we know x for each generated event, we can compute $w(x)$, which we then use to weight the event when filling a histogram, such as for the $pK\pi$ mass. When this method is used, we see that the reconstruction efficiency changes by $\pm 3\%$, changing the rate by the same amount.

7.3 Level 2 Trigger

The Level 2 trigger turn-on was implemented independently of the detector Monte Carlo. We vary the parameters of the turn-on according to the statistical uncertainties in the fit, and see a $\pm 5\%$ effect.

7.4 Hadronic Leakage Modeling

The primary uncertainty in the detector model used in the Monte Carlo lies in its modeling of the leakage of electromagnetic energy into the hadron calorimeters.

We can check our simulation using D^+'s reconstructed in data; Monte Carlo studies indicate that the electron response is nearly identical for Λ_c^+'s and D^+'s. We fit the D^+ peak for different Hadem cuts, resulting in the effectively background-subtracted Hadem distributions shown in Figures 7.1 and 7.2. It is known that the detector model gives too sharp a distribution due to its bremsstrahlung model. However, this effect should only shift small-Hadem events. The shifted value remains small, below 0.04, whereas our cut is at 0.10. The data distribution is broader than Monte Carlo, but is consistent with 100% efficiency for the loose cut of Hadem< 0.10. We therefore use the Monte Carlo calculation of the Hadem cut efficiency and allow it to fluctuate up to 100% efficiency, and down by the same amount. The efficiency for finding electrons relevent for our $e\Lambda_c$ signal changes by $\pm 12\%$, which we take to be our systematic uncertainty for this model uncertainty.

7.5 Underlying Event

The standard Monte Carlo generates only the Λ_b, ignoring the other particles that are inevitably produced as a result of the $\overline{p}p$ collision. This "underlying event" consists primarily of two components, particles from additional interactions between the initial partons, and particles produced in conjunction with the b quark, including final state radiation and fragmentation debris. The reconstruction efficiency has already been corrected by -6%, reflecting the difference between PYTHIA-generated Λ_b's with and without the accompanying particles. This correction includes models of both components of the underlying event, and we also use it as our systematic uncertainty.

Since both components of the underlying event kill events by producing particles near the electron, each component must individually increase the kill rate—

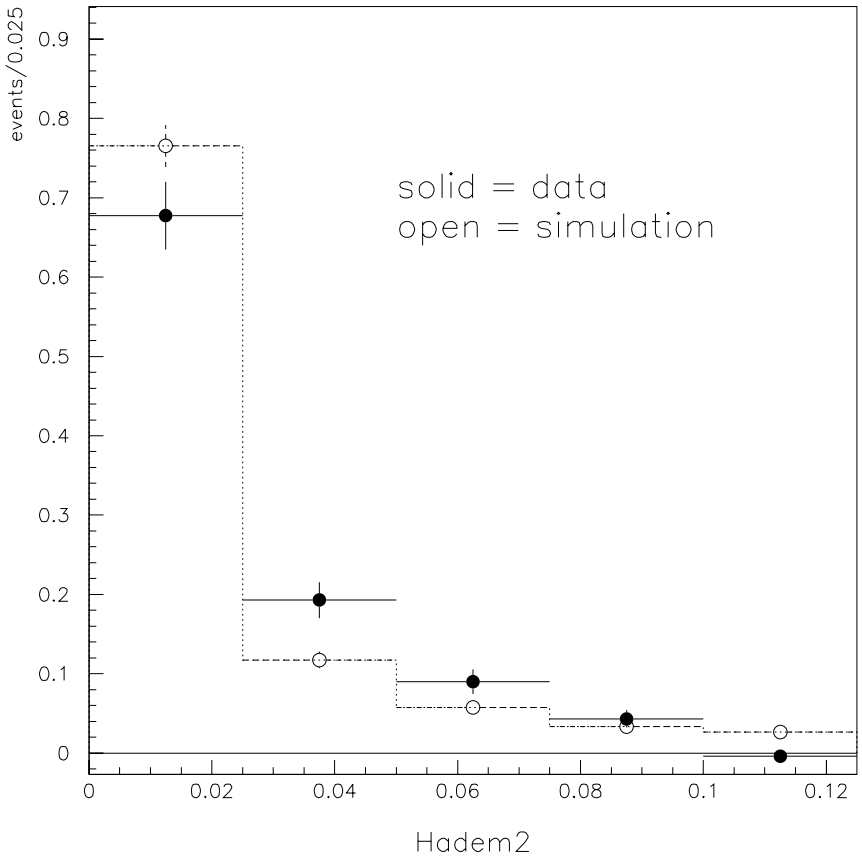

Figure 7.1: Two-tower Hadem distribution from simulation and from D^+ decays in electron data.

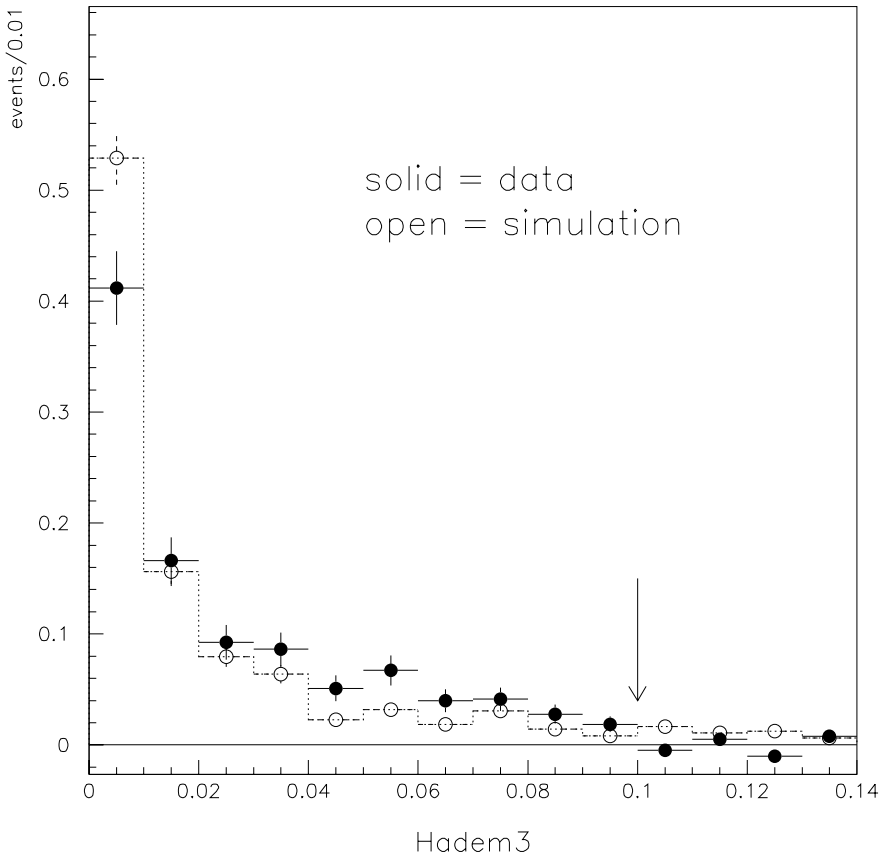

Figure 7.2: Three-tower Hadem distribution from simulation and from D^+ decays in electron data.

that is, the effect of one component must be smaller than the effect of both. Therefore one consistency check is to make sure that the event kill rate due to the additional interactions is less than 6%. This kill rate can be estimated from data. First, the distribution of particles from such additional interactions is uniform in ϕ, whereas most $\overline{b}b$ pairs produce jets back-to-back. Figure 7.3 shows the difference in ϕ between the electron and other tracks in the same event. The distribution clearly peaks at $\Delta\phi = 0$ and $\Delta\phi = \pi$, reflecting the average back-to-back topology. We locate the electron wedge and tower, and find the wedge 90° away in ϕ and in the opposite tower, that is, at $\eta = -\eta_e$, and we count the number of charged tracks pointing to it. We add these tracks to the electron wedge, and flag the event if it now fails the N_{3d} cut. In a portion of the data consisting of 45124 electrons, 2116 events were flagged, resulting in a kill rate of 4.7%. This rate is actually an overestimate of the kill rate due to the additional interactions, since one of the tracks contributing to the kill might have originated from the other underlying event source.

7.6 Bottom Quark Generation

A full calculation, to all orders, of the b quark cross section would be independent of the renormalization scale μ; therefore the residual dependence, resulting from using a next-to-leading order calculation, is a measure of the higher order effects. Nason, Dawson, and Ellis choose a combination of the two available mass scales from the calculation to set the central value of the renormalization scale,

$$\mu = \mu_0 \equiv \sqrt{p_T^2 + m_b^2}. \tag{7.2}$$

We use $\mu = 2\mu_0$ and $\mu = \mu_0/4$ as a reasonable variation to test the residual μ dependence.

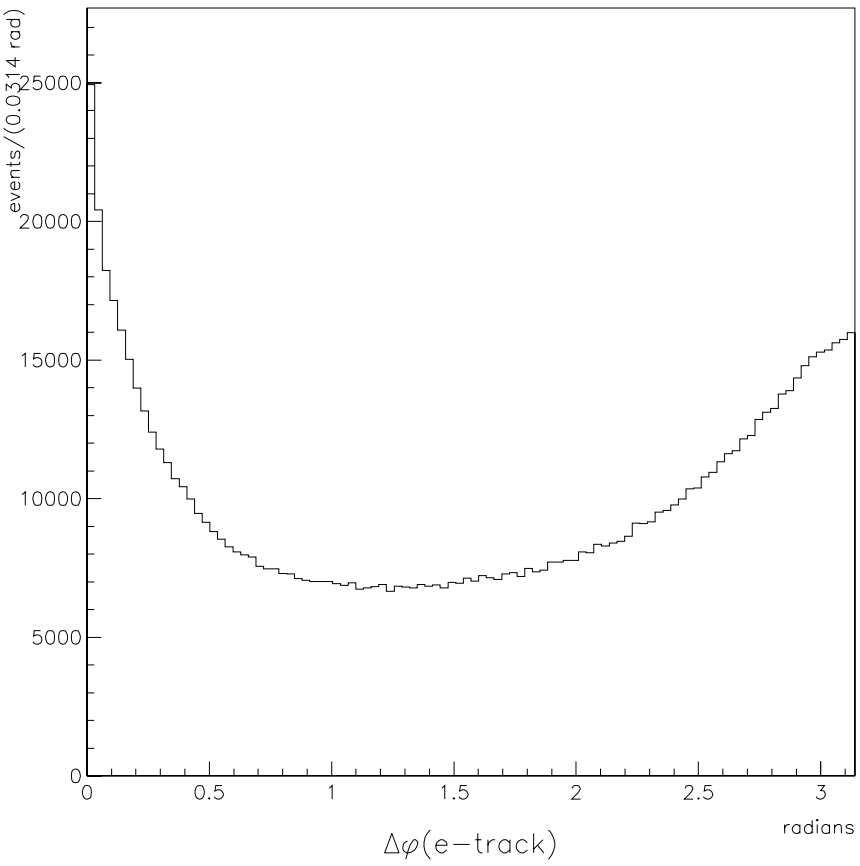

Figure 7.3: Separation in ϕ between electron and other tracks in the same data events for track $p_T > 450$ MeV/c.

There is also an uncertainty in the b quark mass. We have used 4.75 GeV/c^2 as our central value, and vary it ± 0.25 GeV/c^2 along with the renormalization scale. We therefore simulate with two additional b spectra, one with $m_b = 4.50$ GeV/c^2 and $\mu = \mu_0/4$, and another with $m_b = 5.00$ GeV/c^2 and $\mu = 2\mu_0$. The maximum variation in the rate is 20%, which we use as our systematic uncertainty.

The proton structure functions are another uncertainty in the generation of b quarks. Our central value uses the MRSD_0 structure function set of Martin, Roberts, and Stirling. These authors also give an alternate set, MRSD_-, as a $1/sigma$-like variation. Using this alternate set along with the central b quark mass and μ scale changes the rate by less than 1%. The total systematic uncertainty due to the b quark generation is therefore 20%.

7.7 Fragmentation

As noted in Section 1.2.1, we have used the Peterson fragmentation model in our simulation with $\epsilon_b = 0.006 \pm 0.002$, which was measured for B mesons. Since our rate is actually dependent upon fragmentation to a b baryon rather than a meson, we take as a reasonable variation in $\epsilon_b^{\Lambda_b}$ twice the measured error. We calculate the Monte Carlo efficiency again for $\epsilon_b^{\Lambda_b} = 0.002$ and $\epsilon_b^{\Lambda_b} = 0.010$. The z distributions are shown in Figure 7.4. The variation in the efficiency is $\pm 21\%$, with $\epsilon_b^{\Lambda_b} = 0.002$ yielding the higher efficiency, as expected due to its harder z spectrum.

7.8 Polarization

We have assumed in our rate calculation that the Λ_b produced in a $\overline{p}p$ collision is unpolarized. The reality is that the production polarization is unknown.

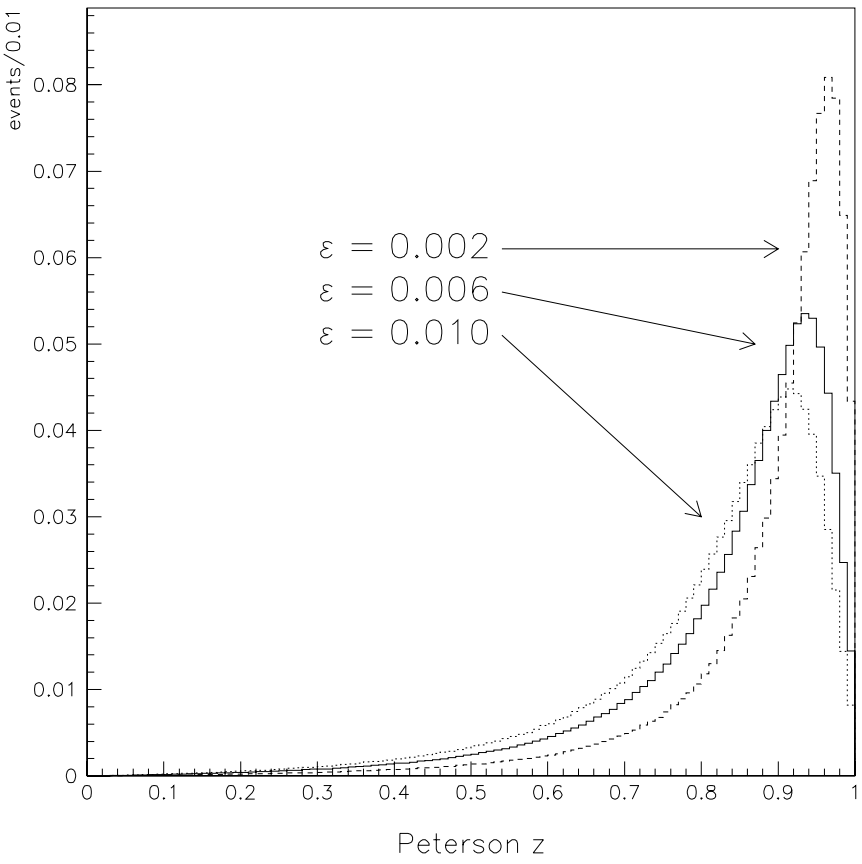

Figure 7.4: z distributions for Peterson fragmentation functions with $\epsilon = 0.006$ (solid), $\epsilon = 0.002$ (dashed), and $\epsilon = 0.010$ (dotted).

The Λ_b polarization changes the distribution of Λ_c decay angles:

$$\frac{d\Gamma}{d\cos\theta_{\Lambda_c}} \sim 1 + P\alpha_{\Lambda_b}\cos\theta_{\Lambda_c} \tag{7.3}$$

where P is the production polarization, and α_{Λ_b} is the decay asymmetry parameter for Λ_b semileptonic decay. The angle θ_{Λ_c} is defined relative to the vector normal to the plane which contains b quark before fragmentation and the hadron afterwards, as shown in Figure 7.5. Both P and α_{Λ_b} take on values from -1 to $+1$, and we therefore vary the product $P\alpha_{\Lambda_b}$ from 0 to ± 1. The reconstruction efficiency changes by $\pm 3\%$, which we adopt as our uncertainty.

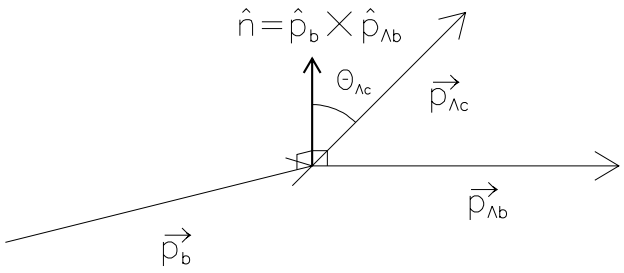

Figure 7.5: Λ_b decay angle definition for production polarization.

7.9 Decay Model

The decay model systematic uncertainty includes two effects. First, there is the question of what exclusive decay modes contribute to this inclusive measurement, for instance the final state $\Lambda_c^{*+} e^- \overline{\nu}_e$ with $\Lambda_c^{*+} \to \Lambda_c^+ \pi^+ \pi^-$, the isospin-suppressed $\Lambda_b \to \Sigma_c^+ e^- \overline{\nu}_e$ with $\Sigma_c^+ \to \Lambda_c^+ \pi^0$ or $\Sigma_c^+ \to \Lambda_c^+ \gamma$, or non-resonant decay modes

with additional hadrons. These decay modes, by increasing the daughter mass, reduce the event reconstruction efficiency relative to that of the exclusive mode. Second, there is the decay distribution, determining how the daughter particles are distributed in phase space.

We have mentioned in Section 1.2.2 an inclusive model based on ACCMM, and an exclusive model based on ISGW, the latter being used for the rate calculation. If instead we use the ACCMM-based model, the efficiency is reduced by 10%.

To estimate the uncertainty due to additional hadron production in $\Lambda_b \to \Lambda_c^+ e^- \overline{\nu}_e X$, we simulate the decay $\Lambda_b \to \Lambda_c^{*+} e^- \overline{\nu}_e$ with $\Lambda_c^{*+} \to \Lambda_c^+ \pi^+ \pi^-$ using a quark-level $V - A$ decay model. We allow this decay mode to contribute up to 50% of the semileptonic decay width. We consider 50% to be a reasonable upper limit because this decay requires the spin of the diquark to change from 0 to 1; the energy to accomplish this change must come from the heavy-heavy $b \to c$ transition, while this heavy quark-light diquark interaction is suppressed in the heavy quark limit. Hence the exclusive decay $\Lambda_b \to \Lambda_c^+ e^- \overline{\nu}_e$ is expected to be the majority of Λ_b semileptonic decays. Since the efficiency can only decrease with this contribution, the rate increases up to 20%. Other decay modes, such as those with a Σ_c or Ξ_c, are isospin or strangeness suppressed.

7.10 Conclusion

The systematic uncertainties have been listed in Table 7.1. The total is $\pm 15\%$ systematic uncertainty due to measured parameters and detector modeling, and $^{+38}_{-31}\%$ theoretical uncertainty.

	% uncertainty
reconstruction efficiency	± 10
luminosity	± 4
Level 2 trigger	± 5
hadron simulation	± 12
underlying event	± 6
Λ_b lifetime	± 3
total systematic uncertainty	± 15
b quark p_T spectrum	± 20
fragmentation	± 21
Λ_b polarization	± 3
Λ_b decay model	± 10
$\frac{\mathrm{Br}(\Lambda_b \to \Lambda_c^{*+} e^- \overline{\nu}_e)}{\mathrm{Br}(\Lambda_b \to \Lambda_c^{+} e^- \overline{\nu}_e) + \mathrm{Br}(\Lambda_b \to \Lambda_c^{*+} e^- \overline{\nu}_e)}$	$+20$
total theoretical uncertainty	$+38$ -31

Table 7.1: Systematic uncertainties.

Chapter 8

Conclusions

The Λ_b production and semileptonic decay rate has been measured at CDF to be

$$\begin{aligned} &\sigma_b(p_T^b > 10.5 \text{ GeV}/c, |y| < 1)\times \\ &f_{\Lambda_b}\text{Br}(\Lambda_b \to \Lambda_c^+ e^- \overline{\nu}_e X)\text{Br}(\Lambda_c^+ \to pK^-\pi^+) \\ &= (2.8 \pm 0.72(stat) \pm 0.41(syst)^{+1.05}_{-0.86}(theory)) \text{ nb}. \end{aligned} \tag{8.1}$$

This is the first measurement of the production and semileptonic decay of the Λ_b at a hadron collider. To compute the product of branching fractions, allowing a comparison between our result and theoretical expectations as well as previous experiments, we can use a CDF b quark cross section measurement, [32]

$$\sigma_b(p_T > 10.5 \text{ GeV}/c, |y| < 1) = 1.99 \pm 0.30 \pm 0.41 \ \mu\text{b}. \tag{8.2}$$

We remove the systematic uncertainties in this measurement due to the choice of structure functions and the luminosity, since these are shared by the present measurement. The product of branching fractions is

$$\begin{aligned} &f_{\Lambda_b}\text{Br}(\Lambda_b \to \Lambda_c^+ e^- \overline{\nu}_e X)\text{Br}(\Lambda_c^+ \to pK^-\pi^+) \\ &= (13.9 \pm 3.6(stat) \pm 4.4(syst)^{+5.3}_{-4.3}(theory)) \times 10^{-4} \end{aligned} \tag{8.3}$$

where the cross section measurement uncertainties have been added to the systematic uncertainty.

All CDF b quark cross section measurements have assumed that the probability that a B_u or B_d meson results from the fragmentation of the b quark is 37.5% each. There are indications that this fraction may be lower. CDF has measured [33]

$$\frac{\sigma_{B_s}}{\sigma_{B_u} + \sigma_{B_d}} = 0.26^{+0.17}_{-0.08} \pm 0.08 \tag{8.4}$$

using the fact that both D^+ and D_s^+ can decay to the common final state $\phi\pi^+$. This measurement assumes equal semileptonic partial widths for the three B mesons and equal D^{**} contributions to these semileptonic widths. A further assumption is made that D_s^{**} decays are dominated by hadronic decays to non-strange D mesons. The usual expectation is that the ratio in Equation 8.4 would be 0.2, whereas this measurement suggests that B_s forms a larger portion of the b fragmentation than expected. Moreover, the LEP experiments have measured the Λ_b product of branching fractions to be those listed in Table 8.1. [34] These measurements are independent of the B meson fragmentation fractions and are consistent with the present measurement within the uncertainties. If we assign the branching fractions as in Section 1.3, f_{Λ_b} is 14% for the PDG $\Lambda_c^+ \to pK^-\pi^+$ branching fraction or 11% for the higher CLEO value. Taking these as measurements of f_{B_s} and f_{Λ_b} reduces our product of branching fractions by up to 9%. We have added this variation to the systematic uncertainty quoted in Equation 8.3.

This measured rate is also consistent with the rate expectation calculated in Section 1.3,

$$f_{\Lambda_b}\mathrm{Br}(\Lambda_b \to \Lambda_c^+ e^- \overline{\nu}_e X)\mathrm{Br}(\Lambda_c^+ \to pK^-\pi^+) = 4.6 \times 10^{-4}. \tag{8.5}$$

However, as noted in Section 1.3, it should be kept in mind that any of the three factors in this prediction may be reasonably expected to be different from the

Experiment	$f_{\Lambda_b}\mathrm{Br}(\Lambda_b \to \Lambda_c^+ e^- \overline{\nu}_e X)\mathrm{Br}(\Lambda_c^+ \to pK^-\pi^+)$
ALEPH	$(6.5 \pm 1.5 \pm 0.8 \pm 0.8) \times 10^{-4}$
DELPHI	$(5.2 \pm 1.1 \pm 0.4^{+1.1}_{-0.5}) \times 10^{-4}$
OPAL	$(6.3 \pm 1.5 \pm 1.1) \times 10^{-4}$

Table 8.1: LEP measurements of the Λ_b product of branching fractions. The first uncertainty is statistical, and where possible, the systematic uncertainty has been split into detector-related and theoretical uncertainties.

values assumed here. Further examination of the Λ_b and Λ_c decays will clarify this picture.

Bibliography

[1] Particle Data Group, "Review of Particle Properties," *Phys. Rev.* **50**, 1173 (1994).

[2] M. Bozzo, *et al.*, *Phys. Lett.* **147B**, 392 (1984).

[3] F. Abe., *et al.*, *Phys. Rev.* **D44**, 29 (1991).

[4] P. Nason, S. Dawson, R.K. Ellis, *Nucl. Phys.* **B327**, 49 (1989).

[5] A.D. Martin, R.G. Roberts, W.J. Stirling, RAL-92-021, DTP-92-16; and A.D. Martin, W.J. Stirling, R.G. Roberts, *Phys. Rev.* **D50**, 6734 (1994).

[6] C. Peterson, D. Schlatter, I. Schmitt, P.M. Zerwas, *Phys. Rev.* **D27**, 105 (1983).

[7] J. Chrin, *Z. Phys.* **C36**, 165 (1987); also S. Bethke, *Z. Phys.* **C29**, 175 (1985) and W. Bartel, *et al.*, *Z. Phys.* **C33**, 339 (1987).

[8] A good review of HQET is available in M. Neubert, *Phys. Rept.* **245**, 259 (1994).

[9] F. Abe, *et al.*, *Phys. Rev. Lett.* **74**, 2626 (1995).

[10] G. Altarelli, N. Cabibbo, G. Corbò, L. Maiani, G. Martinelli, *Nucl. Phys.* **B208**, 365 (1982).

[11] M. Artuso, *et al.*, CLEO-CONF-93-19.

[12] R. Singleton, Jr., *Phys. Rev.* **D43**, 2939 (1991), with a correction to Eq. 2.37 by G. Chiladze (private communication).

[13] N. Isgur, D. Scora, B. Grinstein, M.B. Wise, *Phys. Rev.* **D39**, 799 (1989).

[14] D.J. Scora, Ph.D. dissertation, University of Toronto, 1993.

[15] J. Bartelt, *et al.*, CLEO-CONF-93-19, contributed to the 16th International Symposium on Lepton and Photon Interactions at High Energies, Cornell University, Ithaca, NY, August, 1993.

[16] B. Barish, *et al.*(CLEO Collaboration), *Phys. Rev. Lett.* **76**, 1570 (1996).

[17] I.I. Bigi, UND-HEP-95-BIG02, June, 1995.

[18] Albrecht, *et al.*(ARGUS Collaboration), *Z. Phys.* **C56**, 1 (1994); and Crawford, *et al.*(CLEO Collaboration), *Phys. Rev.* **D45**, 752 (1992).

[19] **CLEO**, *Phys. Lett.* **B323**, 219 (1994).

[20] F. Abe, *et al.*, *Nucl. Instrum. Meth.* , **A271**, 387 (1988).

[21] K. Yasuoka, *et al.*, *Nucl. Instrum. Meth.* , **A267**, 315 (1988).

[22] N. Solomey, A.B. Wicklund, CDF 247 (1984).

[23] CLEO Collaboration, CLEO-CONF-94-8.

[24] Bai, *et al.*(Mark III Collaboration), *Phys. Rev. Lett.* **65**, 686 (1990).

[25] Crawford, *et al.*(CLEO Collaboration), *Phys. Rev.* **D45**, 752 (1992).

[26] T.J. LeCompte and J.D. Lewis, CDF 2938 (January 19, 1995).

[27] N.M. Shaw, CDF 2414, version 1.00 (January 12, 1994).

[28] A.B. Wicklund, K. Byrum, CDF 2624 (March 24, 1994).

[29] F. DeJongh, CDF 1984 (March 3, 1993).

[30] B. Barnett, for the CDF Collaboration, FERMILAB-CONF-96-039-E, contributed to the Conference of the Nuclear and Particle Physics Division of the Russian Academy of Science, Institute of Theoretical and Experimental Physics, Moscow, Russia, October 23-27, 1995.

[31] J. Kroll, "Masses and Lifetimes of B Hadrons," presented at the 17th International Symposium on Lepton-Photon Interactions, Beijing, August 10-15, 1995.

[32] M.W. Bailey, D. Bortoletto, A.F. Garfinkel, A.T. Laasanen, S.M. Tkaczyk, CDF note 2516, March 18, 1994.

[33] T.J. LeCompte, for the CDF Collaboration, FERMILAB-CONF-94-134-E, contributed to the 27th International Conference on High-Energy Physics, Glasgow, Scotland, July 20-27, 1994.

[34] D. Buskilic, *et al.*(ALEPH), *Phys. Lett.* **B294**, 145 (1992); P. Abreu, *et al.*(DELPHI), *Z. Phys.* **C68**, 375 (1995); OPAL note OPN-082.

Vita

Jeffrey Chun-Lee Tseng was born October 9, 1968, in Stanford, California, attending public schools in the same state until matriculation at the California Institute of Technology in Pasadena. While there, he was an undergraduate teaching assistant for an introductory solid state electronics class and pursued research in physical oceanography at the Jet Propulsion Laboratory as well as magnetic monopole physics with the MACRO collaboration. He received his Bachelor of Science degree in June, 1989. The following September, he began graduate study as the George E. Owen Fellow at the Johns Hopkins University in Baltimore, Maryland, studying under Professor Bruce Barnett. He moved to Illinois in June, 1991, to pursue his research with the CDF collaboration at the Fermi National Accelerator Laboratory in Batavia, Illinois. He has also taught mathematics in a high school equivalency (GED) test preparation course at Wayside Cross Rescue Mission, Aurora, since 1992.